ATLAS Electromagnetic Calorimeter performance measurements, search for the Higgs boson in the $H \rightarrow Z\gamma$ channel and detector development for position reconstruction of noble liquid scintillation

Brais López Paredes

Department of Physics and Astronomy

The University of Sheffield

A thesis submitted in fulfilment of the requirements for the degree of

Doctor of Philosophy

March 2015

A mi familia

Abstract

In this thesis, a method for the recovery of QED Final State Radiation photons emitted from muons at small (collinear, $\Delta R < 0.15$) angles is extended to include photons emitted at larger angles ($\Delta R \geq 0.15$) from both electrons and muons. The method is used in the search for Higgs boson decays to 4-leptons, $H \rightarrow ZZ^* \rightarrow 4\ell$, in ATLAS, correcting 3 out of 60 candidate events. It is also applied in the search for Higgs decays to a Z boson and a photon, $H \rightarrow Z\gamma$, introducing a 2% improvement in the upper limit set by the analysis, yielding $11 \times SM$ at $m_H = 125.5$ GeV (95% CL). The method is also used in the measurement of the photon electromagnetic scale to provide a precision better than 0.5%, reducing the measured Higgs mass systematic uncertainty obtained from the $H \rightarrow \gamma\gamma$ analysis. Data-Monte Carlo comparisons are performed to ascertain the validity of the procedure before its application to the different measurements. The collinear photon selection has an efficiency of 70% and a purity of 85%, and a collinear photon is found in 4% of $Z \rightarrow \mu^+\mu^-$ events. The non-collinear selection has an efficiency of 60% and a purity $> 95\%$, and a photon is found in $\sim 1\%$ of events.

The second part of the thesis presents new results from a developed prototype Gaseous Photomultiplier detector based on a cascade of Thick GEM structures intended for gamma-ray position reconstruction in liquid argon. The detector has a MgF_2 window, transparent to VUV light, and a CsI photocathode deposited on the first THGEM. A 10 cm^2 area is instrumented with four readout channels. A gain of $8 \cdot 10^5$ per photoelectron and ~100% photoelectron collection efficiency are measured at stable operation settings. A ~100 μm position resolution at 100 kHz readout rate is demonstrated at room temperature. Structural integrity tests of the detector and seals are successfully performed at cryogenic temperatures by immersing the detector in liquid Nitrogen, laying a good foundation for future operation tests in noble liquids. This new type of device provides a low cost solution for large-area real-time gamma-ray imaging.

Acknowledgements

I would like to thank my supervisor, Stathes Paganis, without whom this thesis would not have been possible, for his support and for his enthusiasm. I would also like to thank all the members of the Sheffield PPPA group, especially Neil Spooner, John MacMillan, Christos Anastopoulos, Davide Costanzo, Dan Tovey, Richard French, Tulay Cuhadar Donszelmann and Matt Robinson for their constant advice despite my persistent need for help. To my fellow PhD students at the University of Sheffield, Gary, Sam, Ed, Josh, Steve, Callum, Martin, Kerry, Jon, Dimitris, Fernando... thanks, *ευχαριστώ*, gracias for all the chats, the coffees, the dinners and the friendship during these nearly four years.

During the time I spent in Portugal I felt like home. For this I would like to thank all of the members of the DRIM group at the Universidade de Aveiro. Professor João Veloso, Carlos, Ana Luísa, Filipe, Anabela, Lara, Luís, Pedro... muito obrigado pela vossa ajuda, pelo vosso tempo, pela vossa amabilidade, pelos vossos conselhos, por ensinar-me a falar *bem* e pela vossa paciência.

Á miña familia, moitas gracias por facerme tan complicado querer volver ó traballo en Sheffield, e por tratarme coma un rei cando estou de volta en Galicia. Quero agradecer especialmente ós meus pais, Jose e Luci, e á miña irmá Sabela que me quixesen, axudasen e aturasen todos estes anos.

Y a María, con quien he compartido casi cada día desde que llegué a Sheffield, gracias por hacer este viaje conmigo. ¡Gracias por apoyarme siempre, por creer en mí y por ser tú!

Contents

CONTENTS

List of Figures

Chapter 1

Introduction

1.1 Particle Physics

The theory currently best describing the composition and interaction of all matter is the Standard Model (SM) [1], accurately verified through experiment. All matter is composed of two different elementary particles: quarks and leptons (fermions with half-integer spin). There are six different flavours of quarks with electric charge, strangeness (S), charm (C), bottom (B) and top (T) quantum numbers, classified in three generations:

	q	Q	S	C	B	T
First generation	d	-1/3	0	0	0	0
	u	2/3	0	0	0	0
Second generation	s	-1/3	-1	0	0	0
	c	2/3	0	1	0	0
Third generation	b	-1/3	0	0	-1	0
	t	2/3	0	0	0	1

Table 1.1: The family of quarks divided into the three different generations and with quantum numbers. The sign convention is to associate negative quantum numbers with negatively charged particles, and vice versa.

Each quark can have three different 'colours', and each has an associated antiquark with inverse quantum numbers and anticolour.

1. INTRODUCTION

There are six leptons, classified according to their electric charge and electron, muon and tau lepton numbers (L_e, μ, τ).

	ℓ	Q	L_e	L_μ	L_τ
First generation	e	-1	1	0	0
	ν_e	0	1	0	0
Second generation	μ	-1	0	1	0
	ν_μ	0	0	1	0
Third generation	τ	-1	0	0	1
	ν_τ	0	0	0	1

Table 1.2: The family of leptons divided into the three different generations associated to their lepton numbers. The sign convention is to assign positive quantum numbers with negatively charged particles, and vice versa.

Each lepton has an associated antilepton with opposite electric charge and lepton numbers.

All leptons and quarks interact via the weak force, while only charged leptons and quarks interact via the electromagnetic force. Quarks interact additionally via the strong force. These three forces are mediated by spin 1 force carriers. The electromagnetic force is mediated by the photon γ, an electrically neutral boson. The weak force is mediated by the neutral Z^0 boson and the electrically charged W^+ and W^- bosons. The strong force is mediated by an octet of coloured bosons, the gluons. The gravitational force mediator particle, the graviton, has not been experimentally found, but a spin 2 particle is required by theoretical arguments. At high interaction energies ($Q >> 100$ GeV), the electromagnetic and the weak force are unified, and it is expected that at energies of $\mathcal{O}(10^{16}$ GeV) all forces unify and can be explained by a Grand Unified Theory (GUT).

Force	Bosons
Electromagnetic	γ
Weak	$Z^0, W^{\pm}$
Strong	g

Table 1.3: Force mediator bosons for the three different forces of the Standard Model. There is only one photon, Z^0 and $W^{\pm}$, but there are eight different gluons carrying different linear combinations of pairs of the three different colours of the strong force.

One additional particle, explaining the origin of the mass of all elementary particles (except neutrinos), is the Higgs boson, the particle associated to the Higgs field and the only scalar (spin 0) elementary particle known to date.

1.1.1 Early developments

Before the discovery of all the different forces affecting elementary particles, the question of how is the atomic nucleus bound together was a puzzling one. From the knowledge of just electromagnetism and gravity, Hideki Yukawa concluded in 1934 that a different force must exist that overcomes electromagnetic repulsion between protons and keeps these and neutrons bound together. It was unoriginally called the strong force, and in the same way as the electromagnetic force, Yukawa proposed that the strong force took place between two distant nucleons via the interchange of a mediating particle. He concluded that if the strong force could not be classically felt it was because it had a very short range (on the order of the nucleus) due to the intermediate particle being massive.

A general expression for the force at a distance between two particles is $\frac{e^{-r/a}}{r^2}$, where r is the distance between the particles and a is the *range* of the force. A rough estimation from the uncertainty principle $\Delta E \Delta t \geq \frac{\hbar}{2\pi}$ can be carried out to obtain a value for the mediator mass. Assuming $\Delta E/c^2 = m_{\text{mediator}}$, $a \simeq 1$ fm and $\Delta t \simeq a/c$, then $m = \frac{\hbar}{2ac} \simeq 100$ MeV/c^2. Yukawa called this particle the *meson*, and when the charged pion $\pi^{\pm}$ was experimentally found ($m \simeq 140$ MeV/c^2), it was assigned the role of strong force mediator.

However, as new particles behaving experimentally like the π were found (*mesons* like the $K^{\pm}$, K^0, ρ, ...) as well as new heavy particles belonging to the *baryon* family

(Λ^0, Δ^+, Ω^-, ...), the quark model was proposed. It proposed that baryons and mesons were composite particles of more elementary particles, the quarks (initially only three flavours were known). Every baryon would be a composite of three quarks, and a meson would be a composite of a quark and an antiquark.

The fact that quarks had never been observed was a fundamental problem. Also, the Δ^{++} baryon could only be explained by the composition of three *u* quarks, which would violate the Pauli exclusion principle. The problem was solved with the inclusion of a new quantum number, the *colour*. If one requires every quark to carry one of three colours (say *red*, *green* or *blue*), then the Pauli exclusion principle would not be violated. Also, if every observed particle in nature is *colourless* (it contains the three different colours together or equal amounts of colour and anticolour), then quarks must be bound inside mesons or baryons, explaining why free quarks were never observed.

Before the proposal and discovery of the neutrinos, the belief about nuclear β decay was that an atomic nucleus decayed into another nucleus with one extra unit of charge via the emission of an electron e^-. For example, ${}^{40}_{19}K \rightarrow {}^{40}_{20}Ca + e^-$ or ${}^{64}_{29}Cu \rightarrow {}^{64}_{30}Zn + e^-$. In general ${}^{A}_{Z}P \rightarrow {}^{A}_{Z+1}Q + e^-$. This kind of three body interaction is kinematically fully determined, and specifically the energy of the electron is fixed and given by the masses of all the participants:

$$E = \frac{m_P^2 - m_Q^2 + m_e^2}{2m_P} \tag{1.1}$$

However, experimentally this was only the *maximum* electron energy observed. This led Pauli to the proposal of a new particle, the neutrino ν, and further research allowed to determine that there existed a different neutrino for each of the charged leptons and the corresponding antineutrinos for the antileptons, together with a different quantum lepton number for each generation.

Thus we now know that nuclear β decay occurs via the decay of a neutron into a proton, an electron and an electron antineutrino:

$$n \rightarrow p^+ + e^- + \overline{\nu}_e \tag{1.2}$$

And similarly for other decays that seemed to be missing momentum and energy, like pion and muon decays.

All particles decaying in this way seemed to have a relatively long lifetime, sug-

gesting a new force that was baptised as *weak* force. All quarks and leptons interact via the weak force via neutral-current interactions and charged-current interactions. The electrically neutral Z boson can be emitted or absorbed by a lepton or a quark. The Z boson mediates processes such as neutrino-electron scattering or $f\bar{f}$ pair production from electron-positron collisions (where photon exchange dominates at low energies). The fundamental vertex of charged-current interactions is that of the conversion of any charged lepton into its corresponding neutrino via the emission of a $W^{\pm}$ boson or the strong-flavour violating conversion of a positively (negatively) charged quark into a negatively(positively) charged quark via the emission of a $W^{\pm}$ boson. For example, this is the process involved in nuclear β decay:

$$\begin{aligned} d &\rightarrow u + W^{-} \\ W^{-} &\rightarrow \bar{\nu}_e + e^{-} \end{aligned} \tag{1.3}$$

Or inverse nuclear β decay, the process used to confirm the existence of the electron antineutrino in the Reines and Cowan experiment [2]:

$$\bar{\nu}_e + p \rightarrow n + e^{+} \tag{1.4}$$

Further experiments led to the determination that the weak force violated parity conservation, acting only on left-handed particles and right-handed antiparticles.

Despite the great difference in strength, weak and electromagnetic interactions were showed to be different manifestations of the same *electroweak* force. The Glashow-Weinberg-Salam theory of electroweak interactions showed that the difference in strength could be attributed to a very high mass of the weak gauge bosons. The masses of the weak bosons are experimentally determined to be [3]:

$$\begin{aligned} m_W &= (80.385 \pm 0.015)\ \mathrm{GeV}/c^2 \\ m_Z &= (91.1876 \pm 0.0021)\ \mathrm{GeV}/c^2 \end{aligned} \tag{1.5}$$

1.1.2 The Standard Model

The Glashow-Weinberg-Salam gauge theory of electroweak interactions is a Yang-Mills theory based on the symmetry group $SU(2)_L \times U(1)_Y$ that describes the elec-

tromagnetic and weak interactions of quarks and leptons. Strong interactions between quarks are described by the theory of Quantum Chromodynamics (QCD), based on the $SU(3)_C$ symmetry group. The Standard Model of particle physics unifies both theories and describes these three forces of nature [4]. This theory comprises two kinds of fields: matter and gauge fields.

The matter fields are the three fermion generations of chiral quarks and leptons defined by the chirality operator $f_{L,R} = \frac{1}{2}(1 \mp \gamma^5) f$ (L = Left-handed. R = Right-handed). Only massless left-handed neutrinos (and right-handed antineutrinos) are considered in the theory. Left-handed fermions belong to weak isodoublets, and right-handed fermions to weak isosinglets:

$$I_f^{3;L,R} = \pm\frac{1}{2}, 0: \quad \begin{array}{llll} L_1 = \begin{pmatrix}\nu_e \\ e^-\end{pmatrix}_L, & e_{R_1} = e_R^-, & Q_1 = \begin{pmatrix}u \\ d\end{pmatrix}_L, & u_{R_1} = u_R, \quad d_{R_1} = d_R \\ L_2 = \begin{pmatrix}\nu_\mu \\ \mu^-\end{pmatrix}_L, & e_{R_2} = \mu_R^-, & Q_2 = \begin{pmatrix}c \\ s\end{pmatrix}_L, & u_{R_2} = c_R, \quad d_{R_2} = s_R \\ L_3 = \begin{pmatrix}\nu_\tau \\ \tau^-\end{pmatrix}_L, & e_{R_3} = \tau_R^-, & Q_3 = \begin{pmatrix}t \\ b\end{pmatrix}_L, & u_{R_3} = t_R, \quad d_{R_3} = b_R \end{array} \tag{1.6}$$

Hypercharge is defined for fermions as a function of the third component of their weak isospin I_f^3 and their electric charge in units of the proton charge $+|e|$:

$$Y_f = 2Q_f - 2I_f^3 \Rightarrow Y_{L_i} = -1, \quad Y_{e_{R_i}} = -2, \quad Y_{Q_i} = \frac{1}{3}, \quad Y_{u_{R_i}} = \frac{4}{3}, \quad Y_{d_{R_i}} = -\frac{2}{3} \tag{1.7}$$

where $i = 1, 2, 3$.

The gauge fields are the particles that mediate the interactions of matter fields. They are bosons of spin one: B_μ, corresponding to the generator Y of $U(1)_Y$ and the fields W_μ^i, $i = 1, 2, 3$, which correspond to the generators T^a, $a = 1, 2, 3$, of $SU(2)_L$, equivalent to $\frac{1}{2}$ the Pauli matrices:

$$T^a = \frac{1}{2}\tau^a; \quad \tau^1 = \begin{pmatrix}0 & 1 \\ 1 & 0\end{pmatrix}, \quad \tau^2 = \begin{pmatrix}0 & -i \\ i & 0\end{pmatrix}, \quad \tau^3 = \begin{pmatrix}1 & 0 \\ 0 & -1\end{pmatrix} \tag{1.8}$$

with commutation relations:

$$\left[T^a, T^b\right] = i\epsilon^{abc} T_c \tag{1.9}$$

where ϵ^{abc} is the Levi-Civita symbol. The strong interaction has eight mediating gluon fields G^a_μ, $a = 1, 2, \ldots, 8$ corresponding to the generators of $SU(3)_C$, given by $\frac{1}{2}$ the 3×3 Gell-Mann anticommuting matrices, which follow the commutation relations:

$$\left[T^a, T^b\right] = if^{abc}T_c \quad \text{with Tr}\left[T^a T^b\right] = \frac{1}{2}\delta_{ab} \tag{1.10}$$

where f^{abc} are the structure constants, completely antisymmetric in the three indices. The field strengths are given by:

$$\begin{aligned} B_{\mu\nu} &= \partial_\mu B_\nu - \partial_\nu B_\mu \\ W^a_{\mu\nu} &= \partial_\mu W^a_\nu - \partial_\nu W^a_\mu + g_2 \epsilon^{abc} W^b_\mu W^c_\nu \\ G^a_{\mu\nu} &= \partial_\mu G^a_\nu - \partial_\nu G^a_\mu + g_s f^{abc} G^b_\mu G^c_\nu \end{aligned} \tag{1.11}$$

where g_2 and g_s are the coupling constants of $SU(2)_L$ and $SU(3)_C$ respectively, and g_1 is the coupling constant of $U(1)_Y$. Self-interactions between gauge fields occur for the the non-abelian $SU(2)_L$ and $SU(3)_C$ groups. Minimal coupling takes place between the matter fields ψ and the gauge fields V_μ through the covariant derivative D_μ, which, for quarks, is defined as:

$$D_\mu \psi = \left(\partial_\mu - ig_s T_a G^a_\mu - ig_2 T_a W^a_\mu - ig_1 \frac{Y_q}{2} B_\mu\right)\psi \tag{1.12}$$

resulting in couplings of the form $g_i \overline{\psi} V_\mu \gamma^\mu \psi$ between fermions and gauge fields.

The Standard Model Lagrangian for massless fermions and bosons is given by

$$\begin{aligned} \mathcal{L}_{SM} = &-\frac{1}{4} G^a_{\mu\nu} G^{\mu\nu}_a - \frac{1}{4} W^a_{\mu\nu} W^{\mu\nu}_a - \frac{1}{4} B_{\mu\nu} B^{\mu\nu} \\ &+ \overline{L}_i i D_\mu \gamma^\mu L_i + \overline{e}_{R_i} i D_\mu \gamma^\mu e_{R_i} + \overline{Q}_i i D_\mu \gamma^\mu Q_i + \overline{u}_{R_i} i D_\mu \gamma^\mu u_{R_i} + \overline{d}_{R_i} i D_\mu \gamma^\mu d_{R_i} \end{aligned} \tag{1.13}$$

which is invariant under local $SU(3)_C \times SU(2)_L \times U(1)_Y$ gauge transformations. For example, the electroweak $SU(2)_L \times U(1)_Y$ sector is invariant under

$$\begin{aligned} &L(x) \to L(x) = e^{i\alpha_a(x)T^a + i\beta(x)Y} L(x), \quad R(x) \to R(x) = e^{i\beta(x)Y} R(x) \\ &\vec{W}_\mu(x) \to \vec{W}_\mu(x) - \frac{1}{g_2}\partial_\mu \vec{\alpha}(x) - \vec{\alpha}(x) \times \vec{W}_\mu(x), \quad B_\mu(x) \to B_\mu(x) - \frac{1}{g_1}\partial_\mu \beta(x). \end{aligned} \tag{1.14}$$

Experimentally, quarks and leptons are massive particles, as well as the three weak force mediators. Mass terms of the form $-m\overline{\psi}\psi$ can be added to account for the matter masses without violating gauge invariance, but a mixture of isospin doublet and singlet occurs within each generation. The addition of a boson mass term $\frac{1}{2}M_W^2 W_\mu W^\mu$ would violate $SU(2) \times U(1)$ gauge invariance. The addition of the experimentally observed mass into the theory avoiding the violation of gauge invariance can be achieved via the Higgs-Brout-Englert-Guralnik-Hagen-Kibble mechanism of spontaneous symmetry breaking [5, 6, 7], usually referred to as the Higgs mechanism, which introduces a scalar field.

1.1.2.1 Electroweak symmetry breaking

In the SM, three gauge bosons need to acquire mass ($W^\pm$, Z), while keeping the photon massless and the symmetry of QED unbroken. The scalar field that will be introduced must therefore provide three degrees of freedom. The simplest choice is an $SU(2)$ doublet Φ of complex scalar fields:

$$\Phi = \begin{pmatrix} \phi^+ \\ \phi^0 \end{pmatrix}, \quad Y_\phi = +1 \tag{1.15}$$

The scalar field Lagrangian

$$\mathcal{L}_S = (D^\mu \Phi)^\dagger (D_\mu \Phi) - V(\Phi), \quad V(\Phi) = \mu^2 \Phi^\dagger \Phi + \lambda (\Phi^\dagger \Phi)^2 \tag{1.16}$$

has to be added to the Lagrangian from equation 1.13. For $\lambda > 0$, the potential is bounded from below, and the minimum is $\langle 0|\Phi|0\rangle = 0$ if $\mu^2 > 0$. However, for $\mu^2 < 0$, Φ develops a vacuum expectation value (vev) $v \neq 0$ with a continuum of minima at $\Phi^\dagger \Phi = -\frac{\mu^2}{2\lambda}$. Choosing a particular minimum in the neutral ϕ^0 direction preserves $U(1)_{QED}$ invariance:

$$\langle \Phi \rangle_0 \equiv \langle 0|\Phi|0\rangle = \begin{pmatrix} 0 \\ \frac{v}{\sqrt{2}} \end{pmatrix}, \quad v = \sqrt{-\frac{\mu^2}{\lambda}} \tag{1.17}$$

The scalar doublet can then be reparametrised as follows:

$$\Phi = \begin{pmatrix} \theta_2 + i\theta_1 \\ \frac{1}{\sqrt{2}}(v + H) - i\theta_3 \end{pmatrix} = e^{i\theta_a(x)\tau^a/v} \begin{pmatrix} 0 \\ \frac{1}{\sqrt{2}}(v + H(x)) \end{pmatrix}, \quad a = 1, 2, 3 \tag{1.18}$$

to first order around the selected minimum. A gauge transformation can then be performed to get rid of the unphysical degrees of freedom:

$$\Phi(x) \to \Phi'(x) = e^{-i\theta_a(x)\tau^a/v}\Phi(x) = \frac{1}{\sqrt{2}} \begin{pmatrix} 0 \\ v + H(x) \end{pmatrix} \tag{1.19}$$

and then calculate $|D_\mu\Phi|^2$ to obtain $\mathcal{L}_S$:

$$|D_\mu\Phi|^2 = \frac{1}{2}(\partial_\mu H)^2 + \frac{1}{8}g_2^2(v + H)^2|W_\mu^1 + iW_\mu^2|^2 + \frac{1}{8}(v + H)^2|g_2W_\mu^3 - g_1B_\mu|^2. \tag{1.20}$$

Four fields $W_\mu^\pm$, Z_μ and A_μ can be naturally defined as linear combinations of the original W_μ^i and B_μ:

$$W^\pm = \frac{1}{\sqrt{2}}(W_\mu^1 \mp iW_\mu^2), \quad Z_\mu = \frac{g_2W_\mu^3 - g_1B_\mu}{\sqrt{g_2^2 + g_1^2}}, \quad A_\mu = \frac{g_2W_\mu^3 + g_1B_\mu}{\sqrt{g_2^2 + g_1^2}} \tag{1.21}$$

where A_μ is the field orthogonal to Z_μ. Substituting the new fields and extracting the terms quadratic in $W^\pm$, Z_μ and A_μ, the masses associated to the new particles can be obtained:

$$M_W^2W_\mu^+W^{-\mu} + \frac{1}{2}M_Z^2Z_\mu Z^\mu + \frac{1}{2}M_A^2A_\mu A^\mu \tag{1.22}$$

Three gauge bosons acquired mass: $W^\pm$ and Z, while the photon remains massless:

$$M_W = \frac{1}{2}vg_2, \quad M_Z = \frac{1}{2}v\sqrt{g_2^2 + g_1^2}, \quad M_A = 0 \tag{1.23}$$

So by spontaneously breaking the $SU(2)_L \times U(1)_Y$ into $U(1)_Q$, three goldstone bosons appeared. By performing a gauge transformation these three unphysical degrees of freedom were incorporated as the longitudinal degree of freedom of the weak gauge bosons, thus allowing for the acquisition of mass. The photon remains massless, since the electromagnetic $U(1)_Q$ symmetry remains unbroken.

Fermion masses can be generated using the same scalar field Φ ($Y = 1$) and with $\tilde{\Phi} = i\tau_2\Phi^*$ ($Y = -1$). The following $SU(2)_L \times U(1)_Y$ invariant Yukawa Lagrangian must be added:

$$\mathcal{L}_F = -\lambda_e \overline{L}\Phi e_R - \lambda_d \overline{Q}\Phi d_R - \lambda_u \overline{Q}\tilde{\Phi} u_R + ... \tag{1.24}$$

For instance, the electron term results in:

$$-\frac{1}{\sqrt{2}}\lambda_e(\overline{\nu}_e, \overline{e}_L)\begin{pmatrix} 0 \\ v + H \end{pmatrix} e_R = -\frac{1}{\sqrt{2}}\lambda_e(v + H)\overline{e}_L e_R \tag{1.25}$$

and the constant term gives a mass of $m_e = \frac{1}{\sqrt{2}}\lambda_e v$. And analogously for the other fermion masses $m_u = \frac{1}{\sqrt{2}}\lambda_u v$, $m_d = \frac{1}{\sqrt{2}}\lambda_d v$, etc., except the neutrinos, for which no right-handed counterpart has been observed.

1.1.2.2 The Higgs boson

The kinetic part of the Higgs field H in the Lagrangian, $\frac{1}{2}(\partial_\mu H)^2$ comes from the covariant derivative $|D_\mu\Phi|^2$, and the mass and the self-interaction terms come from the scalar potential $V(\Phi) = \mu^2\Phi^\dagger\Phi + \lambda(\Phi^\dagger\Phi)^2$. Using $v^2 = -\mu^2/\lambda$ and inserting $\Phi = \frac{1}{\sqrt{2}}\begin{pmatrix} 0 \\ v + H \end{pmatrix}$, the Higgs field Lagrangian becomes:

$$\mathcal{L}_H = \frac{1}{2}(\partial_\mu H)^2 - \lambda v^2 H^2 - \lambda v H^3 - \frac{\lambda}{4}H^4 \tag{1.26}$$

The Higgs mass is given by $M_H^2 = 2\lambda v^2 = -2\mu^2$, where λ is an arbitrary parameter of the Standard Model. The strength of the Higgs self-interactions is therefore proportional to the square of its mass:

$$g_{H^3} \propto \lambda v = \frac{M_H^2}{2v}, \quad g_{H^4} \propto \frac{\lambda}{4} = \frac{M_H^2}{8v^2} \tag{1.27}$$

The coupling of the Higgs to fermions and bosons can be obtained substituting their masses back into the Lagrangian:

$$\mathcal{L}_{M_V} \sim M_V^2(1 + \frac{H}{v})^2, \quad \mathcal{L}_{m_f} \sim -m_f(1 + \frac{H}{v}) \tag{1.28}$$

giving the following coupling strengths:

$$g_{Hff} \propto \frac{m_f}{v}, \quad g_{HVV} \propto \frac{M_V^2}{v}, \quad g_{HHVV} \propto \frac{M_V^2}{v^2} \tag{1.29}$$

The vacuum expectation value v is calculated from the $W^{\pm}$ mass and the Fermi constant G_F, obtained from experiment:

$$M_W = \frac{1}{2} g_2 v = \left(\frac{\sqrt{2} g_2^2}{8 G_F} \right)^{1/2} \Rightarrow v = \frac{1}{(\sqrt{2} G_F)^{1/2}} \simeq 246 \text{ GeV} \tag{1.30}$$

1. INTRODUCTION

Chapter 2

The ATLAS experiment

2.1 The LHC

The Large Hadron Collider (LHC) [8] is currently the newest and highest energy particle physics hadron accelerator and collider in the world. Located at CERN, near Geneva, with a circumference of 26.7 km in the tunnel excavated for the LEP machine, it was designed to achieve a centre-of-mass energy of $\sqrt{s}$ = 14 TeV in proton-proton collisions with a luminosity of 10^{34} cm^{-2} s^{-1} and an energy of 2.8 TeV per nucleon in Lead-Lead collisions at a maximum luminosity of 10^{27} cm^{-2} s^{-1}. The search for the Higgs boson and physics beyond the Standard Model as well as a deeper understanding of CP-violation and quark-gluon plasma motivated the construction of the LHC as a discovery machine, with the highest collision energy and luminosity technologically available to access the very low cross section interactions predicted by the physics models.

Before being injected into the main ring, the particles are first pre-accelerated. Ionised hydrogen gas is fed into the LINAC2 (see figure 2.1), where each proton is accelerated to an energy of 50 MeV. The next step occurs in the Proton Synchrotron Booster (PSB), where the protons are further accelerated to 1.4 GeV, and then to 25 GeV in the Proton Synchrotron (PS) and to 450 GeV in the Super Proton Synchrotron (SPS) before the injection into the LHC via the TI2 and TI8 transfer lines. The protons are accelerated to working energy for $\sim$ 20 min and then circulated for 5 to 24 h while collisions occur. Superconducting dipole and quadrupole magnets are

2. THE ATLAS EXPERIMENT

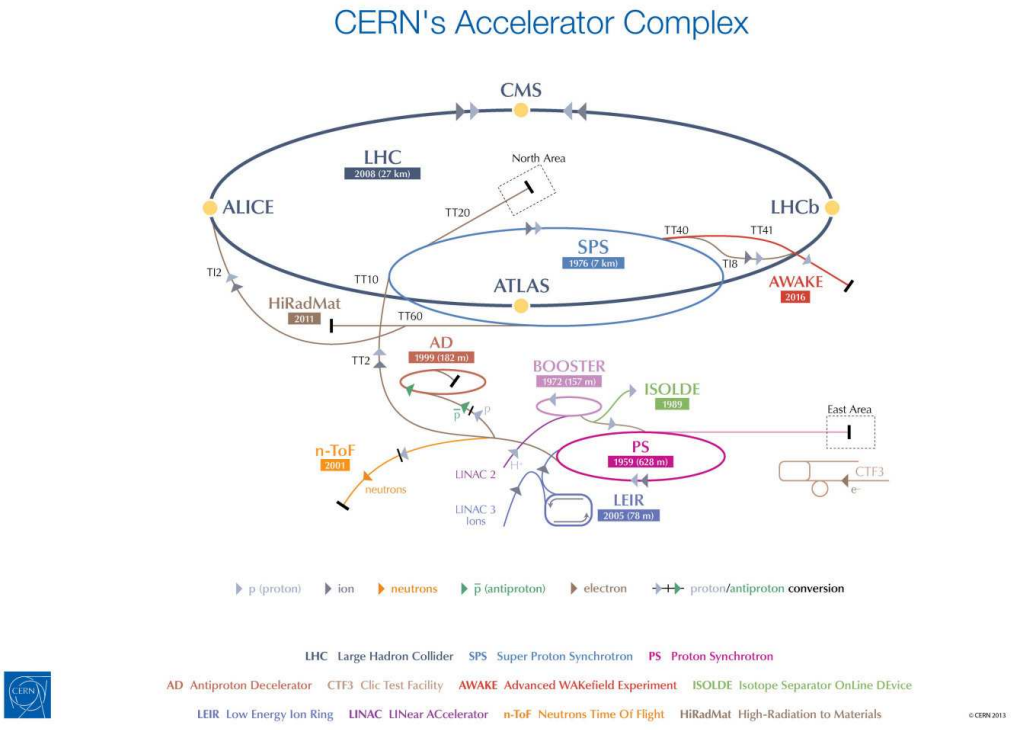

Figure 2.1: The CERN accelerator complex [9].

used in the LHC for focusing and bending of the beam, together with additional beam-correcting magnets. The two beams rotate in opposite directions at a frequency of $\sim$ 40 MHz at design energy, crossing at four interaction points where four experiments are set up: LHCb (Large Hadron Collider Beauty experiment), designed to study the physics of B decays and CP-violation, ALICE (A Large Ion Collider Experiment), which studies heavy ion physics and ATLAS (A Toroidal LHC Apparatus) and CMS (Compact Muon Solenoid), designed to observe all kinds of phenomena and aimed at the discovery of new physics.

The LHC was progressing towards operation at $\sqrt{s}$ = 14 TeV in 2008, but after an interconnection between two dipole magnets failed, releasing tonnes of Helium and damaging the accelerator, the first collisions did not happen until 2010. Nevertheless, the decision was made to reduce the energy of collisions to half the design energy, $\sqrt{s}$ = 7 TeV. The centre-of-mass energy was successfully increased to 8 TeV for the 2012 run. In 2013 the LHC was shut down to proceed with the necessary upgrades to start operating at $\sqrt{s}$ = 13 TeV in early 2015 [10].

In 2012, a new particle was discovered in the search for the Standard Model Higgs boson by the ATLAS and CMS experiments [11, 12]. The properties of the newly discovered particle were later confirmed to agree with those expected from the SM Higgs boson [13, 14, 15, 16]. Two years later, in 2014, the LHCb experiment observed a particle consistent with a tetraquark state from the study of $\overline{B}^0 \rightarrow J/\psi\pi^+\pi^-$ decays [17]. LHC Run II, commencing in early 2015, will bring increased collision energy and luminosity and with this new opportunities for probing unknown physics.

2.2 The ATLAS detector

The ATLAS (A Toroidal LHC Apparatus) detector [18] is one of the main general-purpose detectors at the LHC. It is designed to detect the broadest range of processes possible in proton-proton and heavy ion collisions. It is composed of a series of concentric cylinders playing the roles of: tracker, calorimeter, muon detector and magnet system. A general view of the ATLAS detector is shown in Figure 2.2. Neutrinos are the only known stable particle that cannot be detected by this system, and their presence is detected by missing transverse energy in the detector. Therefore an excellent angular coverage must be achieved. Forward detectors are used for particle detection

up to angles very close to the beam.

The coordinate system of the ATLAS detector is a right-handed euclidean reference frame whose z axis is defined by the beam direction, the x axis points from the interaction point towards the centre of the LHC ring, along its radius, and the y axis points vertically upwards. The azimuthal angle ϕ represents clockwise rotations around the z axis, with the origin at the x axis, and θ is the angle with respect to the z axis. Pseudorapidity is defined as $\eta = -\ln\tan(\theta/2)$. In the relativistic limit ($m/E \to 0$), η is equivalent to rapidity $y = \frac{1}{2}\ln([E + p_z c]/[E - p_z c])$.

A particle's transverse momentum $\vec{p}_T$ is the $x-y$ component of it's momentum $\vec{p}$. Good solid angle coverage ensures that missing transverse momentum (a deviation from $\vec{0}$) is due to undetectable particles, like neutrinos, so it is defined per event as

$$\vec{p}_T^{\,\text{miss}} = -\sum_{i=1}^{n} \vec{p}_T^{\,i} \tag{2.1}$$

where n is the number of particles in the event.

Transverse energy E_T is also used, and it is defined as $E_T = E\cos\theta$. Analogously to missing transverse momentum, missing transverse energy $E_T^{\text{miss}} = |\vec{p}_T^{\,\text{miss}}|$ is defined.

Angular separation between two particles is usually measured in the (η, ϕ) plane. The quantity $\Delta R = \sqrt{\Delta\eta^2 + \Delta\phi^2}$ is used, where $\Delta\eta$ and $\Delta\phi$ are the difference in pseudorapidity and azimuthal angle between the two particles. This is particularly useful due to ΔR being Lorentz invariant under boosts along the beam axis.

2.2.1 Physics requirements

The ATLAS detector was designed to detect new physics processes whose cross-section is expected to be very low compared to Standard Model backgrounds. This implies that every new physics candidate event will be surrounded by dozens of secondary interactions. Excellent particle identification, E_T^{miss} reconstruction and identification of other typical new physics signatures, as well as a high integrated luminosity, are of vital importance to reject the dominant QCD jet background

These goals impose certain requirements for LHC detectors and in particular for ATLAS.

- Very fast and radiation-hard detector components and electronic devices are re-

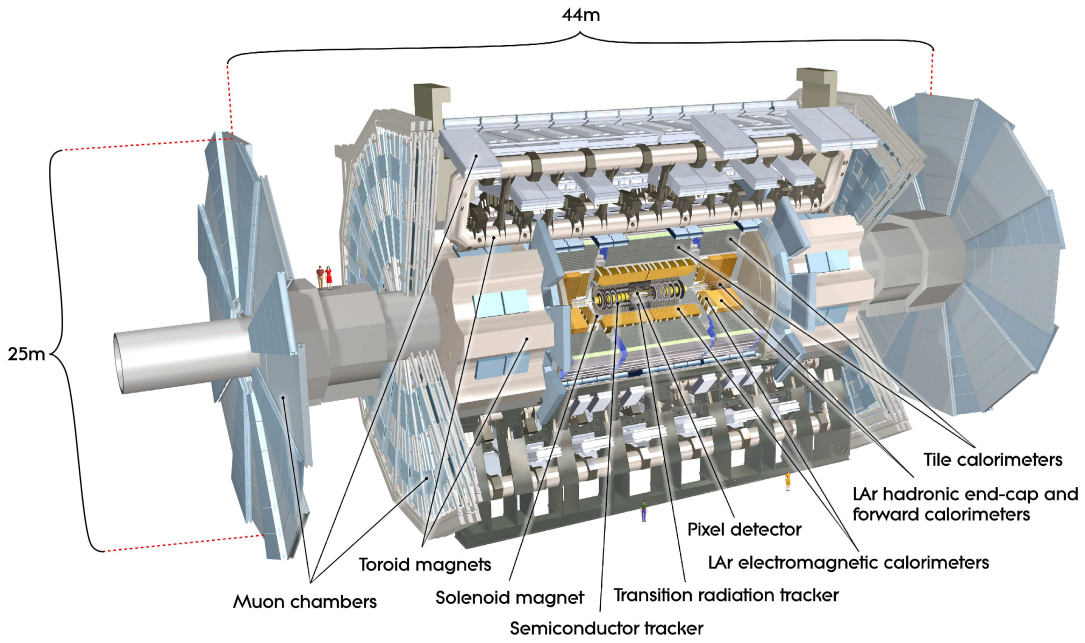

Figure 2.2: An overall view of the ATLAS detector showing its different components. The chosen central solenoidal magnet and the outer toroidal superconductors were the primary geometrical restrictions for the design of the other detector parts [18].

quired to perform under the high particle fluences at the LHC. At the same time, dealing with the presence of secondary interactions (pile-up) demands a high granularity detector.

- Near-full solid angle coverage (η, ϕ) is required for full event reconstruction and E_T^{miss} calculation.

- Good charged particle tracking for well resolved momentum reconstruction close to the interaction region is essential for the identification of secondary vertices and the control of pile-up.

- Very accurate reconstruction and identification of electrons and photons (Electromagnetic calorimeter) and of jets (Hadronic calorimeter) with full angular coverage for E_T^{miss} measurements, vital for many new physics searches.

- Excellent muon identification, momentum measurement and unambiguous charge determination up to very high muon transverse momentum.

- High background rejection combined with efficient triggering on low p_T signal for the study of rare new physics processes.

A summary of the performance goals of ATLAS is shown in Table 2.1. The performance of the muon spectrometer is independent of the inner detector for high p_T muons.

Detector component	Required resolution	η coverage	
		Measurement	Trigger
Tracker	$\sigma_{p_T}/p_T = 0.05\% p_T \oplus 1\%$	± 2.5	n/a
EM Calorimeter	$\sigma_E/E = 10\%/\sqrt{E} \oplus 0.7\%$	± 3.2	± 2.5
Hadronic calorimeter			
barrel and endcap	$\sigma_E/E = 50\%/\sqrt{E} \oplus 3\%$	± 3.2	± 3.2
forward	$\sigma_E/E = 100\%/\sqrt{E} \oplus 10\%$	$3.1 < \lvert\eta\rvert < 4.9$	$3.1 < \lvert\eta\rvert < 4.9$
Muon spectrometer	$\sigma_{p_T}/p_T = 10\%$ at $p_T = 1$ TeV	± 2.7	± 2.4

Table 2.1: ATLAS performance goals [18]. The performance of the muon spectrometer at high muon p_T is independent of the inner detector. Energy and transverse momentum units given in GeV.

2.2.2 Tracking

The ATLAS Inner Detector (ID) was designed for EM particle momenta measurement and vertexing. For high-precision measurements under the luminosity provided by the LHC a very fine detector granularity is required. The Inner Detector is composed of the Pixel and silicon microstrip SemiConductor Tracker (SCT) and the straw-tube Transition Radiation Tracker (TRT). It is submerged into a 2 T magnetic field generated by the central solenoidal magnet.

The Pixel and SCT detectors provide precision tracking within $|\eta| < 2.5$, located at a very small radius from the interaction region. They are divided into two different parts: a central barrel comprised of cylinders concentric to the beam axis, and the end-caps, disks positioned perpendicular to the beam axis. The central barrel provides longitudinal (z) as well as radial and angular ($R - \phi$) information, while the end-cap detectors provide only $R - \phi$ information of the track.

The TRT detector complements the Pixel and SCT detectors by providing $R - \phi$ tracking information at a larger radius, in the $|\eta| < 2.0$ region. In its barrel part, the straw tubes are placed parallel to the beam axis, divided in half at the centre $\eta = 0$. The end-caps present a radial arrangement of the straw-tubes in a series of wheels.

The Inner Detector is in charge of particle tracking and can provide electron identification as well as impact parameter measurements and vertex reconstruction for heavy-jet and τ tagging.

2.2.3 Calorimetry

The calorimeters installed in the ATLAS detector cover the region $|\eta| < 4.9$. They are meant to contain all radiation produced in each event for accurate E_T^{miss} reconstruction. Two distinct calorimeters are present: the Electromagnetic Calorimeter and the Hadronic Calorimeter, with a respective thickness $> 22X_0$ (radiation length) and $> 9.7\lambda$ (interaction length) respectively, adequate for full containment and to reduce the punch-through into the muon systems.

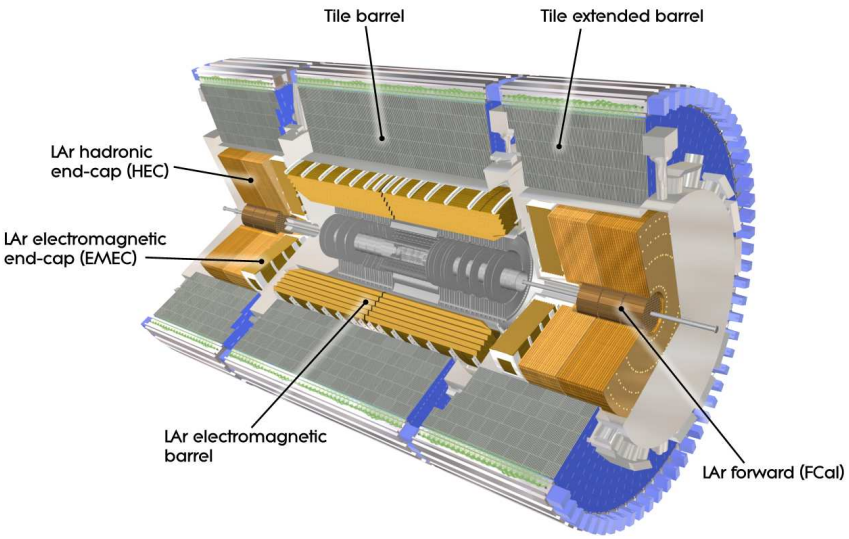

Figure 2.3: Cut-away view of the ATLAS calorimeter systems [18].

2.2.3.1 Electromagnetic Calorimeter

The Electromagnetic Calorimeter is a Lead-LAr calorimeter with kapton electrodes and lead absorber plates, providing full azimuthal coverage without cracks thanks to their accordion shape (see Figure 2.4). It is divided into two parts: the central barrel and the end-caps. The barrel ($|\eta| < 1.475$) has the fine granularity necessary for precision electron and photon energy measurements, while the end-caps ($1.375 < |\eta| < 3.2$) are coarser but sufficient to conform with the physics goals. The barrel calorimeter is divided into two twin half-barrels, separated by 4 mm at $z = 0$, while each of the two end-caps is divided into two coaxial wheels covering respectively $1.375 < |\eta| < 2.5$ (outer wheel) and $2.5 < |\eta| < 3.2$ (inner wheel). A presampler detector present within $|\eta| < 1.8$ provides information about the energy loss of electrons and photons in the passive material upstream of the calorimeter. It is an active liquid Argon layer of 1.1 cm in the barrel and 0.5 cm in the end-cap. The calorimeter region within $|\eta| < 2.5$, dedicated to precision measurements, is segmented longitudinally into three layers. The first layer has the best granularity, intended for position resolution in the clustering of cells. The second sampling absorbs most of the energy carried by electrons and photons thanks to its greater thickness, and the rest is absorbed by the third layer. The

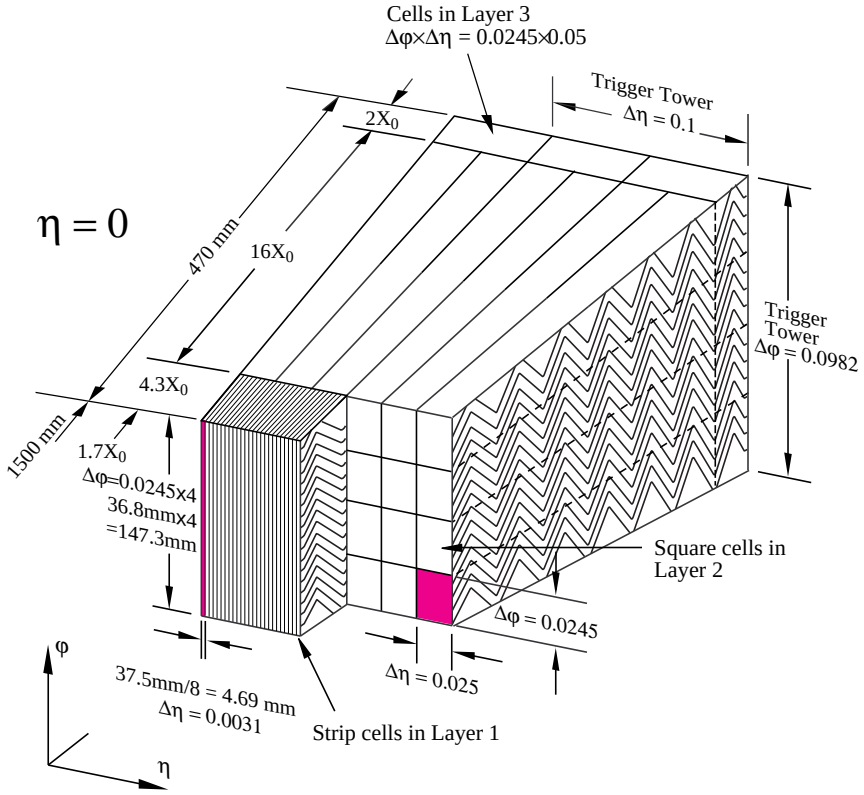

Figure 2.4: ATLAS EM Calorimeter Barrel module [18].

rest of the acceptance is covered by the end-cap inner wheel, with two longitudinal segmentations and coarser lateral granularity.

For a detailed summary of the calorimeter properties (granularity, coverage in pseudorapidity), see table 2.2.

EM calorimeter				
	Barrel		End-caps	
Number of layers and η coverage				
Presampler	1	$\lvert\eta\rvert < 1.52$	1	$1.5 < \lvert\eta\rvert < 1.8$
Calorimeter	3	$\lvert\eta\rvert < 1.35$	2	$1.375 < \lvert\eta\rvert < 1.5$
	2	$1.35 < \lvert\eta\rvert < 1.475$	3	$1.5 < \lvert\eta\rvert < 2.5$
			2	$2.5 < \lvert\eta\rvert < 3.2$
Granularity $\Delta\eta \times \Delta\phi$ vs $\lvert\eta\rvert$				
Presampler	0.025×0.1	$\lvert\eta\rvert < 1.52$	0.025×0.1	$1.5 < \lvert\eta\rvert < 1.8$
Calorimeter 1st layer	$0.025/8 \times 0.1$	$\lvert\eta\rvert < 1.40$	0.050×0.1	$1.375 < \lvert\eta\rvert < 1.425$
	0.025×0.025	$1.40 < \lvert\eta\rvert < 1.475$	0.025×0.1	$1.425 < \lvert\eta\rvert < 1.5$
			$0.025/8 \times 0.1$	$1.5 < \lvert\eta\rvert < 1.8$
			$0.025/6 \times 0.1$	$1.8 < \lvert\eta\rvert < 2.0$
			$0.025/4 \times 0.1$	$2.0 < \lvert\eta\rvert < 2.4$
			0.025×0.1	$2.4 < \lvert\eta\rvert < 2.5$
			0.1×0.1	$2.5 < \lvert\eta\rvert < 3.2$
Calorimeter 2nd layer	0.025×0.025	$\lvert\eta\rvert < 1.40$	0.050×0.025	$1.375 < \lvert\eta\rvert < 1.425$
	0.075×0.025	$1.40 < \lvert\eta\rvert < 1.475$	0.025×0.025	$1.425 < \lvert\eta\rvert < 2.5$
			0.1×0.1	$2.5 < \lvert\eta\rvert < 3.2$
Calorimeter 3rd layer	0.050×0.025	$\lvert\eta\rvert < 1.35$	0.050×0.025	$1.5 < \lvert\eta\rvert < 2.5$
Number of readout channels				
Presampler	7808		1536 (both sides)	
Calorimeter	101760		62208 (both sides)	

Table 2.2: Main electromagnetic calorimeter system parameters [18].

2.2.3.2 Hadronic Calorimeter

The Hadronic Calorimeter is designed to measure the energy and direction of QCD jets produced as a result of the pp collisions. Due to the higher penetration of hadronic showers in comparison to EM showers, the Hadronic calorimeter must present a denser barrier to contain all the energy of a jet and prevent the Muon detectors from being damaged or suffer from extra background events. The Hadronic calorimeter surrounds the EM calorimeter and it is divided into three parts: the Tile calorimeter, the Liquid

argon hadronic end-cap calorimeter and the Forward calorimeter.

Tile calorimeter

Directly around the EM calorimeter is the Tile calorimeter, divided in three overlapping parts covering the region $|\eta| < 1.7$. The central barrel $|\eta| < 1.0$ and the extended barrels $0.8 < |\eta| < 1.7$. It is divided into 64 modules in the azimuthal direction and radially into three layers of 1.5, 4.1 and 1.8λ (interaction lengths) in the barrel region and 1.5, 2.6 and 3.3λ in the extended barrel region. The calorimeter has steel absorbers and scintillating tiles as the active material, from which the light is read-out using wavelength-shifting fibres feeding two photomultiplier tubes for each tile.

LAr hadronic end-cap calorimeter

The hadronic end-cap calorimeters (HEC) are two end-cap wheels placed behind each of the EM calorimeter end-caps inside the same LAr cryostats. It extends from $1.5 < |\eta| < 3.2$, overlapping with the Tile ($|\eta| < 1.7$) and Forward ($|\eta| > 3.1$) calorimeters. The wheels are composed of 32 identical modules, and they are divided into two layers, providing a depth of four segments per end-cap. The more central wheels are built from 25 mm copper plates, and the outer wheels from 50 mm copper plates, with a first plate of half the thickness in both cases. Liquid Argon fills the gaps between the copper plates, acting as the active medium of the detector.

LAr forward calorimeter

The Forward calorimeter (FCal) is also placed inside the LAr end-cap cryostats to preserve detector uniformity and reduce background levels in the muon systems. However, in order to minimise neutron background in the inner detector systems, the Forward calorimeter inner end is located 1.2 m away from the EM calorimeter front face, imposing a more compact, denser solution. With a total of $\sim 10\lambda$, the FCal is segmented into three modules per end-cap: the first, optimised for electromagnetic measurements, is made of copper. The second and third are both made of tungsten and are used for the reconstruction of hadronic particles. The longitudinal channels of a metal array are filled with the electrode structures, parallel to the beam line and formed of

concentric rods and tubes. Liquid argon in the gap between the rod and tube structures acts as the active medium.

2.2.4 The Muon Spectrometer

The Muon Spectrometer (MS) was designed to measure the momentum of charged particles leaving the calorimeter system. It is located in the outer part of the ATLAS detector, enclosing the other detector systems, covering a range of $|\eta| < 2.7$. Muons are MIPs[1] able to cross the electromagnetic and hadronic calorimeters losing only a small percentage of their energy to ionisation. The measurement of their momentum relies on bending their trajectory in a magnetic field and measuring the deviation from the track reconstruction. The field in the $|\eta| < 1.4$ region is provided by the large toroidal magnets visible in figure 2.2. In the range $1.6 < |\eta| < 2.7$ smaller magnets situated at the ends of the barrel magnets provide the magnetic field necessary for bending. In the transition region between these two ranges, $1.4 < |\eta| < 1.6$, both magnetic fields combined deflect the charged particle. In all cases the magnetic field is mostly perpendicular to the muon direction and it minimises the resolution deterioration from multiple scattering.

In the barrel region, three cylindrical chambers concentric to the beam axis measure the track bending. In the transition region and the end-caps, the chambers are planar and arranged perpendicularly to the beam axis. Precision tracking is performed by the Monitored Drift Tubes (MDTs) and the Cathode Strip Chambers (CSCs). The MDTs cover the region $|\eta| < 2.7$, except the innermost end-cap layer, which extends only to $|\eta| < 2.0$. They consist of aluminium cylinders with a diameter of 3 cm with an anode wire in the axis and filled with a mixture of Ar/3%CO_2. Muon ionisation electrons drift towards the anode wire and produce a signal that can be timed with trigger information, providing an overall resolution of 35 μm, and 80 μm per tube. The CSCs are used in the higher flux $2.0 < |\eta| < 2.7$ region due to their higher rate capabilities and time resolution. They are multiwire proportional chambers with the cathode strips perpendicularly aligned for 2D position reconstruction with 60 μm resolution in the bending plane and 5 μm in the direction perpendicular to the bending plane. Triggering is performed with the Resistive Plate Chambers (RPCs) in the barrel and Thin Gap

[1] Minimum Ionising Particles.

Chambers (TGCs) in the end-caps. RPCs provide fast triggering in the barrel region $|\eta| < 1.05$. They consist of resistive plates separated by 2 mm and filled with a gas mixture that is ionised when traversed by a muon. A high electric field applied between the plates accelerates the ionisation electrons and generates a cascade that induces a signal in the metallic electrodes on the outer surfaces of the resistive plates. The TGCs are used for fast triggering and to provide an additional azimuthal coordinate measurement in the end-cap regions to complement the MDT action. It is a multiwire proportional chamber that covers the region $1.05 < |\eta| < 2.4$ and a time of response of 25 ns with a 99% probability.

2.2.5 Trigger, readout and data acquisition

The trigger system is subdivided into three levels: L1, L2 and the Event Filter. The superior levels apply stricter or additional selection criteria to the events accepted by the previous trigger subsystem. The L1 is triggered when high p_T muons, electrons, jets or τ-leptons decaying to hadrons are found, or when a high missing E_T and total E_T is measured. High p_T muons trigger the RPC and TGC systems previously described, and calorimetric triggering is based on measurements with reduced granularity. A selection is then applied in the central trigger processor, where prescaling is also available to optimise bandwidth use. L1 also defines (η, ϕ) Regions of Interest (RoI's) including information about the event and trigger characteristics. L2 uses the RoI data to access full granularity information about the event in the (η, ϕ) areas flagged by L1, and it is optimised to reduce the event rate to $\sim$ 3.5 kHz spending an average of 40 ms per event. The Event Filter subsequently reduces the event rate to $\sim$ 200 Hz with offline software that employs $\sim$ 4 s per event.

2.3 Particle reconstruction and identification in the Electromagnetic Calorimeter

2.3.1 Energy reconstruction

Electromagnetic particles interact with the dense lead absorber plates and start an electromagnetic shower that subsequently ionises the liquid Argon medium between the

plates. Charge in the form of ionisation electrons then drifts towards the electrodes, inducing a signal proportional to the energy that was deposited in the medium. The signal is amplified, shaped and stored, and later digitised and reconstructed cell by cell if the level-1 trigger fires.

2.3.2 Clustering and particle reconstruction

In the region $|\eta| < 2.47$, electrons and photons are reconstructed from clusters of energy deposited in the calorimeter. The energy deposited in all the longitudinal segments of the calorimeter in the regions of a $\Delta\eta \times \Delta\phi = 0.025 \times 0.025$ grid is summed. These energy towers then seed the standard ATLAS *sliding-window* algorithm that, starting from regions of $E_T > 2.5$ GeV, looks for contiguous energy deposits with windows that cover regions of 3×5 towers. If a cluster is matched to an ID track whose origin corresponds to a vertex in the interaction region, it is considered to be an electron. Tracks originating from photon conversions can also be identified, and in such case the cluster is considered a single or a double-track converted photon, depending on the number of reconstructed tracks found to match the cluster. If no tracks match it, the cluster is classified as an unconverted photon.

Electron clusters are then recalculated using a window spanning an area of 3×7 Layer 2 cells in the Barrel calorimeter, and 5×5 Layer 2 cells in the End-cap calorimeter. Photon clusters in the Barrel calorimeter are reconstructed with a 3×7 window in the case of conversions, and with a 3×5 window in the case of unconverted photons, accounting for the reduced lateral size of the shower. In the End-caps, a 5×5 window is also used for both converted and unconverted photons. The lateral size of the window was optimised as a compromise between the coverage of the energy, distributed in the calorimeter differently for each of the three cluster classifications, and the minimisation of pile-up and noise affecting the energy measurement. The cluster energy is calibrated applying correction factors calculated from a full simulation of the detector accounting for energy lost in the passive material upstream of the calorimeter, lost beyond the EM calorimeter and deposited on cells neighbouring the reconstruction window.

2.3.3 Electron and photon identification

Electrons and photons leave distinctive energy depositions in the calorimeter, and their characteristics can be identified studying variables associated to the different layers of the EM calorimeter indicating the longitudinal and transverse characteristics of the shower.

The compatibility of an energy cluster with an electron is decided with a set of three cuts with increasing background rejection: *Loose*, *Medium* and *Tight*. Loose identification criteria include shower shape variables from the second calorimeter layer, as well as the energy deposited in the hadronic calorimeter and track quality and track-matching parameters. The tighter selections are stricter on said variables and impose additional cuts on track and energy-related quantities, including variables from the first calorimeter layer.

Photon identification is subdivided in only two categories: *Loose* and *Tight*. The distributions of the calorimetric variables used [19] are shown in figures 2.5 to 2.13, for both unconverted (a) and converted (b) photon candidates with $E_T > 20$ GeV and $|\eta| < 2.37$ (excluding $1.37 < |\eta| < 1.52$) selected from $Z \to \ell\ell\gamma$ events obtained from the 2012 data sample (dots). The distributions for true photons from simulated $Z \to \ell\ell\gamma$ events (black hollow histogram) and for fake photons from hadronic jets in $Z(\to \ell\ell)$+ jets (red hatched histogram) are also shown, after reweighting their 2D E_T vs η distributions to match that of the data candidates, and correcting the respective calorimetric variable by the average shift between data and simulation distributions determined from the inclusive sample of isolated photon candidates passing the tight selection per bin of (η, E_T) and conversion status. Photon isolation is required on the photon candidate but no criteria on the shower shape are applied. The photon purity of the data sample is $\sim$ 99% [20]. Good agreement between data and Montecarlo and apparent differences between signal-background and converted-unconverted photons are observed for the different variables. The Loose identification criteria applied to photons are equivalent to the electron case, excluding the track-related variables, and the selection is used for triggering purposes. The set of variables used for the Loose criteria are:

- The fraction of energy deposited on a 3×7 to a 7×7 window of second layer

cells

$$R_\eta = \frac{E^{S2}_{3\times7}}{E^{S2}_{7\times7}} \tag{2.2}$$

sensitive to the width of the shower in the η direction (see figure 2.5).

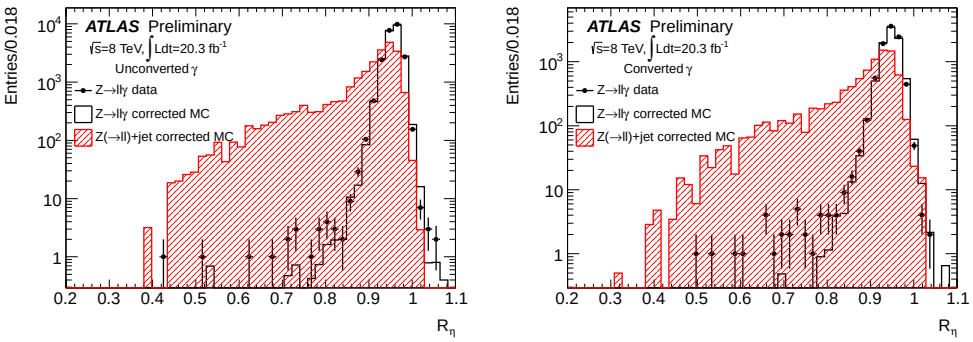

(a) (b)

Figure 2.5: R_η distribution for a selection of unconverted (a) and converted (b) photons from $Z \to \ell\ell\gamma$ events in data (dots) and Monte Carlo simulation (black histogram), compared to a sample of fake photons from $Z(\to \ell\ell)$+jets events (red hatched histogram) with E_T and η reweighted to match the photon distribution, as described in section 2.3.3.

- The width of the shower in the second layer in the η direction, defined as the cell-energy weighted standard deviation of the η position of each cell in a window of 3×5 (see figure 2.6)

$$\omega_{\eta 2} = \sqrt{\frac{\sum (E_c \cdot \eta_c^2)}{\sum E_c} - \left[\frac{\sum (E_c \cdot \eta_c)}{\sum E_c}\right]^2} \tag{2.3}$$

- The fraction of transverse energy deposited in the whole hadronic calorimeter ($0.8 < |\eta| < 1.37$) or only in the first layer ($|\eta| < 0.8$ or $|\eta| > 1.37$) to the energy deposited in the EM calorimeter (see figure 2.7)

$$R_{\text{had}} = \frac{E_T^{\text{had}}}{E_T} \tag{2.4}$$

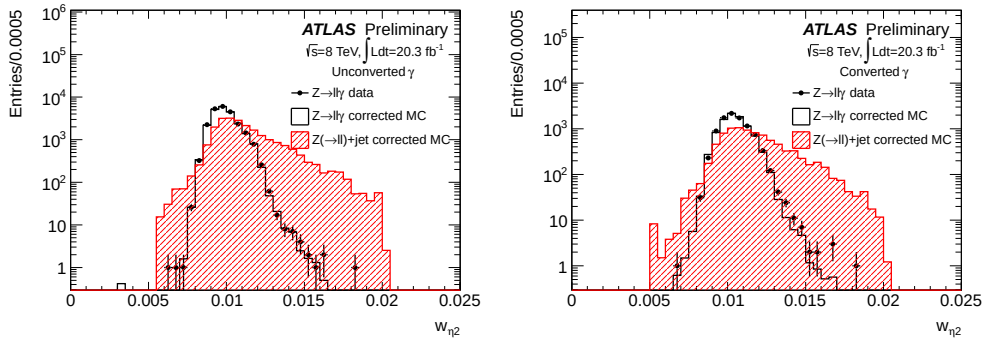

(a) (b)

Figure 2.6: $\omega_{\eta 2}$ distribution for a selection of unconverted (a) and converted (b) photons from $Z \to \ell\ell\gamma$ events in data (dots) and Monte Carlo simulation (black histogram), compared to a sample of fake photons from $Z(\to \ell\ell)$+jets events (red hatched histogram) with E_T and η reweighted to match the photon distribution, as described in section 2.3.3.

The Tight identification criteria impose stricter cuts on the variables used for the Loose selection, and it includes cuts on additional variables optimised to reject the background from $\pi^0 \to \gamma\gamma$ decays, two very close photons that leave a broader shower resembling a single photon deposition. The cuts are optimised for robustness under pile-up conditions. An additional variable from the second layer is used:

- The fraction of energy deposited on a 3×3 to a 3×7 window of second layer cells

$$R_\phi = \frac{E^{S2}_{3\times 3}}{E^{S2}_{3\times 7}} \tag{2.5}$$

  sensitive to the width of the shower in the ϕ direction, a discriminating variable between converted and unconverted photons thanks to the magnetic bending of charged particles in the ϕ direction provided by the magnetic field (see figure 2.8).

And the rest are Layer 1 variables:

- The lateral containment of the shower in the η direction, calculated as the fraction

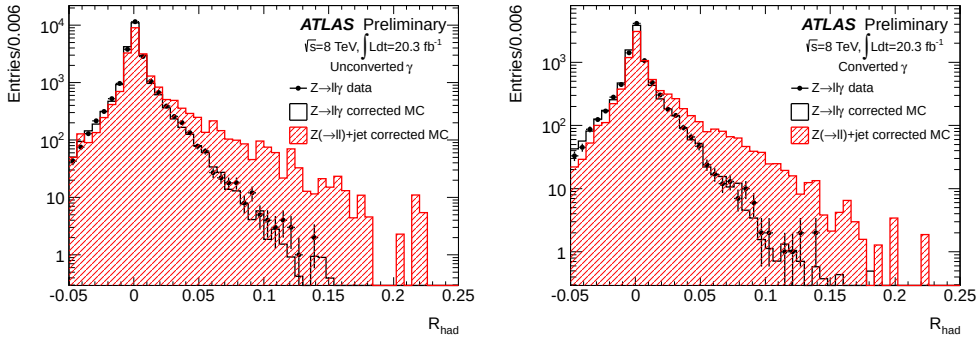

(a) (b)

Figure 2.7: R_{had} distribution for a selection of unconverted (a) and converted (b) photons from $Z \to \ell\ell\gamma$ events in data (dots) and Monte Carlo simulation (black histogram), compared to a sample of fake photons from $Z(\to \ell\ell)$+jets events (red hatched histogram) with E_T and η reweighted to match the photon distribution, as described in section 2.3.3.

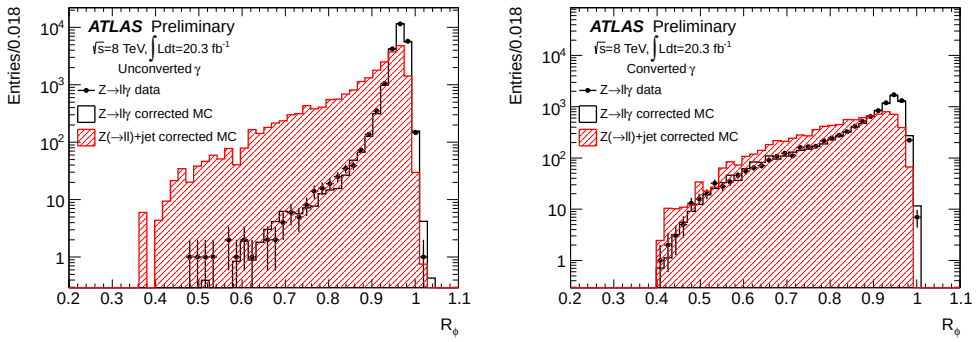

(a) (b)

Figure 2.8: R_ϕ distribution for a selection of unconverted (a) and converted (b) photons from $Z \to \ell\ell\gamma$ events in data (dots) and Monte Carlo simulation (black histogram), compared to a sample of fake photons from $Z(\to \ell\ell)$+jets events (red hatched histogram) with E_T and η reweighted to match the photon distribution, as described in section 2.3.3.

of energy deposited three strips away from the strip with the highest energy

$$F_{\text{side}} = \frac{E(\pm 3) - E(\pm 1)}{E(\pm 1)} \tag{2.6}$$

where $E(\pm n)$ represents the energy of the strip at position $\pm n$ from the highest energy strip at $n = 1$ (see figure 2.9).

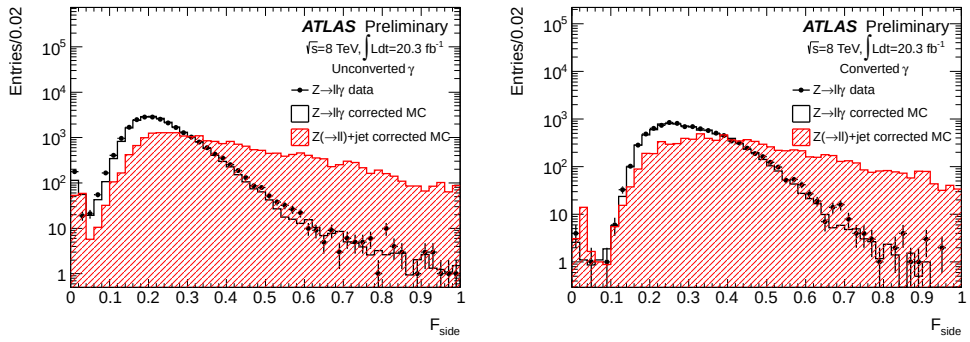

(a) (b)

Figure 2.9: F_{side} distribution for a selection of unconverted (a) and converted (b) photons from $Z \to \ell\ell\gamma$ events in data (dots) and Monte Carlo simulation (black histogram), compared to a sample of fake photons from $Z(\to \ell\ell)$+jets events (red hatched histogram) with E_T and η reweighted to match the photon distribution, as described in section 2.3.3.

- The difference between the second local maximum and the minimum energy found in a strip between the first and second energy maxima

$$\Delta E_s = E^{\text{S1}}_{\text{max2}} - E^{\text{S1}}_{\text{min}} \tag{2.7}$$

with a value of $\Delta E_s = 0$ if no second maximum is found (see figure 2.10).

- and the relative difference of the two local energy maxima

$$E_{\text{ratio}} = \frac{E^{\text{S1}}_{1^{st}\,\text{max}} - E^{\text{S1}}_{2^{nd}\,\text{max}}}{E^{\text{S1}}_{1^{st}\,\text{max}} + E^{\text{S1}}_{2^{nd}\,\text{max}}} \tag{2.8}$$

with a value of $E_{\text{ratio}} = 1$ if there is no second energy maximum (see fig-

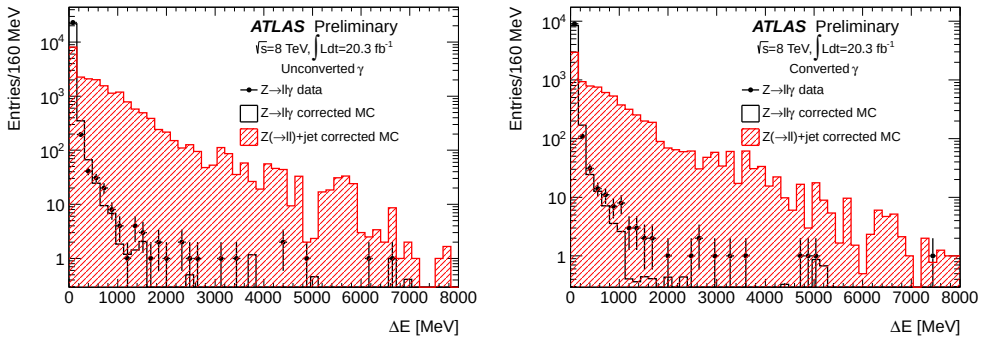

(a) (b)

Figure 2.10: ΔE_s distribution for a selection of unconverted (a) and converted (b) photons from $Z \to \ell\ell\gamma$ events in data (dots) and Monte Carlo simulation (black histogram), compared to a sample of fake photons from $Z(\to \ell\ell)$+jets events (red hatched histogram) with E_T and η reweighted to match the photon distribution, as described in section 2.3.3.

ure 2.11).

The two last variables help to identify a second peak in clusters originated from $\pi^0 \to \gamma\gamma$ decays, usually found in the first layer.

- The width of the shower in the η direction with respect to the highest energy strips calculated in a radius of three strips around it and weighted to their energy

$$\omega_{s3} = \sqrt{\frac{\sum E_i \cdot (i - i_{\max})^2}{\sum E_i}} \tag{2.9}$$

where i is the index of the strip, $i_{\max}$ the index of the highest energy strip and E_i the energy deposited in i (see figure 2.12).

- The shower width in the η direction calculated over the strips covering 2.5 second layer cells, which is a variable number (see table 2.2)

$$\omega_{stot} \tag{2.10}$$

computed as ω_{s3} (see figure 2.13).

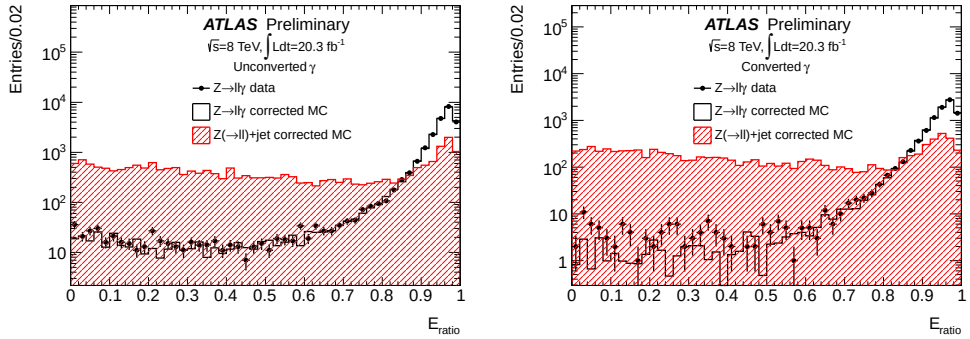

(a) (b)

Figure 2.11: E_{ratio} distribution for a selection of unconverted (a) and converted (b) photons from $Z \to \ell\ell\gamma$ events in data (dots) and Monte Carlo simulation (black histogram), compared to a sample of fake photons from $Z(\to \ell\ell)$+jets events (red hatched histogram) with E_T and η reweighted to match the photon distribution, as described in section 2.3.3.

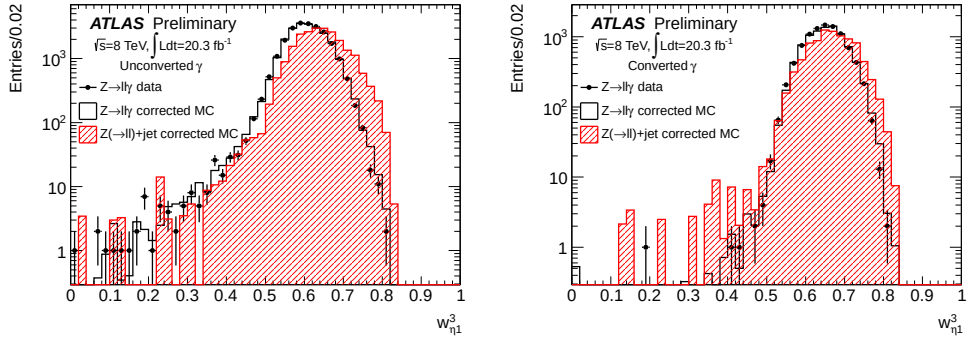

(a) (b)

Figure 2.12: ω_{s3} distribution for a selection of unconverted (a) and converted (b) photons from $Z \to \ell\ell\gamma$ events in data (dots) and Monte Carlo simulation (black histogram), compared to a sample of fake photons from $Z(\to \ell\ell)$+jets events (red hatched histogram) with E_T and η reweighted to match the photon distribution, as described in section 2.3.3.

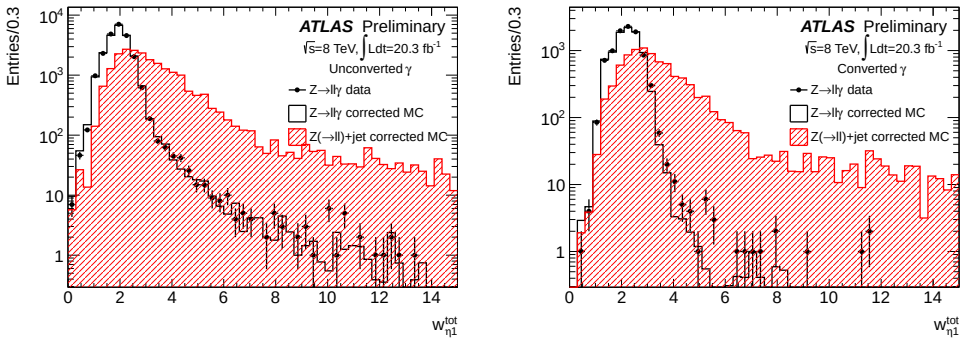

(a) (b)

Figure 2.13: ω_{stot} distribution for a selection of unconverted (a) and converted (b) photons from $Z \rightarrow \ell\ell\gamma$ events in data (dots) and Monte Carlo simulation (black histogram), compared to a sample of fake photons from $Z(\rightarrow \ell\ell)$+jets events (red hatched histogram) with E_T and η reweighted to match the photon distribution, as described in section 2.3.3.

Tight identification criteria are optimised separately for converted and unconverted photons, with an identification efficiency of $\sim$ 85% for $E_T > 40$ GeV and a purity of $\sim$ 99.98% (5000 : 1). The cuts applied on the photon candidates vary with η to account for differences in the material in front of the calorimeter and the geometry, but they do not change with photon E_T [21].

Chapter 3

Reconstruction of QED Final State Radiation in $Z \rightarrow \ell\ell$ events for Higgs boson mass correction

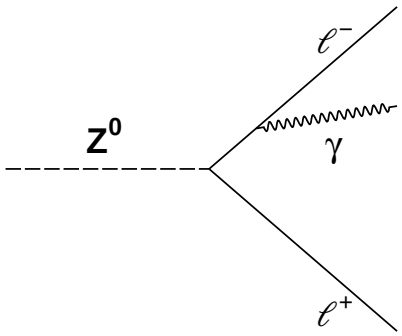

Figure 3.1: $Z \rightarrow \ell\ell\gamma$ diagram

The QED Final State Radiation (FSR) significantly affects the shape of the Z boson mass resonance when the particle decays into a $\mu^+\mu^-$ or an e^+e^- pair and a γ is radiated by one of the leptons. $Z \rightarrow l^+l^-\gamma$ events belonging to the Z mass pole are shifted to lower masses when the energetic photon is neglected. This affects all channels with charged leptons in the final state, like $H \rightarrow Z\gamma(Z \rightarrow \ell^+\ell^-)$ or $H \rightarrow \mu^+\mu^-$ and particularly the $H \rightarrow ZZ \rightarrow 4\ell$, where the omission of FSR photons leads to long mass

tails that affect the mass measurement.

Final state photons are radiated at any angle with respect to the emitting lepton, with the highest probability occurring at very small angles. The amount of energy radiated by the leptons ranges from a small quantity to a significant fraction of the particle's energy. In ATLAS these photons then interact and leave their energy in the EM Liquid Argon Calorimeter in the form of an energy cluster from which the photon energy is reconstructed.

3.1 FSR photon identification

The FSR photons emitted by a lepton at a very small angle with respect to its momentum direction are known as *collinear*. In such cases, the photon energy cluster in the EM Calorimeter is located within a small $\Delta R < 0.15$ cone around the lepton track, providing a strong discrimination against otherwise indistinguishable background photons. Collinear FSR photons emitted by electrons are usually included into the electron calorimeter shower and therefore do not need to be recovered. When emitted by muons, the photon needs to be recovered from the energy cluster, which is sometimes intersected by the muon track. For clusters with $E_T \geq 3.5$ GeV, standard ATLAS photon tools are used to reconstruct the photon energy and position. However, if a muon track has intersected the photon cluster, the photon and the track are wrongly attached to an electron, but the FSR photon can still be recovered searching for electrons that share the muon track and using the energy of the cluster associated to the electron. Muons also deposit energy in the calorimeter, so this contribution must be corrected. For clusters with $E_T < 3.5$ GeV, a dedicated *topologically seeded* clustering algorithm is able to reconstruct photons down to a few hundred MeV, at the expense of decreased purity.

The FSR photons emitted at $\Delta R \geq 0.15$ with respect to the lepton direction are known as *non-collinear* or *far*. Due to the lack of discriminating parameters with respect to background photons only high energy clusters are considered in this case, emitted from both muons and electrons and reconstructed with standard ATLAS photon tools.

A dedicated method to include collinear FSR photons in the reconstruction of Z bosons decaying to pairs of muons was developed and first presented in [22]. The

algorithm was extended to include non-collinear FSR photons emitted from electrons and muons.

3.1.1 Data and Monte Carlo samples

The studies presented here focus on the $Z \to \mu^+\mu^-$ decay channel and use all events found in the 2012 proton-proton collision data collected at $\sqrt{s} = 8$ TeV (20.3 fb^{-1}). The simulated $Z \to \mu^+\mu^-(\gamma)$ events were generated with ALPGEN [23], using CTEQ6L1 PDFs at LO with LO α_s and with up to five additional partons in the hard scattering process, then interfaced to PYTHIA [24] (Perugia2011C tune) for hadronisation and showering. The effects of QED radiative corrections are calculated with PHOTOS [25], a package dedicated to the decay of resonant states. All events are fully simulated with GEANT4 [26], including pile-up. Weighting is applied to match the average number of interactions per bunch crossing to the measured value.

3.1.2 Photon selection

The selection of collinear photons is based on three variables, described below and shown in figure 3.2. Monte Carlo information was used to determine whether an event was true signal or background. The nature of the background was also determined to be either muon ionisation energy reconstructed as an FSR photon or hadrons depositing energy in the calorimeter. Note that both backgrounds are stacked.

The angular separation $\Delta R = \sqrt{\Delta\eta^2 + \Delta\phi^2}$ between the energy clusters and the muon track must be $\Delta R < 0.15$ to reduce the impact of hadronic background, as shown in figure 3.2a (green histogram). Muon ionisation energy (blue histogram) is mostly localised at $\Delta R < 0.08$. However, this is where most of the signal is present (black histogram). To discriminate muon ionisation from true FSR photon signal the longitudinal segmentation of the EM calorimeter is used. The fraction of energy left in the first sampling of the calorimeter divided by the total energy left in the calorimeter (f_1) is shown in figure 3.2b. Most of the signal leaves a significant fraction of its energy in the first calorimeter sampling ($f_1 > 10\%$), as photons interact with the dense medium and an electromagnetic shower starts developing. Muons behave as Minimum Ionising Particles (MIPs) that slowly lose energy in the EM calorimeter following the Bethe-

Bloch formula[1]. Consequently, muons always deposit similar amounts of energy in the calorimeter, with less chances of depositing energy in the smaller first sampling. Hence, many events accumulate at $f_1 < 10\%$, as shown in the figure.

In figure 3.2c, the dimuon invariant mass is shown for simulated events with a reconstructed FSR photon. The emission of an FSR photon always leads to a reduced dimuon invariant mass ($m_{\mu\mu} < 91.18$ GeV), as can be seen in the mass distribution of events with a true FSR photon. In contrast, muon pairs that did not radiate any photon concentrate around the Z pole mass. If the fake FSR photons associated to these events were to be included in the mass calculation, the resonance shape would be distorted. Two distinct regions are defined by the S/B ratio, one corresponding to $S/B < 1$ (for $m_{\mu\mu} < 89$ GeV) and the other to $S/B > 1$ (for $m_{\mu\mu} > 89$ GeV). For this reason, only events with $m_{\mu\mu} < 89$ GeV are considered for FSR correction.

Applying an $m_{\mu\mu} < 89$ GeV cut, a purity map in (ΔR, f_1) was constructed for standard clusters ($E_T \geq 3.5$ GeV, figure 3.3a) and for toposeeded clusters ($E_T < 3.5$ GeV, figure 3.3b) separately. Purity was calculated as the ratio of truth-matched reconstructed photons divided by the total number of reconstructed photons. In the case of standard clusters, figure 3.3a shows that only the region with $f_1 < 10\%$ has a purity below 60%. Toposeeded clusters present a higher fake rate, with a purity below 60% for $f_1 < 20\%$ and for the higher values of ΔR, which stops the algorithm from being used to search for non-collinear FSR photons.

The selection of non-collinear (*far*) FSR photons is based on the optimised set of variables for the discrimination of photons from jets containing neutral particles that decay into photons ($\pi \rightarrow \gamma\gamma$), the so-called *Tight* photon identification criteria (see section 2.3.3). In figure 3.4a the $m_{\mu\mu}$ distribution of events with a reconstructed *far* FSR is shown. These photons are *Tight* and satisfy $\Delta R(\mu, \gamma) \geq 0.15$. As it was observed in the collinear case, events with fake (or very low energy) photons have a dimuon mass that agrees with the Z boson mass.

Having all these results in mind, the following selection criteria were defined and implemented in different Higgs searches ([28], [29]):

[1] See for example equation 6.1 for the formula applied to the case of fast electrons. For the general case see e.g. [27].

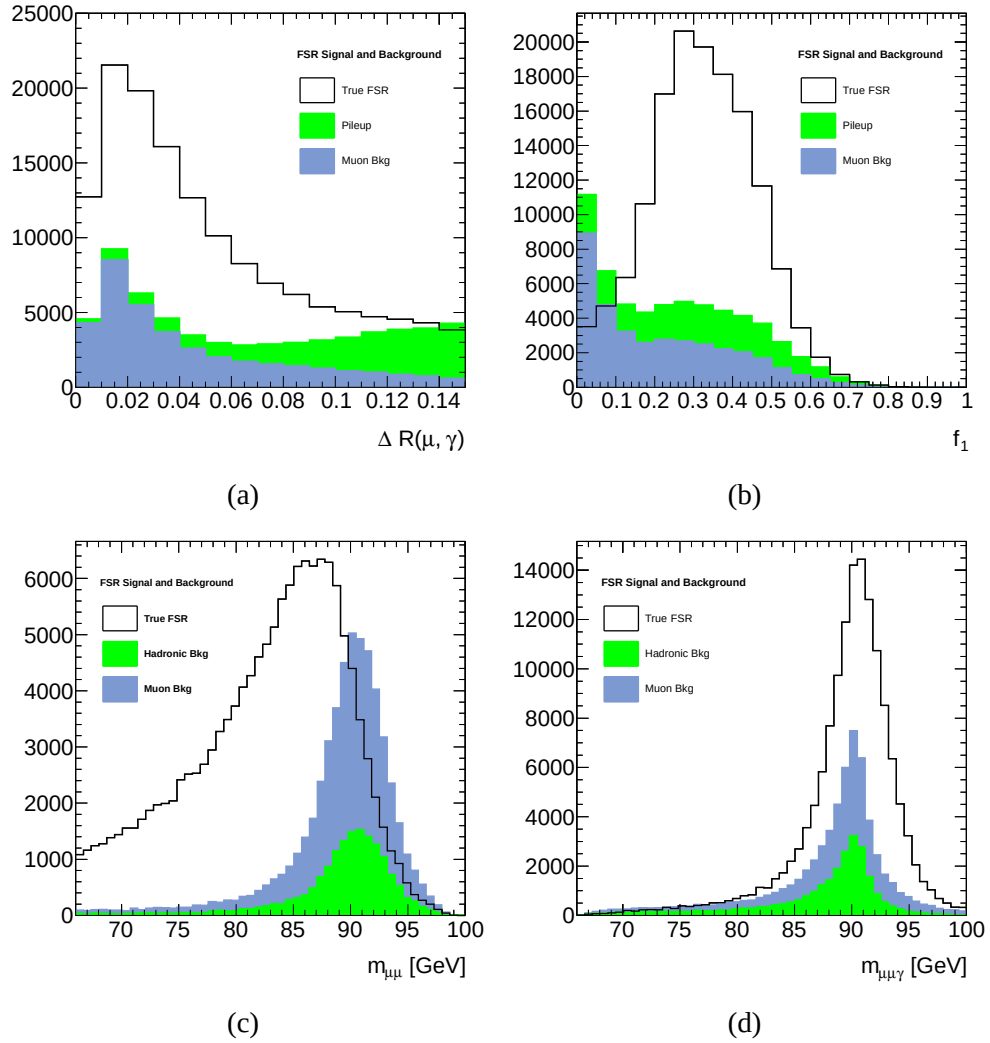

Figure 3.2: Distribution of true and fake collinear FSR photons as a function of the selection variables. Truth matched reconstructed FSR photons are shown as a white filled histogram. Reconstructed FSR photons matched to muon depositions (blue) and to particles from pile-up events (green) are stacked in the same histogram. (a) ΔR of the cluster with respect to the muon. Muon depositions take place along the muon track ($\Delta R \sim 0$), while hadronic events can take place anywhere. (b) Distribution of the proportion of energy left in the first calorimeter sampling with respect to the total energy deposition in the calorimeter (f_1). Most of the true FSR photons leave at least 10% of their energy in the first sampling. (c) Dimuon mass distribution. Events with a fake FSR lie in the Z mass resonance, while those requiring a true FSR correction belong to a different distribution. (d) Three-body invariant mass of the selected $Z \to \mu\mu\gamma$ events. Purity after all cuts is $\sim$ 85%.

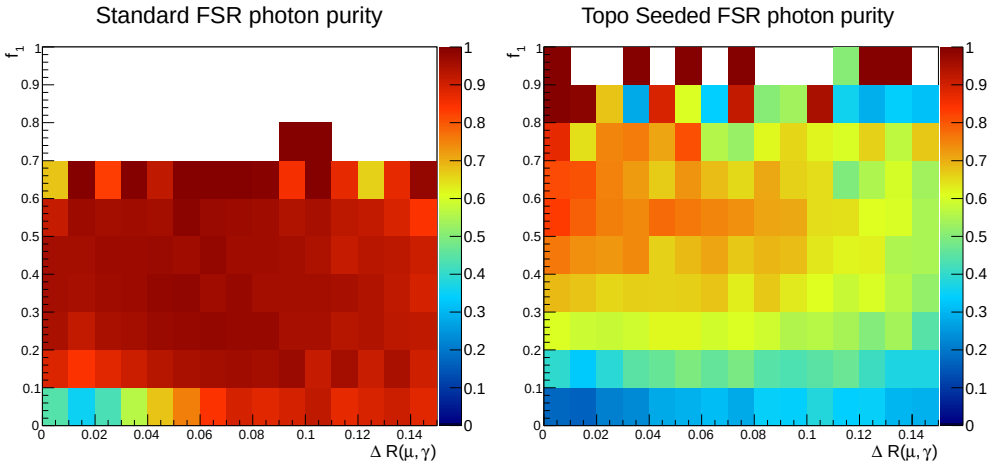

(a) (b)

Figure 3.3: Purity maps of the collinear FSR selection as a function of photon f_1 and $\Delta R(\mu, \gamma)$. Purity is calculated as the ratio of the number of truth matched reconstructed FSR photons and the total number of reconstructed FSR photons. (a) Purity map for standard photon clusters ($E_T \geq 3.5$ GeV). Purity is above 60% except for $f_1 < 10\%$. (b) Purity map for toposeeded clusters ($E_T < 3.5$ GeV). Fake rate is higher at lower energies. Purity is below 60% for $f_1 < 20\%$ and for the higher values of ΔR.

Collinear photon selection:

For $E_T \geq 3.5$ GeV (standard photon and electron clusters)

- $\Delta R(\mu, \gamma) < 0.15$
- Photon $f_1 > 0.1$

For $E_T < 3.5$ GeV (toposeeded clusters)

- $\Delta R(\mu, \gamma) < 0.08$
- Photon $f_1 > 0.2$

If the muon track passes through the photon cluster ($\Delta R(\mu, \gamma) < 0.05$), 400 MeV of energy are subtracted from the cluster to account for the average muon deposition in the calorimeter [29].

Photons reconstructed in the crack calorimeter region ($1.37 < |\eta| < 1.52$) or at $|\eta| > 2.37$ are discarded.

If more than one candidate is found, the cluster with the highest energy is chosen. The mass of the three body system cannot exceed 100 GeV, or the photon is discarded.

Figure 3.2d shows the three-body invariant mass distribution of $Z \rightarrow \mu^+\mu^-$ with an identified collinear FSR photon after all cuts. Signal events are now in the Z mass resonance distribution and purity is $\sim$ 85%.

Non-collinear photon selection:

If no collinear FSR candidates are found and the dimuon mass does not exceed 81 GeV, then a search is performed in the orthogonal space of the calorimeter ($\Delta R(\mu^+, \gamma) \geq 0.15$ and $\Delta R(\mu^-, \gamma) \geq 0.15$). *Tight* photon identification and $E_T > 10$ GeV is required. The mass of the final three body system cannot exceed 100 GeV, or the photon is discarded.

The non-collinear photon search is also performed with e^+e^- pairs, following the same procedure.

Figure 3.4b shows the three-body invariant mass distribution of $Z \rightarrow \mu^+\mu^-$ with an identified *far* FSR photon after all cuts. All signal events belong now to the *Z*-resonance distribution and purity is higher than 95%.

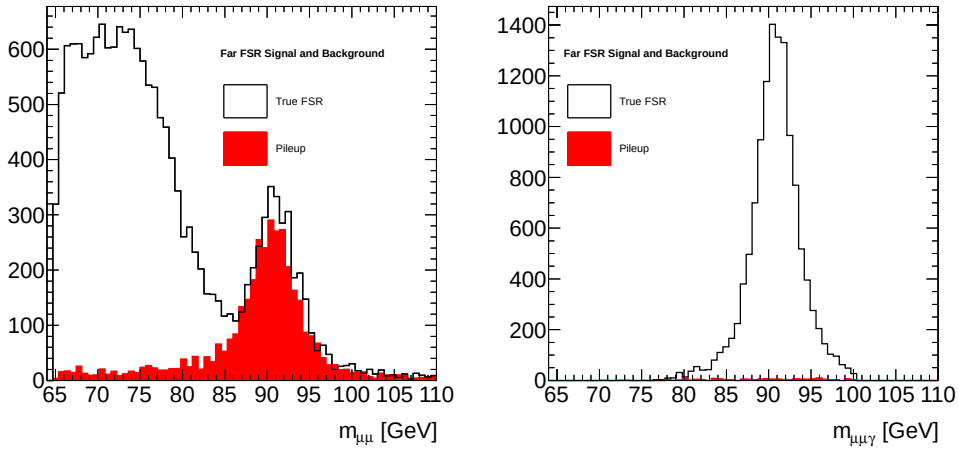

(a) (b)

Figure 3.4: Mass distribution of events with a reconstructed *far* FSR. (a) Dimuon invariant mass distribution. Events with fake reconstructed photons concentrate around the Z mass resonance, while events requiring FSR correction fall into a different distribution. (b) Three-body invariant mass of $Z \to \mu\mu\gamma$ events after all cuts. Purity is $\gtrsim 95\%$.

3.2 Performance of the FSR recovery procedure

The performance of the FSR recovery procedure in data was tested with a selection of $Z \to \mu^+\mu^-(\gamma)$ events in a dedicated study. Two oppositely charged muons with transverse momentum $p_T > 20$ GeV in the pseudorapidity range $|\eta| < 2.5$ were selected. The angular separation between them was required to be $\Delta R(\mu^+, \mu^-) \geq 0.1$ to avoid overlaps. The ratio of the sum of all track transverse momenta in a $\Delta R < 0.2$ cone around each muon and the respective muon track transverse momentum should be less than $\sum p_T / p_T(\mu) < 10\%$, while the ratio of the muon E_T and the sum of the calorimeter depositions in a $\Delta R < 0.2$ cone around it is required to be less than $\sum E_T / E_T(\mu) < 30\%$. The impact parameter significance of each muon is required to satisfy $d_0/\sigma_{d_0} < 3.5$.

FSR photon candidates are selected as described above. Figure 3.5a shows the $\Delta R(\mu, \gamma)$ distribution of FSR photons collinear to muons, and figures 3.5b and 3.5c show their f_1 and transverse energy E_T distributions in data (filled circles) and Monte Carlo (blue histogram). Figures 3.6a and 3.6b show the analogous ΔR and E_T distributions of non-collinear FSR photons. Figure 3.7 shows the mass distribution of all $Z \to \mu\mu$ events, with and without identified FSR candidates, before and after the FSR correction. In figure 3.8 the same distributions are shown, but restricted to those events with (a) collinear FSR photons and (b) non-collinear FSR photons identified. A very good agreement between data and Monte Carlo is seen before and after the FSR correction.

Efficiency is defined as the fraction of reconstructable true signal events that have actually been reconstructed, while purity is defined as the fraction of all reconstructed events that are true signal. The collinear selection has an efficiency of 70% in the recovery of FSR photons and a purity of 85%. The ratio of events with an identified collinear FSR to all $Z \to \mu\mu$ events is $\simeq 4\%$. In the case of the non-collinear selection, the efficiency is 60%, the purity of the selected photons is $> 95\%$ and the ratio of events with respect to the total number $\simeq 1\%$.

3.2.1 Systematic uncertainty from FSR correction

Assuming that PHOTOS correctly describes the FSR effects observed in data, the FSR correction may induce a systematic uncertainty in the mass scale and resolution of the

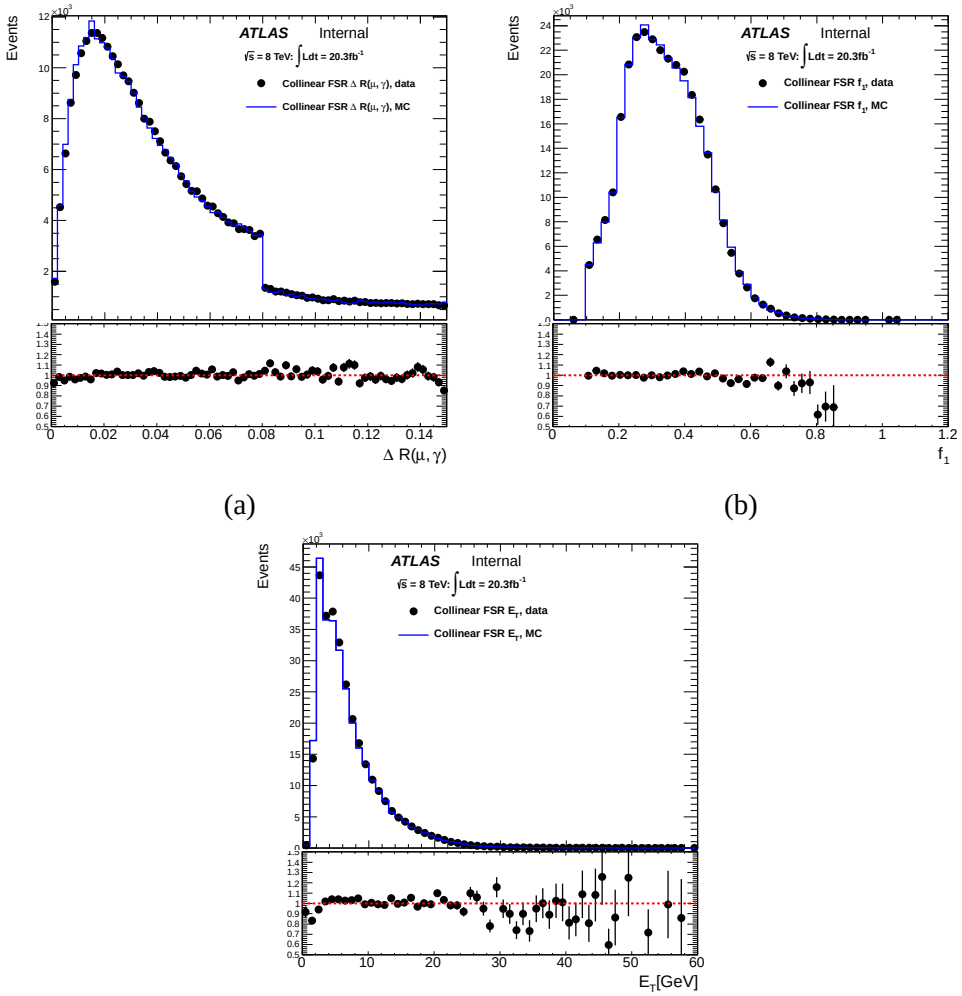

Figure 3.5: (a) Distribution of $\Delta R(\mu, \gamma)$ for FSR photons collinear to muons after all analysis cuts. The step in the distribution is due to the presence of both standard clusters ($\Delta R < 0.15$) and toposeeded clusters ($\Delta R < 0.08$). (b) Distribution of f_1 for FSR photons collinear to muons after all analysis cuts. (c) Transverse energy (E_T) distribution of all collinear FSR photons after all analysis cuts. The minimum available cluster transverse energy in the analysis is $E_T = 1.5$ GeV.

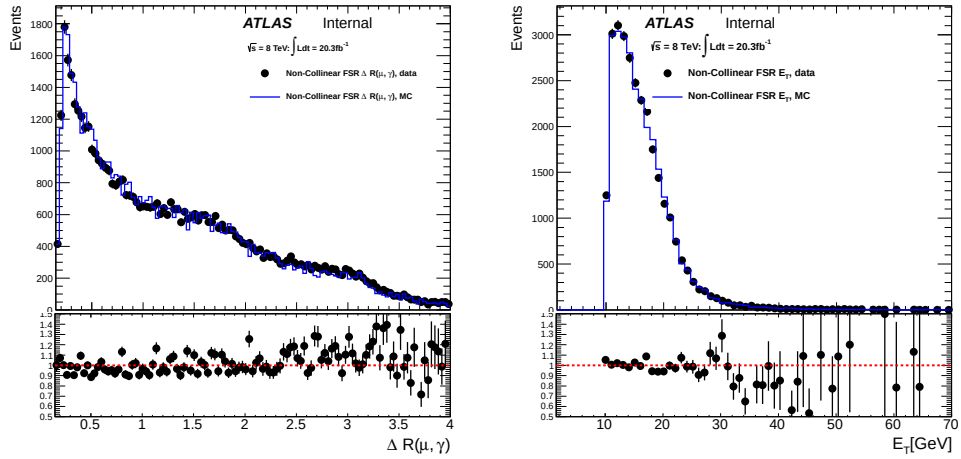

(a) (b)

Figure 3.6: (a) Distribution of the angular distance $\Delta R(\mu, \gamma)$ between non-collinear FSR photons and the closest muon of the event after all analysis cuts. (b) Transverse energy (E_T) distribution of all non-collinear FSR photons after all analysis cuts. An $E_T > 10$ GeV cut is applied for background removal.

$Z \to \mu\mu$ resonance due to the additional systematics associated to the photon scale and resolution.

The $Z \to \mu\mu$ distribution was fitted in the mass range (91.18 ± 3) GeV with a gaussian function before and after FSR correction. The results are shown in table 3.1 for data and Monte Carlo.

The correction shifts the gaussian mean by (+40 ± 3) MeV, and the resolution is improved by (3 ± 1)%. This change in the mass peak of the distribution will be affected by the photon energy scale uncertainty. Approximating this uncertainty by 0.5% (see chapter 4) the mass shift would indicate that the additional uncertainty is $40 \cdot 0.005$ MeV ~ MeV. The same result could have been estimated knowing that ~ 5% of events are corrected with a photon of average transverse energy $\langle E_T \rangle \sim 10$ GeV with an energy scale uncertainty of 0.5%. The additional uncertainty in the Z mass scale is $0.05 \cdot 0.005 \cdot 10$ GeV ~ MeV. This is negligible.

Assuming a systematic uncertainty of 10% in the photon resolution at an average $E_T \sim 10$ GeV [30], 5% of corrected events will induce an $\mathcal{O}(10)$ MeV negligible contribution to the resolution uncertainty.

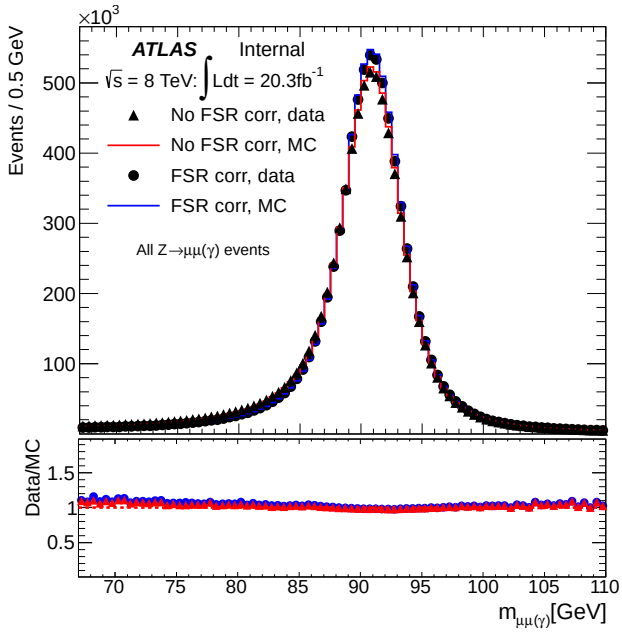

Figure 3.7: Invariant mass distribution of all $Z \to \mu^+\mu^-$ events in data before FSR correction (filled triangles) and after FSR correction (filled circles). The MC prediction is shown before correction (red histogram) and after correction (blue histogram). Both collinear and non-collinear corrections are shown.

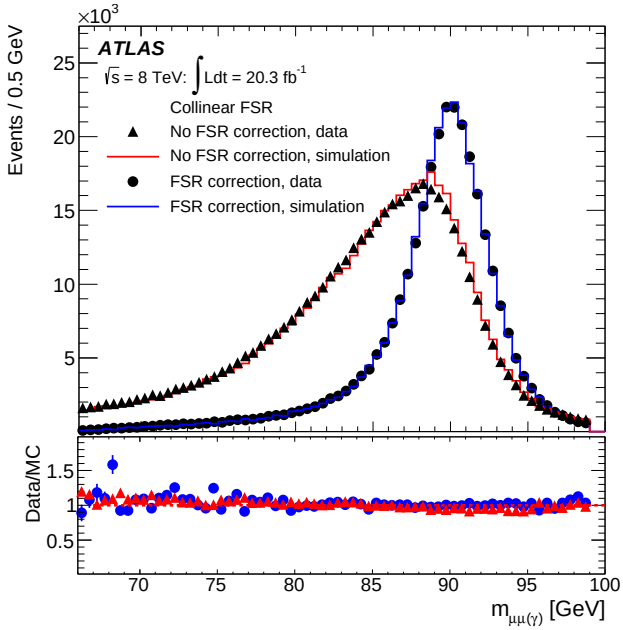

(a)

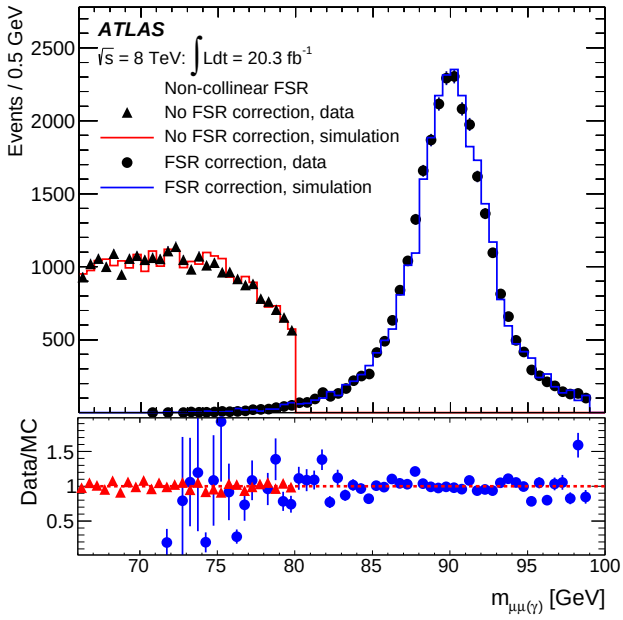

(b)

Figure 3.8: (a) The invariant mass distributions of $Z \to \mu^+\mu^-(\gamma)$ events in data before collinear FSR correction (filled triangles) and after collinear FSR correction (filled circles), for events with a collinear FSR photon satisfying the selection criteria as described in Sec. 3.1.2. The prediction of the simulation is shown before correction (red histogram) and after correction (blue histogram). (b) The invariant mass distributions of $Z \to \mu^+\mu^-(\gamma)$ events with a non-collinear FSR photon satisfying the selection criteria as described in Sec. 3.1.2. The prediction of the simulation is shown before correction (red histogram) and after correction (blue histogram).

Table 3.1: Results of the fit in the Z→ $\mu\mu$ distribution before and after FSR correction for data and MC. Uncertainties are statistical only.

Type	Mean ($m_{\mu\mu}$)	σ ($m_{\mu\mu}$)	Mean ($m_{\mu\mu\gamma}$)	σ ($m_{\mu\mu\gamma}$)
MC	90.869± 0.003	2.348±0.006	90.903±0.003	2.289±0.006
Data	90.848±0.002	2.362±0.004	90.884±0.002	2.296±0.004

3.2.2 Pile-up tests

The high luminosity of the LHC implies that for every hard pp scattering there can be dozens of soft interactions occurring simultaneously. During the 2012 $\sqrt{s}$ = 8 TeV pp run, an average of 20.7 of these pile-up events took place per hard scattering (see figure 3.9), and the average will grow when the centre-of-mass energy is increased. Pileup interactions affect the FSR correction procedure mainly in the form of hadronic background, but its effect is modelled by the Monte Carlo. Ensuring the quality of the modelling of FSR in the Monte Carlo under different pile-up conditions is necessary to avoid additional systematic uncertainties associated to the correction.

The dependence of the FSR correction on different pile-up conditions was tested collecting events in three categories defined by the average number of interactions per bunch crossing $\langle\mu\rangle$ and fitting the Z mass and resolution, comparing Data and Monte Carlo in each case. The categories are defined as $\langle\mu\rangle \in [0,17],(17,23],(23,40]$ to contain approximately $1/3$ of the $Z \to \mu\mu\gamma$ events each.

Collinear FSR	Fit result (Data)		Fit result (MC)	
$\langle\mu\rangle$	Mean/GeV	σ/GeV	Mean/GeV	σ/GeV
0 - 17	90.709 ± 0.016	1.888 ± 0.030	90.663 ± 0.016	1.993 ± 0.030
17 - 23	90.685 ± 0.016	2.019 ± 0.030	90.653 ± 0.018	2.066 ± 0.035
23 - 40	90.668 ± 0.016	2.067 ± 0.032	90.652 ± 0.019	2.027 ± 0.036

Table 3.2: Gaussian fits of $Z \to \mu\mu\gamma$ mass for collinear FSR events ($\Delta R(\mu,\gamma)< 0.15$, $E_{T,\gamma} > 1.5$ GeV). Fits performed with a Gaussian in a $\pm 1\sigma$ range around the mean determined by a pre-fit.

The mass distribution of $Z \to \mu^+\mu^-$ events with a collinear FSR photon identified is shown in figure 3.10 for the three different categories in data (black circles) and Monte

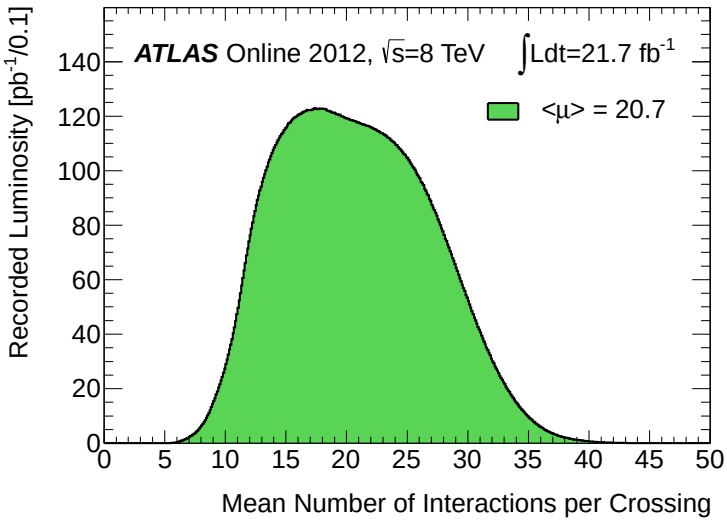

Figure 3.9: Luminosity-weighted distribution of the mean number of interactions per crossing for 2012 (full pp collisions dataset).

Carlo (red histogram). The result of the fits is shown in table 3.2. No variation is found within statistical uncertainties for the different $\langle\mu\rangle$ values, and the Monte Carlo simulation reproduces well the behaviour of the data. The analysis needs to be repeated when higher $\langle\mu\rangle$ collision events are available before the FSR selection procedure described here can be used with the new data.

Far FSR	Fit result (Data)		Fit result (MC)	
$\langle\mu\rangle$	Mean/GeV	σ/GeV	Mean/GeV	σ/GeV
0 - 17	90.979 ± 0.051	2.063 ± 0.098	90.949 ± 0.049	2.001 ± 0.092
17 - 23	90.974 ± 0.060	2.31 ± 0.12	91.131 ± 0.043	2.083 ± 0.092
23 - 40	91.147 ± 0.055	2.19 ± 0.10	91.140 ± 0.056	1.75 ± 0.098

Table 3.3: Gaussian fits of $Z \rightarrow \mu\mu\gamma$ mass for far FSR events ($\Delta R(\mu,\gamma) \geq 0.15$, $E_{T,\gamma} >$ 10 GeV). Fits performed with a Gaussian in a $\pm 1\sigma$ range around the mean determined by a pre-fit.

Similarly, the mass distribution of events with a non-collinear FSR photon identified is shown in figure 3.11. The fit results are shown in table 3.3. Again, there is good agreement between data and simulation and no significant $\langle\mu\rangle$ dependence is observed.

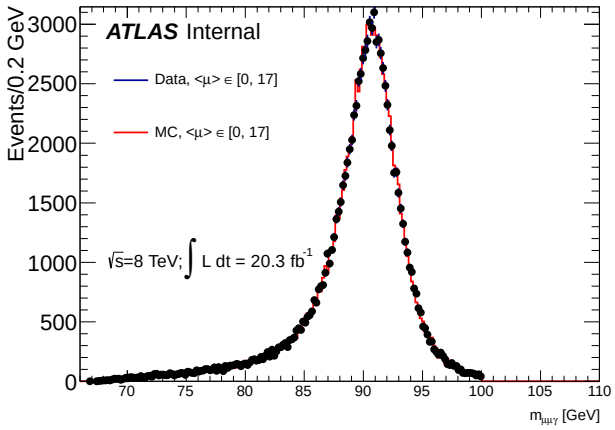

(a)

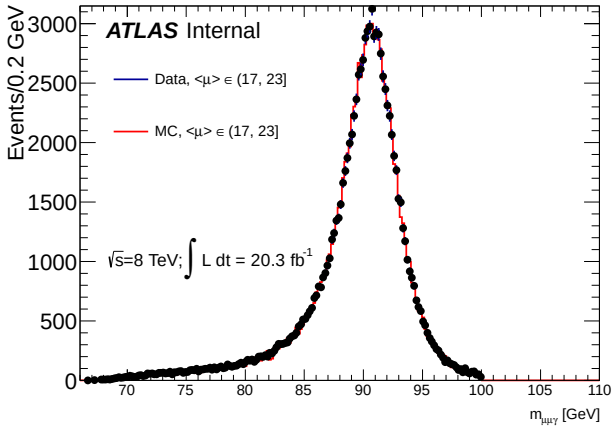

(b)

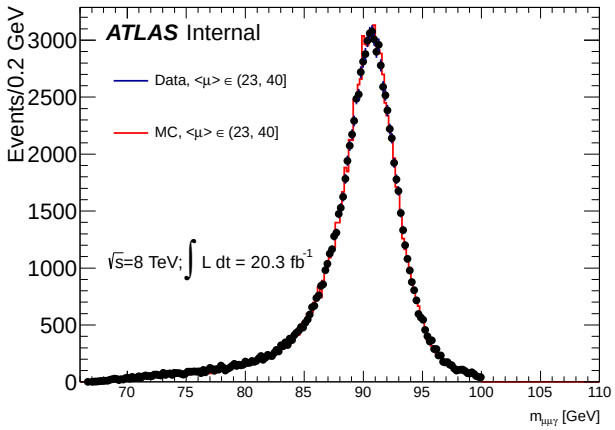

(c)

Figure 3.10: $m_{\mu\mu\gamma}$ mass distribution of all $Z \to \mu^+\mu^-$ events with a collinear FSR photon identified and (a) $\langle\mu\rangle \in [0, 17]$, (b) $\langle\mu\rangle \in (17, 23]$, (c) $\langle\mu\rangle \in (23, 40]$. Data are shown as black circles, Monte Carlo as a red histogram.

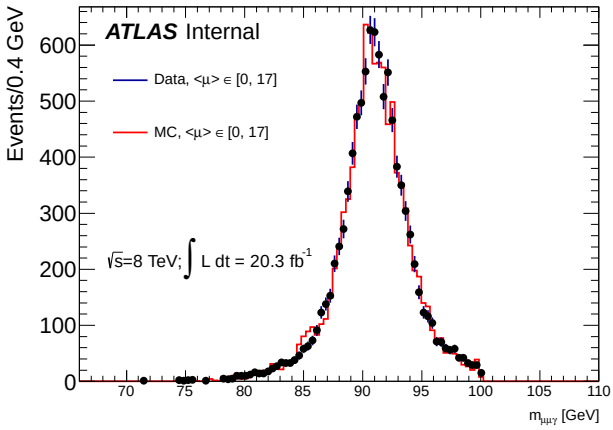

(a)

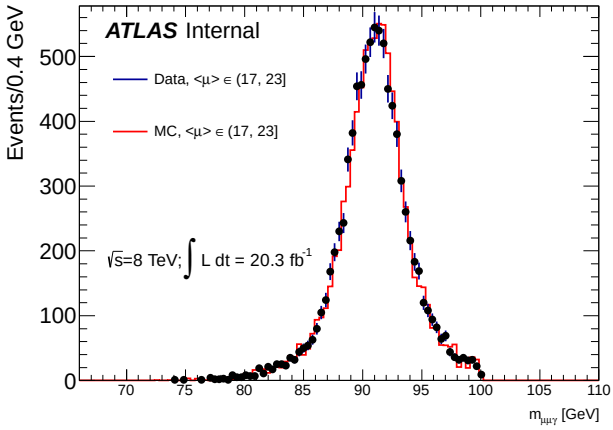

(b)

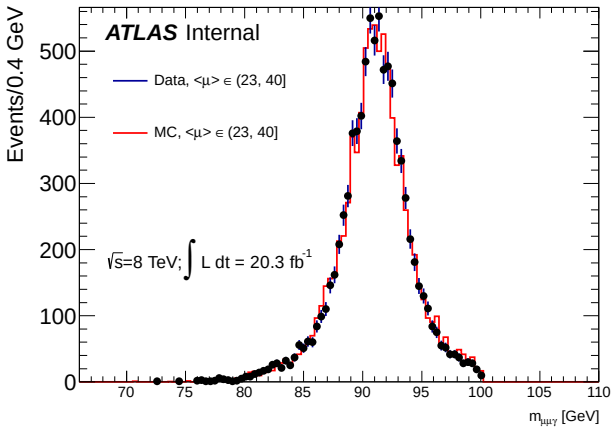

(c)

Figure 3.11: $m_{\mu\mu\gamma}$ mass distribution of all $Z \to \mu^+\mu^-$ events with a non-collinear FSR photon identified and (a) $\langle\mu\rangle \in [0, 17]$, (b) $\langle\mu\rangle \in (17, 23]$, (c) $\langle\mu\rangle \in (23, 40]$. Data are shown as black circles, Monte Carlo as a red histogram.

3.2.3 $H \to ZZ^* \to 4\ell$ FSR recovery and mass measurement

The first ATLAS physics analysis to adopt the FSR photon correction was the $H \to ZZ^* \to 4\ell$ search. The procedure can recover Higgs events falling outside the signal region due to radiation of photons in the final state. Only a small percentage of events are expected to be corrected, but given the low number of candidate signal events it is very important to recover as many as possible. As seen in figure 3.12 [31], the recovery of radiative photons improves the Higgs mass measurement by correcting events falling in the low-mass tail of the distribution.

In this analysis the correction is applied to the 4-lepton events that pass all selection criteria. Only one FSR photon is selected per event, after searching for collinear ($\mu^\pm$ only) and non-collinear ($\mu^\pm$ and $e^\pm$) FSR photon candidates. A total of 3 events out of 60 Higgs candidate events were corrected, 1 collinear FSR (2.4 expected) and 2 non-collinear FSR (0.6 expected). See table 3.4 for a summary of the corrected events.

Channel	$m_{4\ell}$	$m_{4\ell}$ + FSR corr.	$m_{4\ell}$ + FSR + m_Z const.
4μ	113.425	123.527 (far FSR)	123.736
$2\mu 2e$	109.911	123.955 (coll. FSR)	126.754
$2\mu 2e$	95.771	126.453 (far FSR)	126.765

Table 3.4: 4-lepton candidate event masses before and after FSR correction and Z mass constraint with $m_{4\ell} \in (110, 140)$ GeV. Masses given in GeV.

The Higgs mass in the $H \to 4\ell$ channel is measured to be $m_H = 124.51 \pm 0.52$ GeV [32] as a result of the fit shown in figure 3.13.

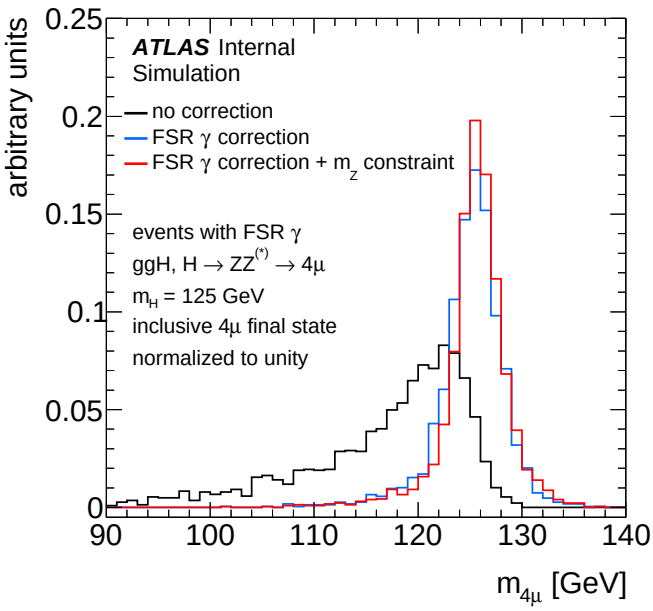

Figure 3.12: Mass distribution of simulated $H \to ZZ^* \to 4\mu$ events with mass m_H = 125 GeV with an identified FSR photon. The mass distribution before any correction is shown (black line) and after the FSR photon is recovered (blue line). The effect of applying the Z mass constraint for the events corrected for FSR is also shown (red line).

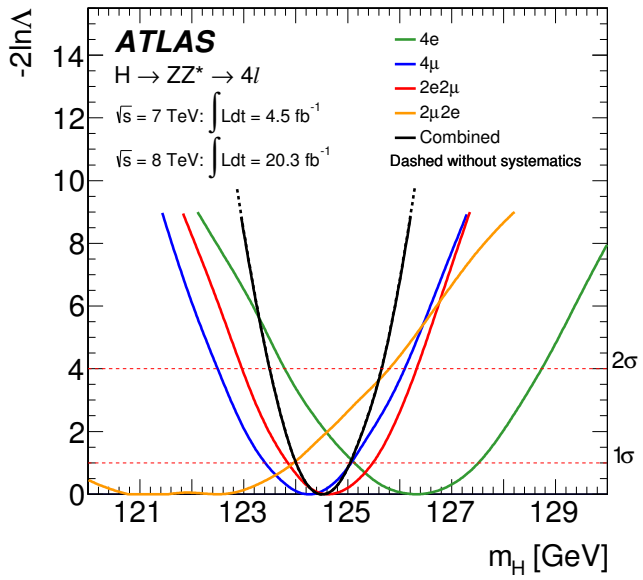

Figure 3.13: The profile likelihood as a function of m_H for the combination of all $H \to ZZ^* \to 4\ell$ channels and for the individual channels for the combined 7 TeV and 8 TeV data samples. The combined result is shown both with (solid line) and without (dashed line) systematic uncertainties, and the two results are almost indistinguishable. From [32].

Chapter 4

Electromagnetic Calorimeter energy scale control measurements with QED FSR photons

The Z resonance is used to set the absolute energy scale of the Electromagnetic Calorimeter. The calibration applied to photons is determined with $Z \rightarrow e^+e^-$ events. The behaviour of electrons is extrapolated to photons, even if not identical, since the only available standard candle for electromagnetic calibration at $E \sim 10^2$ GeV is the Z boson decaying into electron-positron pairs.

4.1 Energy scale calibration with electrons from $Z \rightarrow ee$ decays

In situ electron scales are extracted using a $Z \rightarrow ee$ sample and cross checked with a $J/\Psi \rightarrow ee$ sample [33]. The scales are intended to correct the reconstructed electromagnetic energy for any residual mis-calibration due to calorimeter inhomogeneities or incorrect passive material determination. The correction is parametrised as:

$$E_i^{\text{reco}} = E_i^{\text{true}}(1 + \alpha_i) \tag{4.1}$$

where E^{reco} is the reconstructed electron energy, E^{true} is the true electron energy and i runs over the pseudorapidity bins. The mass of a di-electron event, neglecting the electron mass, is given by

$$M = \sqrt{E_1 E_2 \cos\theta_{12}} \tag{4.2}$$

where θ_{12} is the angle between the two electrons with reconstructed energy E_1 and E_2 respectively. Parametrising the energy as above, we have

$$M_{ij}^{\text{reco}} = \sqrt{(1+\alpha_i)(1+\alpha_j)}\, M^{\text{true}} \simeq (1 + \frac{\alpha_i + \alpha_j}{2}) M^{\text{true}} = (1 + \frac{\beta_{ij}}{2}) M^{\text{true}}. \tag{4.3}$$

Here M^{reco} is the reconstructed mass of the event with two electrons and M^{true} is the true mass. The so-called lineshape fit method estimates β_{ij} and calculates α_i and α_j fitting a Monte Carlo template to the data. The bias introduced in the generation of the template is estimated and corrected by applying the method to the Monte Carlo sample itself.

The results from the lineshape fit method are obtained from a sample of events with two electrons satisfying the medium criteria from the decay of a Z boson, with $E_T > 27$ GeV and $|\eta| < 2.47$. The fits are performed in the range $m_{ee} \in (80, 100)$ GeV. The achieved precision in the determination of the scale is on the order of $2 \cdot 10^{-4}$, and the results are shown in Figure 4.1.

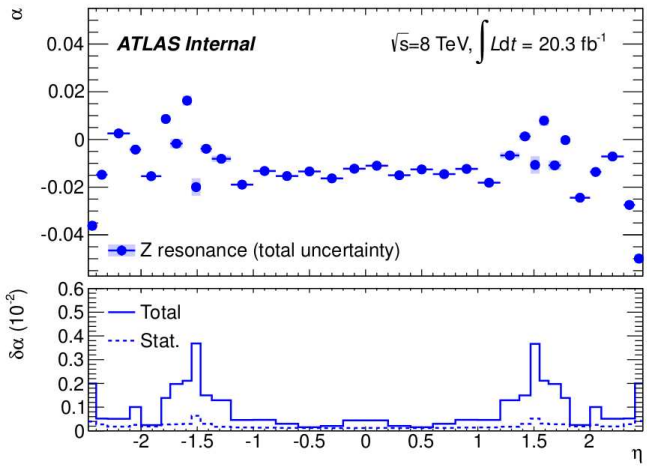

Figure 4.1: Top: electron scales as a function of η obtained from a $Z \to ee$ sample applying the lineshape fit method. Bottom: statistical and total uncertainties.

A cross check of the linearity of response using lower energy $J/\Psi \to ee$ elec-

trons shows that discrepancies are accounted for by the extrapolation of the systematic uncertainties to the lower energy range, as seen in figure 4.2.

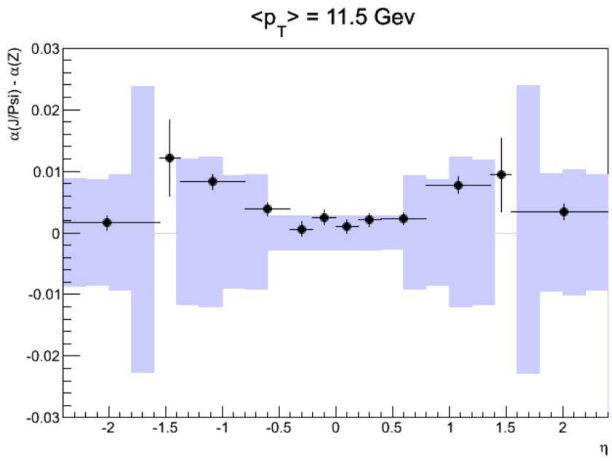

Figure 4.2: Difference in electron scales between Z and J/Ψ samples as a function of η (black points) with total uncertainty bars, applying the lineshape fit method. The error bands represent the a priori systematic uncertainty derived from the extrapolation of the Z-based calibration to $\langle E_T \rangle$ = 11.5 GeV.

4.1.1 Sources of systematic uncertainty

Calibration uncertainties are determined from the accuracy of the $Z \rightarrow ee$ method for the average electron transverse energy $\langle E_T^e \rangle \sim 40$ GeV from $Z \rightarrow ee$ decays. Other sources introduce energy and particle-type dependent effects that shift the energy scale by a given amount. The $Z \rightarrow ee$ based calibration offsets all effects affecting electrons with $E_T = \langle E_T^e \rangle$, hence the uncertainties are defined as:

$$\delta E_i^{e,\gamma}(E_T, \eta) = \Delta E_i^{e,\gamma}(E_T, \eta) - \Delta E_i^{e}(\langle E_T^e \rangle, \eta) \tag{4.4}$$

for each source of uncertainty i.

Table 4.1 shows the series of uncertainties common to electrons and photons estimated for unconverted photons with $E_T = 60$ GeV. The energy response of the calorimeter is affected by: the gain setting at which the calorimeter cells are recorded (Medium Gain or High Gain), which depends on the energy deposition in the cell; the

offset in the energy pedestal of electrons and photons, which induces an energy non-linearity mainly affecting low-energy particles; the uncertainty from the Presampler and calorimeter L1/L2 calibration, that depends on the fraction of energy deposited in those layers (f_{PS}, f_{L2}); the passive material uncertainties (ID, Calorimeter, Cryostat), estimated from simulations with modified material. The sources of uncertainty are considered independent and added in quadrature.

	Unconverted photons, $E_{\text{T}} = 60$ GeV				
$\|\eta\|$ range	0–0.6	0.6–1	1–1.37	1.55–1.82	1.82–2.47
$Z \to ee$ calibration	0.03	0.04	0.08	0.16	0.05
Gain, pedestal	0.03	0.02	0.01	0.89	0.55
Layer calibration	0.15	0.20	0.20	0.25	0.26
ID material	0.06	0.12	0.19	0.07	0.12
Other material	0.09	0.17	0.40	0.96	0.09
Total	0.19	0.31	0.50	1.35	0.63

Table 4.1: Summary of energy scale systematic uncertainty contributions from sources common to electrons and photons, estimated for unconverted photons with $E_{\text{T}} = 60$ GeV, in percent [30].

Tables 4.2 and 4.3 show the different systematic uncertainties affecting the photon energy scale exclusively. Photons cannot be reconstructed in the calorimeter crack region, $|\eta| \in (1.37, 1.52)$, which is excluded.

Uncertainty	$\|\eta\| < 0.6$	$0.6 \leq \|\eta\| < 1.37$	$1.52 \leq \|\eta\| < 1.81$	$1.81 \leq \|\eta\| < 2.37$
Inefficiency	0.02	0.03	0.10	0.02
Fake Rate	0.01	0.06	0.06	0.03

Table 4.2: Impact on the energy scale of unconverted (converted) photons from the additional inefficiency (fake rate) in four pseudorapidity bins, in percent [30].

Particle type	$\|\eta\| < 0.8$	$0.8 \leq \|\eta\| < 1.37$	$1.52 \leq \|\eta\| < 2.37$
$\Delta(\gamma - e)$, converted	0.16 ± 0.11	0.46 ± 0.10	0.19 ± 0.10
$\Delta(\gamma - e)$, unconverted	0.03 ± 0.04	0.10 ± 0.06	0.05 ± 0.04

Table 4.3: Difference between out-of-cluster energy loss for electrons and photons, $\Delta(\gamma - e)$, in percent [30].

4.2 Cross-check of photon scales with Z radiative decays

As mentioned before, electron scales are applied to photons despite the fact that their behaviour is not identical. This extrapolation must therefore be validated to ensure a proper photon calibration. A data-driven study of radiative Z decays was performed for this reason. Collinear FSR photons from $Z \to \mu\mu\gamma$ decays were used and the results were later combined with non-collinear FSR results from $Z \to \mu\mu$ and $Z \to ee$ radiative decays.

4.2.1 The double ratio method

After the application of the in situ calibration to photons in data and Monte Carlo[1], any residual mis-calibration affecting the photon energy can again be parametrised as:

$$E_i^{\text{reco}} = E_i^{\text{true}}(1 + \alpha_i) \tag{4.5}$$

where the index i refers to a photon η region or E_T range. E^{reco} is the scale-corrected reconstructed photon energy and E^{true} is the true photon energy. The three-body invariant mass of the Z radiative decay events is measured and data is compared to Monte Carlo. To determine the value of α, the photon energy in data is shifted by different amounts $(1+\alpha)$, and the value providing the best agreement is taken as the photon energy scale.

As a way to quantify the agreement, the so-called double ratio method is used. It relies on the following double ratio:

$$R(\alpha) = \frac{\langle m(\,\ell\ell\gamma(\alpha))_{\text{data}}\rangle / \langle m(\ell\ell)_{\text{data}}\rangle}{\langle m(\ell\ell\gamma)_{\text{MC}}\rangle / \langle m(\ell\ell)_{\text{MC}}\rangle}, \tag{4.6}$$

where $\langle m(\ell\ell)_{\text{data}}\rangle$ and $\langle m(\ell\ell)_{\text{MC}}\rangle$ are the mean value of the fit of the $Z \to \ell\ell$ non-radiative event distribution from data and from Monte Carlo, respectively. The term $\langle m(\,\ell\ell\gamma(\alpha))_{\text{data}}\rangle$ is the mean of the fit of the distribution of radiative $Z \to \ell\ell\gamma$ events in data, with the photon energy shifted by $(1+\alpha)$. The same applies for $\langle m(\ell\ell\gamma)_{\text{MC}}\rangle$, but with no injected shift. The value of α for which $R = 1$ is taken as the photon energy

[1] Monte Carlo photon E_T is smeared to match the observed $Z \to ee$ energy resolution

scale.

The $m_{\ell\ell\gamma}/m_{\ell\ell}$ ratio is intended to cancel any lepton scale uncertainties. If one shifts $E_\ell \to E_\ell/(1+\Delta)$, then at first order in Δ:

$$m_{\ell\ell\gamma} \to m_{\ell\ell\gamma}(\Delta) = \frac{m_{\ell\ell\gamma}}{1+\Delta}\left(1 - \frac{\Delta}{2}\left[1 - \frac{m_{\ell\ell}^2}{m_{\ell\ell\gamma}^2}\right]\right) \tag{4.7}$$

Similarly, shifting $E_\gamma \to E_\gamma/(1+\alpha)$ and neglecting all terms but $\mathcal{O}(1)$ in α

$$m_{\ell\ell\gamma} \to m_{\ell\ell\gamma}(\alpha) = m_{\ell\ell\gamma}\left(1 + \frac{\alpha}{2}\left[1 - \frac{m_{\ell\ell}^2}{m_{\ell\ell\gamma}^2}\right]\right) \tag{4.8}$$

So applying both simultaneously:

$$m_{\ell\ell\gamma}(\alpha,\Delta) = \frac{m_{\ell\ell\gamma}}{1+\Delta}\left(1 + \frac{\alpha}{2}\left[1 - \frac{m_{\ell\ell}^2}{m_{\ell\ell\gamma}^2}\right]\right)\left(1 - \frac{\Delta}{2}\left[1 - \frac{m_{\ell\ell}^2}{m_{\ell\ell\gamma}^2}\right]\right) \tag{4.9}$$

Given that $1 - x \simeq (1+x)^{-1}$ for $x \to 0$:

$$m_{\ell\ell\gamma}(\alpha,\Delta) = \frac{m_{\ell\ell\gamma}}{1+\Delta}\left(1 + \frac{\alpha}{2}\left[1 - \frac{m_{\ell\ell}^2}{m_{\ell\ell\gamma}^2}\right]\right)\left(1 + \frac{\Delta}{2}\left[1 - \frac{m_{\ell\ell}^2}{m_{\ell\ell\gamma}^2}\right]\right)^{-1} \tag{4.10}$$

The value of α (i.e. the systematic uncertainty on α) required to cancel the effect coming from Δ is:

$$\sigma_\alpha = \Delta\left(1 + \frac{2}{1 - \frac{m_{\ell\ell}^2}{m_{\ell\ell\gamma}^2}}\right) \tag{4.11}$$

However, when dividing $m_{\ell\ell\gamma}$ by $m_{\ell\ell}$, since the latter is also shifted by $(1+\Delta)$:

$$\frac{m_{\ell\ell\gamma}(\alpha,\Delta)}{m_{\ell\ell}(\Delta)} = \frac{m_{\ell\ell\gamma}}{m_{\ell\ell}}\left(1 + \frac{\alpha}{2}\left[1 - \frac{m_{\ell\ell}^2}{m_{\ell\ell\gamma}^2}\right]\right)\left(1 + \frac{\Delta}{2}\left[1 - \frac{m_{\ell\ell}^2}{m_{\ell\ell\gamma}^2}\right]\right)^{-1} \tag{4.12}$$

And the systematic uncertainty in α is reduced to simply:

$$\sigma_\alpha = \Delta \tag{4.13}$$

In the selected events, $\frac{m_{\ell\ell}}{m_{\ell\ell\gamma}} \sim 0.85$, so the ratio reduces the impact of Δ on α by ~ 8.

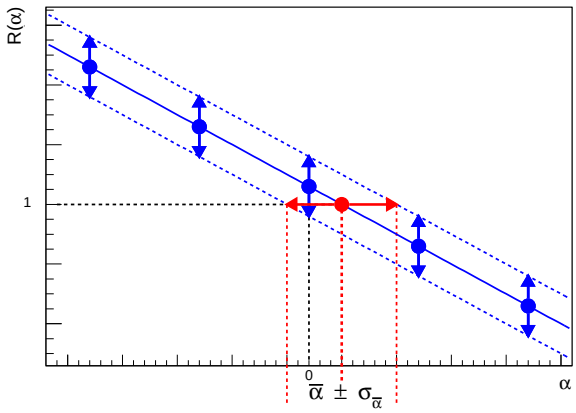

Figure 4.3: Schematic representation of the double ratio method

As shown in Figure 4.3, the value of α for which $R(\alpha) = 1$ is the photon energy scale.

4.2.2 Data and Monte Carlo samples

All $Z \to \mu\mu$ candidate events found in the 2012 proton-proton collision data collected at $\sqrt{s}$ = 8 TeV (20.3 fb^{-1}) are used.

The simulated $Z \to \mu\mu(\gamma)$ events were generated using SHERPA 1.4.1 run with the CT10 PDF family at NLO with up to three additional partons produced in the hard scattering with matrix elements calculated at LO. A cross-check was performed using events generated with the ALPGEN [23] generator, with CTEQ6L1 PDFs at LO with LO α_s and with up to five additional partons in the hard scattering process, then interfaced to PYTHIA [24] (Perugia2011C tune) for hadronization and showering. The effects of QED radiative corrections are calculated with PHOTOS [25], a package dedicated to the decay of resonant states. All events are fully simulated with GEANT4 [26], including pileup. Weighting is applied to match the average number of interactions per bunch crossing to the measured value.

4.2.3 Event selection

Events are required to have two oppositely-charged muons with a mass in the window $m_{\mu\mu} \in (55, 116)$ GeV. If a photon of $E_T > 7$ GeV, $f_1 > 10\%$ and $\Delta R(\mu, \gamma) < 0.15$ is found, the dimuon mass is required to be $m_{\mu\mu} < 89$ GeV, or else it is rejected as background. Events with photons are then required to have a three-body invariant mass of $m_{\mu\mu\gamma} \in (55, 116)$ GeV.

These cuts yield a photon purity of $\sim$ 97% estimated from Monte Carlo simulations. The main backgrounds affecting the selection are Z+jets containing photons from $\pi^0 \to \gamma\gamma$ or other neutral hadron decays, as well as muon energy depositions in the calorimeter.

Details of the selection are in Tables 4.4 and 4.5

Muons	
Trigger	Single μ with $p_T > 24$ GeV, dimuon with both $p_T(\mu) > 13$ GeV or $p_T(\mu_1) > 18$ GeV and $p_T(\mu_2) > 8$ GeV
General Cuts:	Muons with a Z position $\lvert Z_{\rm PV}\rvert$ <10 mm to the primary vertex Pseudo-rapidity region in $\lvert\eta\rvert$ <2.4
Identification:	Tight Identification criteria
Isolation:	Ptcone20/$p_{\rm T}$ < 0.10
$p_{\rm T}$ min:	$p_{\rm T} > 20$ GeV
ID Cuts:	Pixel b-layer hit unless the extrapolated muon track passes by an un-instrumented or dead area of the b-layer
	N pixel hits+N crossed dead pixel sensors > 0 N SCT hits+N crossed crossed dead SCT sensors > 4
	N pixel holes+N SCT holes < 3
Muons with 0.1 < $\lvert\eta\rvert$ <1.9:	N TRT hits(nTRTh)+N TRT outliers hits(nTRToh)>5(nTotal) nTRToh/nTotal > 0.9
Rest of muons:	If nTotal >5 then nTRToh/nTotal > 0.9

Table 4.4: Selection criteria applied on muon candidates.

4.2.4 Results

Photon energy scales are calculated in bins of photon pseudorapidity and transverse energy, using two different generators, Alpgen and SHERPA to check for variations in

Photons	
General Cuts:	Pseudo-rapidity region $\|\eta\| < 1.37$ or $1.52 < \|\eta\| < 2.37$
E_{T} min:	$E_{\mathrm{T}} > 7$ GeV
ΔR:	Angular distance muon-photon $\Delta R(\mu, \gamma) < 0.15$
f_1:	Fraction of energy deposited in first layer $f_1 > 10\%$

Table 4.5: Selection criteria applied on photon candidates.

the scale.

Various kinematic distributions for $Z \to \mu\mu$ events with a collinear FSR identified are shown in figures 4.4 (η), 4.5 (E_T), 4.6 (f_1) for Alpgen (left) and Sherpa (right). The mass distribution of all $Z \to \mu\mu\gamma$ events is shown in figure 4.7, while the mass distribution of all $Z \to \mu\mu$ events is shown in figure 4.8, again for Alpgen (left) and Sherpa (right).

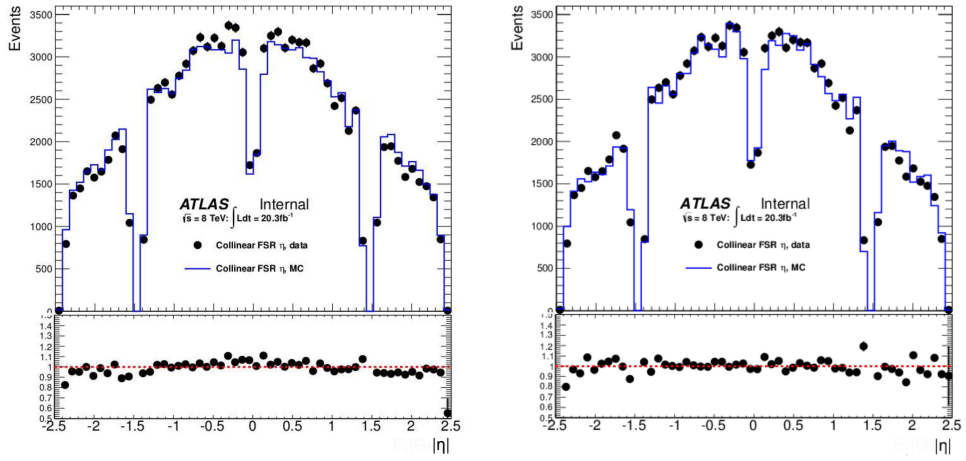

Figure 4.4: Comparison between data and Alpgen (left) and Sherpa (right) of the $Z \to \mu\mu\gamma$ collinear FSR photon η distribution.

Photon categorisation

The photon scales are calculated in η and E_T regions chosen to adapt to cuts used in various physics analyses, like the $H \to \gamma\gamma$ analysis, and such that there is sufficient statistics in each bin to obtain a reliable and stable result. The binning is set to be the

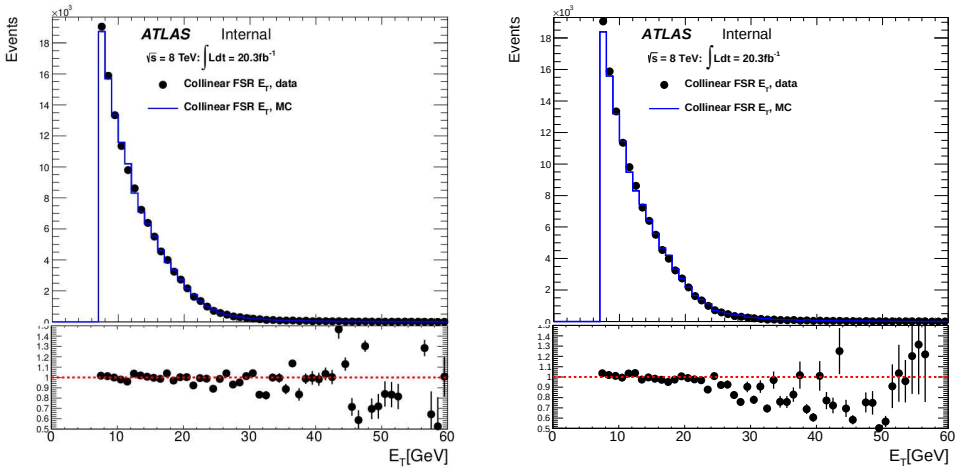

Figure 4.5: Comparison between data and Alpgen (left) and Sherpa (right) of the $Z \rightarrow \mu\mu\gamma$ collinear FSR photon E_T distribution.

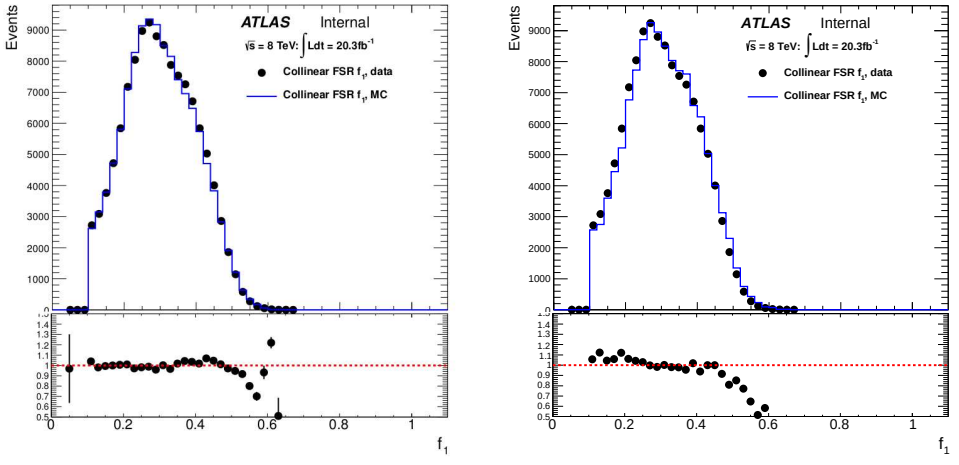

Figure 4.6: Comparison between data and Alpgen (left) and Sherpa (right) of the $Z \rightarrow \mu\mu\gamma$ collinear FSR photon f_1 distribution.

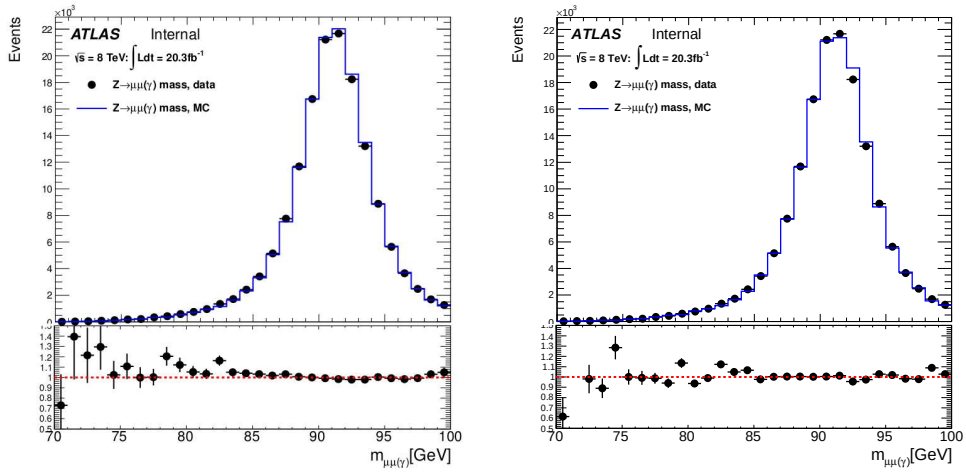

Figure 4.7: Comparison between data and Alpgen (left) and Sherpa (right) of the $m_{\mu\mu\gamma}$ mass distribution in $Z \rightarrow \mu\mu\gamma$ collinear FSR events.

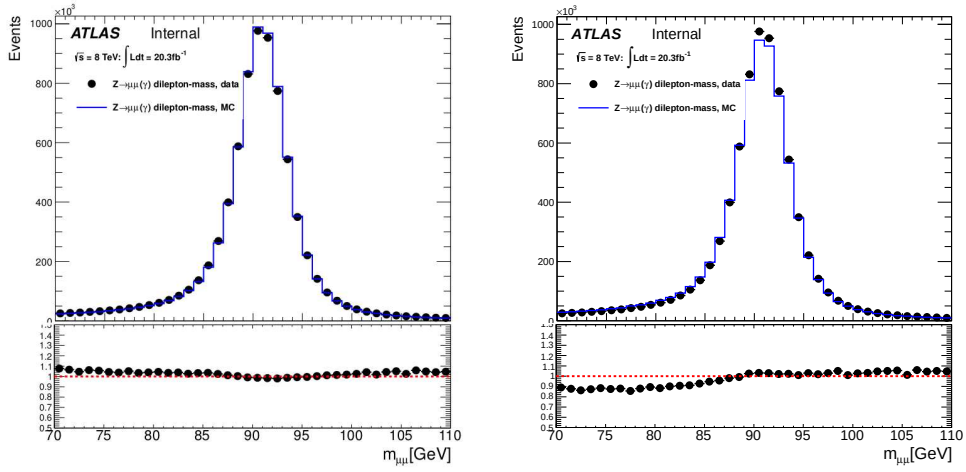

Figure 4.8: Comparison between data and Alpgen (left) and Sherpa (right) of the $m_{\mu\mu}$ mass distribution for all $Z \rightarrow \mu\mu$ events.

following:
E_T bins : $\{7, 10, 15, 20, 30, 100\}$ GeV
$|\eta|$ bins : $\{0.0, 0.6, 1.37, 1.52, 1.81, 2.37\}$
Each set of bins is used independently to check for linearity and uniformity of the calorimeter scale.

Fit procedure

The double ratio previously described (section 4.2.1) requires the mass distributions to be fitted to extract the mean values for the $R(\alpha)$ formula. The approach taken in this analysis has been to fit the distributions to a Gaussian in a mass window defined by 1.5σ of a previous fit.

Systematic uncertainties

The scale extraction was performed applying systematic variations of the different corrections and methods employed. These include (a) muon scale and (b) resolution uncertainties, (c) fit range, (d) background contamination.

In all cases, the scale extracted from the Double Ratio method was different from the nominal scale by less than the statistical uncertainty ($10^{-3} \sim 10^{-4}$).

In the case of (a), the Double Ratio method was designed to remove this effect (see equation 4.10). Also, the symmetry of the $m_{\mu\mu}$ distribution cancels any effect coming from (b). To check the impact of muon scale and resolution uncertainties, the procedure recommended by the ATLAS Muon Combined Performance group is followed. The muon momentum in Monte Carlo is shifted as a function of the ID and MS measured momenta and the combined (CB) momentum. This is done separately for the resolution and the scale. A total systematic uncertainty of 0.1% was found.

To check the effect of varying the fit range (c), the scale was extracted with ranges different from 1.5σ. Ranges of 1.2σ, 1.7σ and 2.0σ yielded results that differed on average by less than $\sim 10^{-4}$.

A systematic arising from background contamination was checked by calculating the scales with a pure Monte Carlo sample (true collinear photons only). The same procedure was followed excluding the 3% fake events, and the effect was found to be negligible.

Extracted scales

The photon energy scale α was extracted applying the Double Ratio method with the η and E_T binning previously mentioned. The results for the two different generators are shown in figures 4.9 and 4.10. The scales are shown after the $Z \to ee$ scale correction. The violet band around the electron scale line at zero is the quadratic sum of the different systematic uncertainties affecting the $Z \to ee$ scales, as described in section 4.1.1. The vertical uncertainties associated to the photon scales are statistical uncertainties and systematic uncertainties added in quadrature.

The photon scales are consistent with the electron scales in all cases and they are generator independent within uncertainties. The average difference between generators is 0.004 ± 0.005, which is consistent with zero.

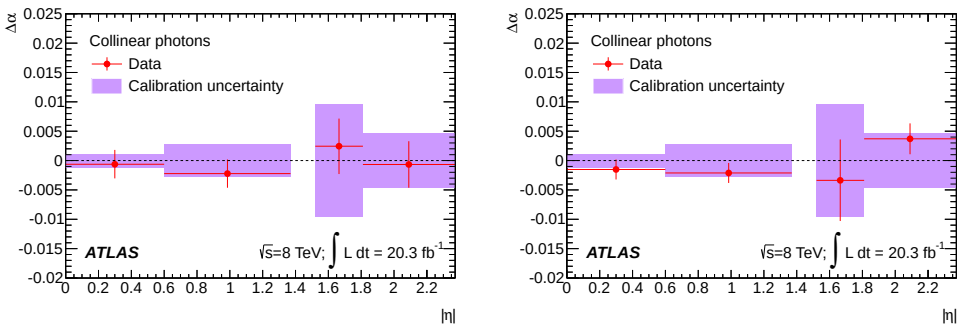

Figure 4.9: Scale factor from collinear FSR photons in bins of photon η (circles) calculated with respect to Alpgen (left) and Sherpa (right). The violet band around zero represents the systematic uncertainty associated to the electron scale from $Z \to ee$ calculations. The vertical uncertainties on the points are statistical and systematic added in quadrature. The barrel−end-cap crack region $|\eta| \in (1.37, 1.52)$ is excluded.

These results are consistent with the scales extracted from an orthogonal selection (non-collinear FSR) in the $Z \to \mu\mu$ and $Z \to ee$, as presented in [34], and can therefore be combined for a more precise cross-check of the calibration.

Combination

A similar selection of FSR photons was performed using the same SHERPA samples in the $Z \to \mu\mu$ and $Z \to ee$ channels. Photons were selected in di-lepton events

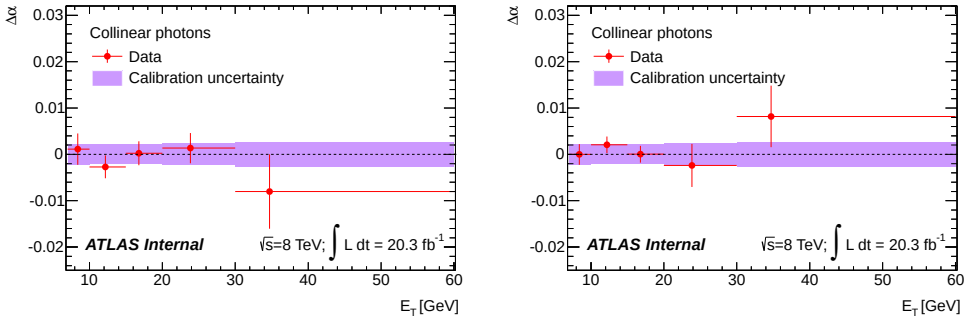

Figure 4.10: Scale factor from collinear FSR photons in bins of photon E_T (circles) calculated with respect to Alpgen (left) and Sherpa (right). The violet band around zero represents the systematic uncertainty associated to the electron scale from $Z \to ee$ calculations. The vertical uncertainties on the points are statistical and systematic added in quadrature.

with $\Delta R(\ell, \gamma) > 0.2$ (0.4) for $\ell = \mu^{\pm}$ ($e^{\pm}$), $p_T > 10$ GeV. Tight photon identification and $E_{T\text{cone40}} < 4$ GeV isolation was required to remove most of the background and achieve an average purity of 98%.

A weighted average was chosen for the combination. Muon scale and resolution uncertainties were treated as fully correlated in the combination. The formula used for the combination was:

$$\alpha_{\text{combined}} = \frac{w_e \alpha_e + w_\mu \alpha_\mu}{w_e + w_\mu} \tag{4.14}$$

where $w_i = 1/\sigma_i^2$ is the weight associated to each scale α_i. The uncertainty on α_{combined} was propagated as:

$$\sigma_{\text{combined}} = \frac{1}{\sqrt{w_e + w_\mu}} \tag{4.15}$$

The unconverted photon energy scales from $Z \to \mu\mu(\gamma)$ (collinar and non-collinear) and from $Z \to ee(\gamma)$ (non-collinear) are shown together in figures 4.11 and 4.12 prior to combination. Their weighted average is shown in figures 4.13 and 4.14 in bins of η and E_T, respectively. The collinear analysis was performed with an Alpgen sample and with a SHERPA sample, and the results are shown on the left and right plots respectively, for comparison.

Good agreement is observed between the three different analyses in both η bins

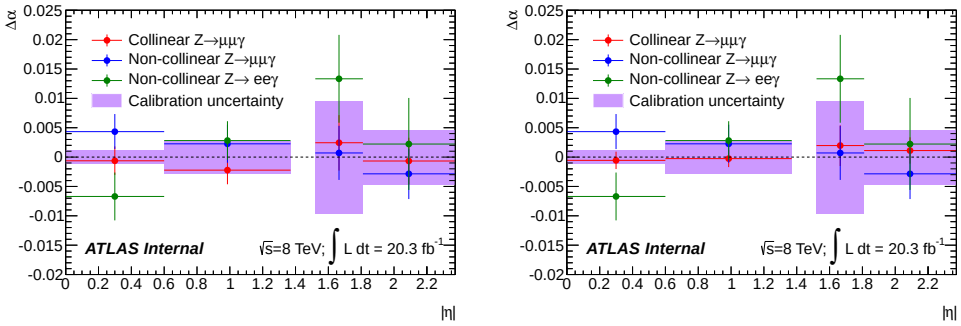

Figure 4.11: Photon energy scale factors for FSR photons from (black) $Z \to \mu\mu$ (collinear), (red) $Z \to \mu\mu$ (non-collinear) and $Z \to ee$ in bins of photon η. The violet band around zero represents the systematic uncertainty associated to the electron scale from $Z \to ee$ calculations. The vertical uncertainties on the points are statistical and systematic added in quadrature. Collinear results are shown with Alpgen (left) and Sherpa (right). The barrel−end-cap crack region $|\eta| \in (1.37, 1.52)$ is excluded.

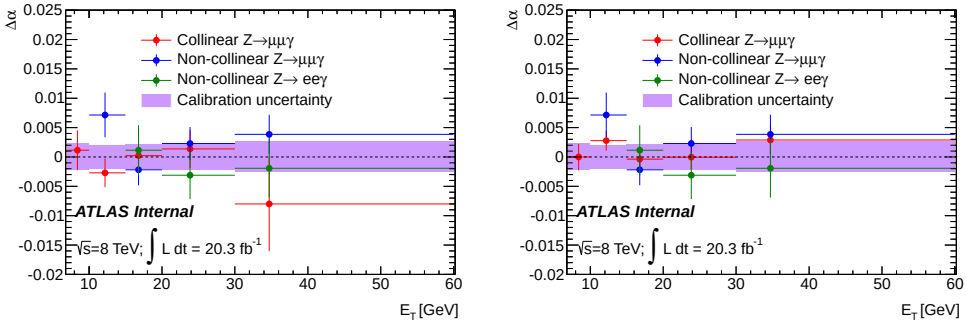

Figure 4.12: Photon energy scale factors for FSR photons from (black) $Z \to \mu\mu$ (collinear), (red) $Z \to \mu\mu$ (non-collinear) and $Z \to ee$ in bins of photon E_T. The violet band around zero represents the systematic uncertainty associated to the electron scale from $Z \to ee$ calculations. The vertical uncertainties on the points are statistical and systematic added in quadrature. Collinear results are shown with Alpgen (left) and Sherpa (right).

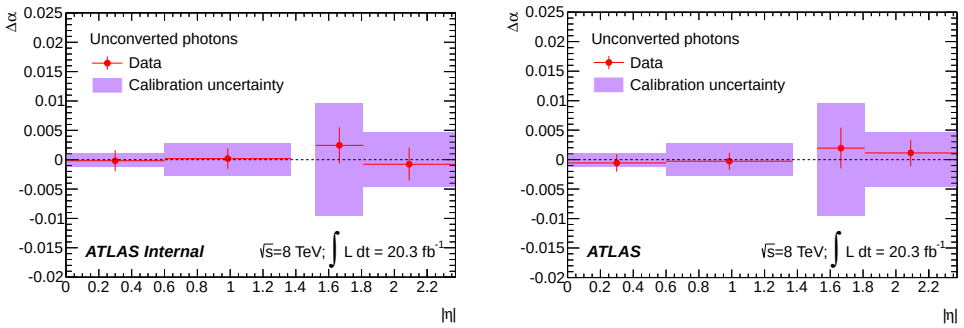

Figure 4.13: Combination of scale factors from all unconverted FSR photons in bins of photon η (red circles). The violet band around zero represents the systematic uncertainty associated to the electron scale from $Z \to ee$ calculations. The vertical uncertainties on the points are statistical and systematic added in quadrature. Collinear results are shown with Alpgen (left) and Sherpa (right). The barrel−end-cap crack region $|\eta| \in (1.37, 1.52)$ is excluded.

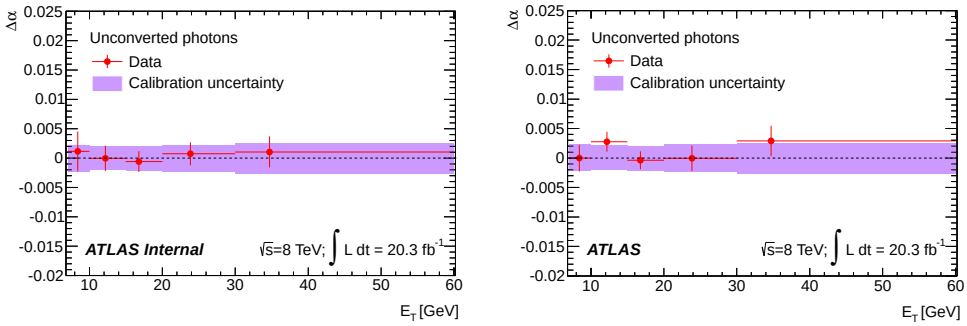

Figure 4.14: Combination of scale factors from all unconverted FSR photons in bins of photon E_T (red circles). The violet band around zero represents the systematic uncertainty associated to the electron scale from $Z \to ee$ calculations. The vertical uncertainties on the points are statistical and systematic added in quadrature. Collinear results are shown with Alpgen (left) and Sherpa (right).

(Figure 4.11) and E_T bins (Figure 4.12). The combination of the results is fully compatible with the electron scales from section 4.1, showing a good uniformity (Figure 4.13) and linearity (Figure 4.14).

4.3 $H \rightarrow \gamma\gamma$ mass measurement

The cross-check of the extrapolation of the $Z \rightarrow e^+e^-$ based energy scale calibration to photons was indispensable for the validation of the method. In the absence of a significant bias, the Higgs mass was measured in the $H \rightarrow \gamma\gamma$ decay channel. The effect of the systematic uncertainties arising from the photon energy calibration ranges from 0.18% to 0.31% depending on the kinematic category of the diphoton, as described in [32]. The fit result, shown in figure 4.15, yields a value for the Higs mass from the $H \rightarrow \gamma\gamma$ decay channel of $m_H = 125.98 \pm 0.50$ GeV.

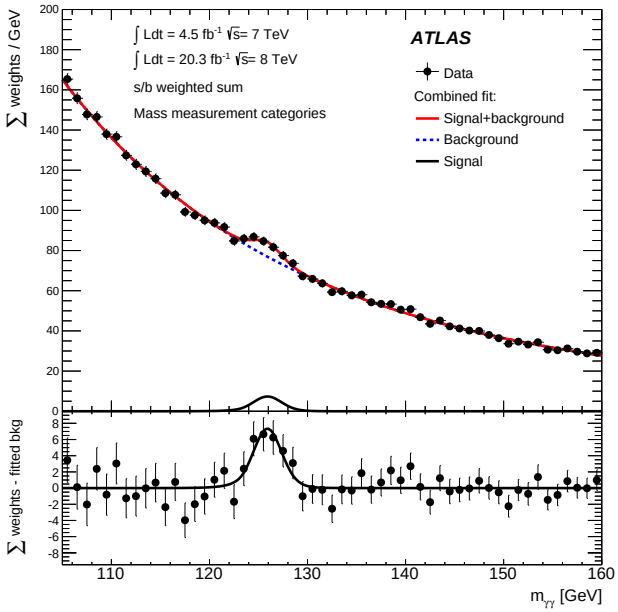

Figure 4.15: Invariant mass distribution in the $H \rightarrow \gamma\gamma$ analysis for data (7 TeV and 8 TeV samples combined), showing weighted data points with errors, and the result of the simultaneous fit to all categories. The fitted signal plus background is shown, along with the background-only component of this fit. The different categories are summed together with a weight given by the s/b ratio in each category. The bottom plot shows the difference between the summed weights and the background component of the fit. From [32]

Chapter 5

Search for Higgs boson decays to a photon and a Z boson in pp collisions at $\sqrt{s} = 7$ and 8 TeV with the ATLAS detector

5.1 Introduction

In July 2012, the ATLAS [35] and CMS [36] experiments discovered a new particle decaying to pairs of bosons ($\gamma\gamma$, ZZ, WW) in the search for the Higgs boson. It was unknown if the particle was the expected Standard Model Higgs, a different, exotic neutral Higgs particle or simply a different particle with similar couplings. The small excess observed in the $\gamma\gamma$ decay channel signal yield with respect to SM expectation in both ATLAS ($\mu_{\gamma\gamma}^{\text{ATLAS}} = (1.9 \pm 0.5) \times \text{SM}$) and CMS ($\mu_{\gamma\gamma}^{\text{CMS}} = (1.6 \pm 0.4) \times \text{SM}$) suggested the possibility of new colourless charged particles with significant coupling to the Higgs, an extended Higgs sector or the observation of a Higgs impostor in the form of an electroweak singlet scalar.

The branching ratio of $H \to \gamma\gamma$ is intimately related to the branching ratio of $H \to Z\gamma$. The modification of the former should have an effect on the latter. In the SM, both decays occur via loops of the same charged particles, with the most sizeable contribution coming from the $W^{\pm}$ loop (see figure 5.1a), followed by the top-quark

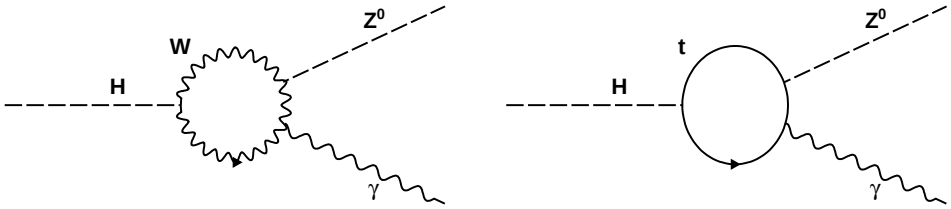

(a) (b)

Figure 5.1: SM contributions to the $H \rightarrow Z\gamma$ decay branching ratio.

loop (see figure 5.1b), giving rise to the branching ratios shown in figure 5.2. If new, unknown charged vector bosons were mediating the Higgs decay to $\gamma\gamma$ and $Z\gamma$, their shifts in branching fraction would be of similar magnitude, while for new fermions or scalar particles the $H \rightarrow Z\gamma$ shift would be smaller [37]. These new particles would induce differences in electroweak observables and new minima in the Higgs potential, either at tree level or after the inclusion of radiative corrections, and they would represent evidence of particles at the TeV scale.

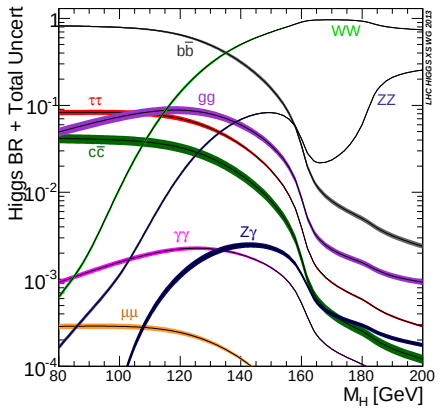

Figure 5.2: Higgs branching ratios and their uncertainties [38].

However, the discovery of a resonant signal in the diboson channels does not directly imply the discovery of the SM Higgs boson. Clearly different rates or subtle differences in channel correlations may arise from impostor or look-alike particles. Singlet electroweak scalars have an enhanced decay branching fraction into $\gamma\gamma$ and $Z\gamma$ with respect to the SM Higgs, while their decay into ZZ or W^+W^- is disfavoured, and

could have induced the discovered signal [39, 40]. Modifications of the rates are also expected if the Higgs is a composite particle [41].

Posterior analyses determined the properties of the observed resonance. Its couplings to bosons [13, 14] and its spin and parity [15, 16] are consistent with a SM Higgs boson of mass $m_H \sim 125.5$ GeV [13]. The coupling to fermions still remains to be determined, but there is evidence in favour of the SM hypothesis [42]. The measured decay rates, particularly $H \to \gamma\gamma$, constrain the enhancement of the $Z\gamma$ decay channel to a maximum of about $2\times$SM expectation given the above-described models, but larger enhancements can be realised via careful selection of parameters.

5.2 Data and Monte Carlo samples

Data events are required to pass the lowest energy unprescaled lepton or dilepton triggers. The single-muon trigger has a threshold of $p_T > 24$ GeV for the $\sqrt{s} = 8$ TeV period and 18 GeV for the 7 TeV period. The single-electron trigger has E_T thresholds of 25 and 20 GeV, respectively. Dimuon events are triggered when both muons pass $p_T > 13$ GeV or $p_T > 10$ GeV, respectively for each period, and dielectron events are triggered if $E_T > 12$ GeV for both electrons. An asymmetric trigger is also used for dimuon events in $\sqrt{s} = 8$ TeV, requiring $p_{T1} > 18$ GeV and $p_{T2} > 8$ GeV. The efficiency of the triggers is 99% and 92% for $e^+e^-\gamma$ and $\mu^+\mu^-\gamma$ events pasing all the analysis cuts, respectively. The muon channel has a reduced geometric acceptance for the regions $|\eta| < 1.05$ and $|\eta| > 2.4$. After trigger efficiency and data quality requisites the integrated luminosities are 20.3 fb^{-1} and 4.5 fb^{-1} for the 8 and 7 TeV data-taking periods.

Standard Model signal and background events are simulated using the Monte Carlo event generators outlined in table 5.1.

Signal ggF and VBF processes, amounting to 95% of SM production cross section, are generated with POWHEG and then interfaced to PYTHIA 8.170 for showering and hadronisation using CT10 PDFs [51]. The Higgs p_T distribution predicted by HRES2 [52] is used to reweight the ggF events. Associated production signal (WH, ZH and $t\bar{t}H$) is simulated with PYTHIA 8.170 with CTEQ6L1 PDFs [53]. Signal events are produced for $m_H \in (120, 150)$ GeV in steps of 5 GeV for both centre-of-mass energy conditions. Events are weighted to agree with their SM cross section for

Table 5.1: Event generators used to model the signal (first two rows) and background (last four rows) processes.

Process	Generator
ggF, VBF	POWHEG [43, 44, 45]+PYTHIA8 [24]
WH, ZH, $t\bar{t}H$	PYTHIA8
$Z+\gamma$ and $Z \to \ell\ell\gamma$	SHERPA [46, 47]
Z+jets	SHERPA, ALPGEN [23]+HERWIG [48]
$t\bar{t}$	MC@NLO [49, 50]+HERWIG
WZ	SHERPA, POWHEG+PYTHIA8

each generated mass.

Computations are performed at NNLO in the strong coupling constant α_s and NLO in the electroweak coupling constant α except for $t\bar{t}H$ associated production, calculated at NLO in α_s. Theoretical uncertainties affecting the production cross section are due to the choice of renormalisation and factorisation scales in the calculations, the uncertainty on PDFs and the value chosen for α_s in the perturbative expansion. Dependence on centre-of-mass energy and generated Higgs mass ($m_H \in (120, 150)$ GeV) is small. Uncertainties on scale for all considered Higgs production processes are uncorrelated. At $\sqrt{s} = 8$ TeV and $m_H = 125.5$ GeV their value is $^{+7}_{-8}$% for ggF , ±0.2% for VBF, ±1% for WH, ±3% for ZH and $^{+4}_{-9}$% for $t\bar{t}H$. PDF and α_s systematics are correlated in the gluon-initiated ggF and $t\bar{t}H$ processes, and the quark-initiated VBF and WH and ZH processes. At $\sqrt{s} = 8$ TeV and $m_H = 125.5$ GeV the uncertainties are ±8% and ±2.5% respectively. Higgs boson branching ratios are calculated with HDECAY and Prophecy4f [54, 55, 56]. The relative uncertainty associated to the $H \to Z\gamma$ decay channel is m_H dependent and ranges from ±9% to ±6% for $m_H = 120$ and 150 GeV respectively. A further ±5% uncertainty is added to account for internal photon conversions in $H \to \gamma^*\gamma \to \ell^+\ell^-\gamma$ decays and for radiative $H \to \mu^*\mu \to \mu^+\mu^-\gamma$ decays in the accepted Z-mass range.

Background samples are simulated to test background parameterisation and study the fit bias (see section 5.4). ALPGEN and MC@NLO samples are interfaced to HERWIG 6.510 for parton showering, fragmentation and underlying event modelling, with JIMMY 4.31 [57] to simulate multiparton interactions. SHERPA, MC@NLO and POWHEG are run with CT10 PDFs, and with ALPGEN CTEQ6L1 PDFs were used.

Geant4 is used to simulate the interaction of all Monte Carlo generated samples with the ATLAS detector, including pileup interactions from nearby bunch crossings. The Monte Carlo simulated events are weighted according to their average number of interactions per bunch crossing $\langle\mu\rangle$ to match the measured distribution observed in data in the different data-taking periods as well as the luminous region observed in data.

5.3 Event selection and backgrounds

5.3.1 Event selection

The selection requires a minimum of one primary vertex per event, determined from ID track fits compatible with a common point of origin. The vertex with the highest scalar sum of track p_T is then chosen.

Two opposite-sign same-flavour leptons are selected. In the case of muons, $p_T > 10$ GeV and $|\eta| < 2.7$ is required for each candidate. Muons reconstructed in the central barrel region, where the MS does not provide coverage ($|\eta| < 0.1$), must satisfy $p_T > 15$ GeV. Good muon track reconstruction is ensured with the requirement of a minimum number of associated ID hits, and transverse and longitudinal impact parameters must satisfy $d_0 < 1$ mm and $z_0 < 10$ mm, respectively, with respect to the primary vertex.

In the case of electrons, the candidates' transverse energy must be $E_T > 10$ GeV and their pseudorapidity within $|\eta| < 2.47$. Electron and photon energy is reconstructed from energy deposits in the EM calorimeter. Tracks belonging to an electron or originating from a photon conversion (only in $\sqrt{s} = 8$ TeV data) are required a minimum number of associated silicon detector hits. They are fitted with a Gaussian-Sum Filter [58] to account for energy loss in the form of bremsstrahlung. The tracks are required to point to the energy clusters, have at least one associated hit in the innermost ID pixel layer if traversing an active module and have a longitudinal impact parameter $z_0 < 10$ mm. Electron energy clusters are required to be consistent with expected electromagnetic transverse and longitudinal shower shapes[59].

Photon candidates must satisfy $E_T > 15$ GeV and be reconstructed in the pseudorapidity region with high EM calorimeter Layer 1 granularity $|\eta| \in [0, 1.37] \cup [1.52, 2.37]$. Good status of read-out and high-voltage systems is required, and clusters recon-

structed near affected regions are discarded.

Photons are required to satisfy a selection based on the first and second calorimeter layer shower shapes, as well as on the energy leakage into the hadronic calorimeter [19]. Hadronic background is additionally reduced through the calorimeter isolation transverse energy [35] E_T^{iso} calculated as the sum of E_T depositions in a cone of radius $\Delta R = \sqrt{(\Delta\eta)^2 + (\Delta\phi)^2} = 0.4$ centred in the photon candidate and subtracting contributions from pileup, the underlying event and the photon cluster energy. $E_T^{\text{iso}} < 4$ GeV is required.

In some cases, muons and electrons are reconstructed with the same track. Overlap removal is performed. Muons reconstructed in the MS have precedence over electrons. Otherwise the muon candidates are discarded. Photon candidates are rejected if their energy cluster is found within $\Delta R < 0.3$ of a muon or electron candidate to suppress radiative Z and H decays to $\ell\ell(\gamma)$ final states.

Same-flavour and opposite-sign lepton pairs are selected as Z boson candidates if both particles pass the above-mentioned requirements. At least one of the $Z \to \mu\mu$ candidate muons is required to be reconstructed simultaneously in the ID and the MS detectors for the pair to be considered. If more than one Z candidate is found, the lepton pair with invariant mass closest to the Z pole mass is chosen.

Higgs boson candidates are built from a Z and a γ candidate. The photon with the highest E_T of the event is chosen. The leptons that triggered the event are required to match the leptons from the $Z \to \ell\ell$ pair (one or both for single or dilepton trigger, respectively). Track and calorimeter isolation are required for the $Z \to \ell\ell$ candidate leptons. The track p_T^{iso}, computed in a $\Delta R = 0.2$ cone around each lepton track, excluding it, must satisfy $p_T^{\text{iso}}/p_T^{\ell} < 0.15$. Similarly, electron $E_T^{\text{iso}}/E_T^{\ell} < 0.2$ is required, with the electron isolation variable calculated in a cone of radius $\Delta R = 0.2$. For muons, the selection requires $E_T^{\text{iso}}/p_T^{\mu} < 0.3$, or 0.15 if no ID track was reconstructed, with the same isolation cone around the muon track. The contributions to the isolation cones from any of the Z lepton candidates are subtracted.

Further impact parameter requirements are imposed. The transverse impact parameter significance of the lepton ID track must satisfy $|d_o|/\sigma_{d_0} < 3.5$ for muons and 6.5 for electrons.

Cuts are applied on the invariant mass of the dilepton and the $\ell\ell\gamma$ systems to suppress contributions from $H \to \gamma^*\gamma \to \ell\ell\gamma$ and $H \to \ell^*\ell \to \ell\ell\gamma$ that mimic the

$H \to Z\gamma \to \ell\ell\gamma$ final state. $m_{\ell\ell} > m_Z - 10$ GeV and $115 < m_{\ell\ell\gamma}/\text{GeV} < 170$ is required.

The number of events passing all the selections described above from the $\sqrt{s}$ = 7 TeV and 8 TeV runs in the $Z \to ee$ and $Z \to \mu\mu$ channels is shown in table 5.2.

Table 5.2: Events passing all selection cuts in the $H \to Z\gamma$ analysis.

# events	$Z \to ee$ channel	$Z \to \mu\mu$ channel
$\sqrt{7}$ TeV	1041	1400
$\sqrt{8}$ TeV	7798	9530

Monte Carlo simulated events are reconstructed and selected as data events, and then corrected for efficiency and energy and momentum resolution differences with data observed in photons and leptons.

Signal $H \to Z\gamma \to \ell\ell\gamma$ acceptance of the kinematic requirements for simulated events at $m_H = 125.5$ GeV is 54% in the $Z \to ee$ channel and 57% in the $Z \to \mu\mu$ channel. Photon reconstruction and selection has an average efficiency of 61% for $\sqrt{s}$ = 7 TeV data and 68% for 8 TeV data. The $Z \to ee$ efficiencies are 67% and 74%, respectively. The increment in efficiency in the second data-taking period is due to a re-optimisation of the photon and electron identification criteria. In the case of $Z \to \mu\mu$ the reconstruction and selection efficiency is 88%.

If trigger efficiencies are taken into account, the full signal efficiency for $H \to Z\gamma \to \ell\ell\gamma$ events at $m_H = 125.5$ becomes 22% for the electron channel and 27% for the muon channel, at $\sqrt{s}$ = 7 TeV, and 27% and 33% at 8 TeV, respectively.

Relative to simulated ggF signal events, the VBF channel has a 5% higher efficiency, while the associated production modes are below by 5 to 10%. As a function of m_H, the overall signal efficiency varies from 120 to 150 GeV within 0.87 and 1.25 relative to the efficiency at 125.5 GeV.

5.3.2 Invariant mass calculation

Three corrections are implemented to the three-body invariant mass $m_{\ell\ell\gamma}$ with the aim of better discriminating background events that do not belong to the resonant Higgs signal distribution.

Photon pseudorapidity correction

The standard ATLAS photon reconstruction algorithm calculates the photon transverse energy and pseudorapidity with respect to the nominal interaction point of the detector ($\vec{r} = \vec{0}$). The selected photon pseudorapidity η_γ is recalculated with respect to the primary vertex and its transverse energy corrected $E_T^\gamma = E_\gamma / \cosh \eta_\gamma$. The improvement observed in the signal mass resolution is $\sim$ 1% [28].

Collinear FSR correction

$Z \rightarrow \mu\mu$ channel events are corrected for FSR photons collinear to muons, as described in section 3.1.2. The resolution of the three-body system is improved by $\sim$ 1% due to the Z mass resolution improvement after the correction, included in figure 5.4 (left). No *far* FSR correction is applied.

A study performed on ALPGEN Monte Carlo-generated events determined that the FSR correction is improving the dilepton reconstructed mass, as shown in figure 5.3. The figure shows the relative difference between the generated mass of the $Z \rightarrow \mu\mu\gamma$ three-body system and the reconstructed mass, calculated as $\frac{m_{\text{rec}} - m_{\text{true}}}{m_{\text{true}}}$, before and after the addition of the missing photon. The distribution of corrected events has a resolution of $\sim$ 1.9% and the average is shifted by 0.1% with respect to the true average.

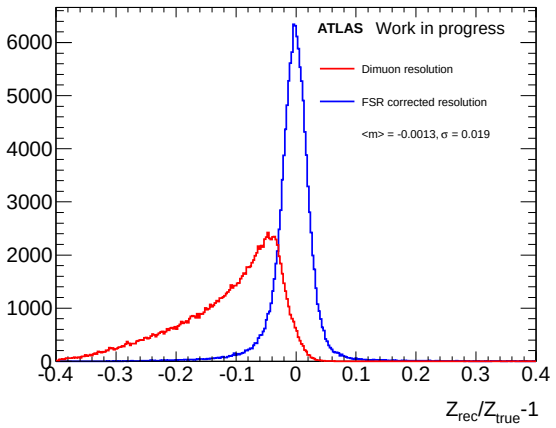

Figure 5.3: Relative difference between reconstructed and true mass ($\frac{m_{\text{rec}} - m_{\text{true}}}{m_{\text{true}}}$) in $Z \rightarrow \mu\mu$ Monte Carlo-simulated events with a collinear FSR photon identified before (red histogram) and after (blue histogram) FSR correction.

Z-mass constraint

The Z-mass resolution is further improved with the recalculation of the leading lepton four-momentum Lorentz vector in each event based on the known on-shell Z-mass lineshape. A Z-mass constrained fit is performed as previously used in the ATLAS $H \to 4\ell$ analysis [35]. The lepton four-momenta are recomputed by means of a kinematic fit which minimizes the χ^2 between the measured cartesian coordinates of the momenta and the best-fit values constraining the dilepton invariant mass to be equal to its most probable value, determined under the hypothesis of a true $Z \to \ell\ell$ decay and assuming an unbiased Gaussian resolution function for the detector reconstruction of the mass. An improvement of $\sim 15 - 20\%$ after all other corrections is observed in the mass resolution.

The effect of the corrections is shown in figure 5.4. The $m_{\mu\mu\gamma}$ and $m_{ee\gamma}$ distributions represented correspond to $gg \to H$ Monte Carlo simulated signal events at $m_H = 125$ GeV. The $m_{ee\gamma}$ resolution is affected by bremsstrahlung, and is $\sim 8\%$ worse than for $m_{\mu\mu\gamma}$. The three-body mass distribution is modelled with a Crystal Ball function accounting for the well-reconstructed events plus a wide Gaussian component to represent the tails of the distribution. At $m_H = 125.5$ GeV, the resolution of the core distribution in the $\mu\mu$ channel is $\sigma_{CB} = 1.6$ GeV.

5.3.3 Event categorisation

The $\ell\ell\gamma$ events are first categorised based on the centre-of-mass energy of the pp collisions ($\sqrt{s} = 7$ or 8 TeV) and the lepton flavour ($\ell = e, \mu$). Further categorisation classifies events into groups according to their signal-to-background ratio and invariant mass resolution. The classification is based on two variables:

- $\Delta\eta_{Z,\gamma} = |\eta_Z - \eta_\gamma|$
  The pseudorapidity difference between the Z and the γ of the Higgs candidate.

- $p_{Tt} = |(\vec{p}_T^{\,\gamma} + \vec{p}_T^{\,Z}) \times \hat{t}|$
  The p_{Tt} of the event, defined as the component of the vectorial Higgs boson

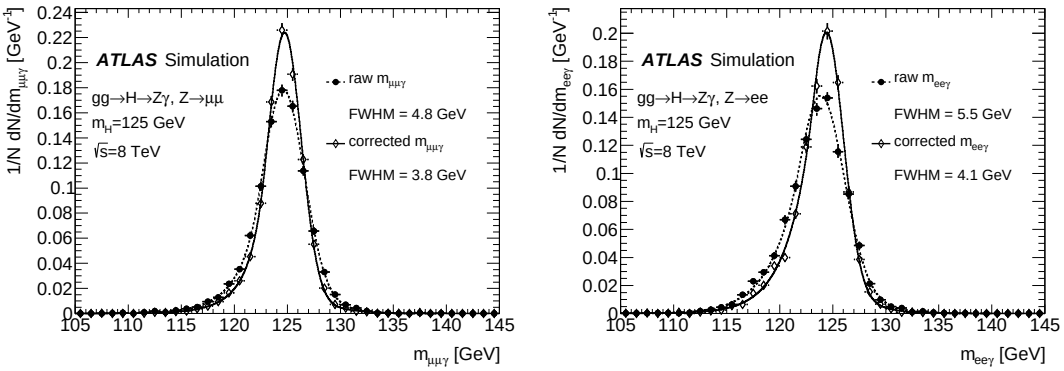

Figure 5.4: Three-body invariant-mass distribution for $H \to Z\gamma$, $Z \to \mu\mu$ (left) or $Z \to ee$ (right) selected events in the 8 TeV, $m_H = 125$ GeV gluon-fusion signal simulation, after applying all analysis cuts, before (filled circles) and after (open diamonds) the corrections described in Section 5.3.2. The solid and dashed lines represent the fits of the points to the sum of a Crystal Ball and a Gaussian function.

candidate transverse momentum $\vec{p}_T$ in the direction of the $Z\gamma$ thrust axis $\hat{t}$ in the transverse plane. The thrust axis direction is defined as $\hat{t} = (\vec{p}_T^{\,\gamma} + \vec{p}_T^{\,Z})/|\vec{p}_T^{\,\gamma} + \vec{p}_T^{\,Z}|$.

Events are separated into high-p_{Tt} and low-p_{Tt} candidates if their p_{Tt} is greater or less than 30 GeV, respectively. In the 8 TeV analysis, enough statistics allowed for an additional classification of events into a $|\Delta\eta_{Z,\gamma}| < 2.0$ category and a $|\Delta\eta_{Z,\gamma}| > 2.0$ category.

Higher signal-to-background ratio is observed in events with high-p_{Tt} and small $|\Delta\eta_{Z,\gamma}|$, while background events, mostly coming from the $q\bar{q} \to Z + \gamma$ process, are characterised by a greater $|\Delta\eta_{Z,\gamma}|$ due to the Z and γ being back-to-back in the transverse plane. These high-p_{Tt}, low-$|\Delta\eta_{Z,\gamma}|$ event categories are mostly populated by VBF or associated production (VH, $t\bar{t}H$) signal events, in which the Higgs is more boosted, as well as ggF events with harder or more central photon and leptons, resulting in a higher mass resolution.

This categorisation improves the sensitivity of the analysis by 33% for a signal at $m_H = 125.5$ GeV with respect to a categorisation based on the centre-of-mass energy and the lepton flavour alone [60].

5.3.4 Sample composition

The most important backgrounds affecting this channel are the continuum $Z+\gamma$, $Z \to \ell\ell$ production, radiative $Z \to \ell\ell\gamma$ decays and $Z+$ jets ($Z \to \ell\ell$ decays with a jet misidentified as a photon). Other smaller background components are $t\bar{t}$ and WZ events.

The $Z + \gamma$ component is produced in $q\bar{q}$ interactions via the t or u-channel and in parton-to-photon fragmentation. The photon isolation requirement is designed to remove the events arising from parton fragmentation, and $Z + jets$ events together with photon identification criteria. Non-collinear FSR photons from radiative $Z \to \ell\ell\gamma$ decays are suppressed with a selection designed to be opposite to that in section 3.1.2: $m_{\ell\ell} > m_Z - 10$ GeV, $m_{\ell\ell\gamma} > 115$ GeV and $\Delta R(\ell, \gamma) > 0.3$.

Simulated samples are only used to optimise the selection applied to data events and the fitting functions to estimate the background in data, and to determine the associated systematic uncertainties. Therefore the background composition is only estimated to correctly normalise the different simulated samples.

The two $Z + \gamma$, $Z \to \ell\ell$ and $Z \to \ell\ell\gamma$ components interfere and are not independently Lorentz invariant. They must be considered as a single $Z\gamma$ background.

The $t\bar{t}$ and WZ background contributions are estimated directly from simulation, normalising to the measured luminosity with the Monte Carlo NLO cross sections. An uncertainty of ±50% is conservatively considered to account for data-Monte Carlo differences in the rate of jet misidentification, the PDF uncertainties and the trunked perturbative expansion [28]. The relative fractions of $Z\gamma$ and $Z+jets$ background events are estimated from data after the subtraction of the Monte Carlo-estimated $t\bar{t}$ and WZ components. A 2D sideband method [19, 61] is applied utilising photon isolation and identification variable distributions in Z+jets enriched control regions.

The presence of a background $Z\gamma$ component in $Z+jets$ control regions is estimated from simulated events, as well as the correlation between photon identification and isolation variables in $Z + jets$ events. The signal $H \to Z\gamma$ is neglected during this estimation. For $\sqrt{s} = 7$ and 8 TeV, the background is composed of 82% $Z\gamma$, 17% $Z+jets$ and 1% $t\bar{t}+WZ$ events. The contamination of $Z\gamma$ by mainly $Z+jets$ events has a relative uncertainty of 5%, estimated comparing ALPGEN and SHERPA predictions of the correlation of photon identification and isolation variables in $Z + jets$ events. Data and Monte Carlo show good agreement in $m_{\ell\ell\gamma}$, $m_{\ell\ell}$, lepton and photon p_T, η and

ϕ, and other kinematic variables.

5.4 Experimental systematic uncertainties

The impact of experimental systematic uncertainties on the expectation value of signal yields in the different categories was quantified as follows:

- 1.8% and 2.8% uncertainty on integrated luminosity for 7 TeV and 8 TeV data, respectively [62].
- Photon identification efficiency uncertainty has a category-dependent value ranging from 2.6% to 3.1%. Photon ID efficiency is neglected. Data and Monte Carlo comparisons were performed on electron and photon control samples to estimate these effects [21].
- The combination of electron trigger, reconstruction and identification efficiency uncertainties ranges from 2.5% to 3% in $Z \to e^+e^-$ categories. Large control samples of $Z \to \ell\ell$, $W \to \nu e$ and $J/\psi \to \ell\ell$ are used for the determination of the different lepton efficiencies. The effect of the data-driven measurement uncertainties is estimated by varying the efficiency corrections applied to Monte Carlo samples within those uncertainties [63, 64].

Lepton energy scale, resolution and impact parameter selection efficiencies, muon trigger, reconstruction and identification efficiencies and photon and lepton isolation efficiencies have a negligible effect on signal yield, and amount to 5% relative uncertainty per category on signal efficiency, less than half the SM $\sigma \times BR$ theoretical uncertainty. The estimated uncertainty affecting the population of p_{Tt} categories coming from the simulated Higgs p_T varies within 1.8% and 3.6%, depending on category. It is determined varying the QCD scales and PDFs used in HRES2 to predict the p_T spectrum.

The experimental systematic uncertainties considered that affect the $m_{\ell\ell\gamma}$ signal distribution are:

- Peak position uncertainty of 0.2 GeV. The major contribution comes from the $Z \to ee$ energy scale calibration of electrons and the extrapolation to photons, as described in chapter 3.

- 3% and 10% uncertainty on photon energy resolution in $Z \to \mu\mu$ and $Z \to ee$ events, respectively. To estimate these values, the resolution corrections applied to the Monte Carlo simulation were varied within their systematic uncertainties.

- Muon momentum is smeared in the Monte Carlo simulation to match the measured momentum resolution. The smearing is varied within uncertainties to extract a value $\lesssim 1.5\%$ of resolution uncertainty.

Bias in the signal extraction procedure is also considered. The background is fitted with analytical functions optimised to maximise the sensitivity in each category with a bias limited to a maximum of 20% in the signal yield statistical uncertainty from background fluctuations. The fit is performed in a range optimised for all categories simultaneously. The different models are optimised with large simulated signal and background samples. The greatest bias observed in each category is used as a systematic uncertainty. In the $m_{\ell\ell\gamma} \in (120, 150)$ GeV range, the bias varies from 0.5 to 8.3 events depending on the population.

The uncertainties in 2011 and 2012 are taken as 100% correlated, except in the luminosities.

5.5 Results

5.5.1 Likelihood function

The $m_{\ell\ell\gamma}$ distribution is simultaneously fitted in all categories in the mass range $m_{\ell\ell\gamma} \in (115, 170)$ GeV. The likelihood is a function of the parameter of interest $\langle\mu\rangle$, the Higgs signal yield divided by the expected Standard Model yield, known as the signal strength; and of nuisance parameters describing the background shape and normalisation per category, and the systematic uncertainties.

The signal production cross sections times branching ratio for $\sqrt{s} = 7$ and 8 TeV are extracted from a simultaneous fit with these two parameters of interest, but removing the systematic uncertainties on the expected SM values from the fit.

The model chosen to fit the background in each category is optimised to maximise sensitivity and minimise bias, as described in section 5.4. Fourth and fifth-order polynomials are used to fit the low P_{Tt} categories and an exponentiated second-order

polynomial for the high P_{Tt} cases in $\sqrt{s} = 8$ TeV data. For $\sqrt{7}$ TeV data, a fourth-order polynomial and an exponential function are used, respectively, for the low and high P_{Tt} categories.

Simulated samples are used to determine the signal resolution with the model described in section 5.3.2. The parameters are extracted for each Higgs mass in the range $m_H \in (120, 150)$ GeV in 0.5 GeV steps separately for each category, interpolating the fully simulated Monte Carlo samples.

A constraint factor is included in the likelihood function for each nuisance parameter representing one of the systematic uncertainties described in section 5.4. A log-normal constraint is used for expected signal yield uncertainties in each $\sqrt{s}$ and lepton flavour category, and a Gaussian constraint is used for the signal fraction uncertainty in the kinematic categories as well as for the $m_{\ell\ell\gamma}$ signal resolution [65].

5.5.2 Statistical analysis

A profile likelihood test statistic [65] is used to compare the background-only hypothesis and the signal-plus-background hypothesis. Likelihood maximisation is performed to determine the best μ value ($\hat{\mu}$) for each Higgs mass in the range $m_H \in (120, 150)$ GeV in steps of 0.5 GeV. The likelihood is also maximised for different fixed values of μ to extract the optimal value of nuisance parameters (e.g. background only $\mu = 0$, SM signal plus background $\mu = 1$). The compatibility of the different hypotheses with the data is quantified with the p-value. The p-value of the background-only hypothesis, p_0 is used as an estimate of the significance of an observation. Signal strength μ upper limits are calculated at 95% CL with a modified frequentist (CL_s) method [66], calculating $\mu_{\text{up}} = \mu(CL_s = 0.05)$. The observed results from the data fit are compared to generated Asimov pseudo-data [67]. The pseudo-data is generated for the $\mu = 0$ and $\mu = 1$ hypotheses to respectively extract CL_s and p_0 upper limits.

The $m_{\ell\ell\gamma}$ distribution of all data events is shown in figure 5.5 (black circles), compared to the sum of all background-only fits of each category to data (blue line). No significant excess is found for any of the masses with respect to the background fits, and the p_0 shows compatibility with the null hypothesis. The greatest excess is found at $m_H = 141$ GeV, with $p_0 = 0.05$, equivalent to a significance of $\sigma = 1.6$. The expected value of p_0 is in the range (0.34, 0.44) for the chosen mass range. At $m_H = 125.5$ GeV

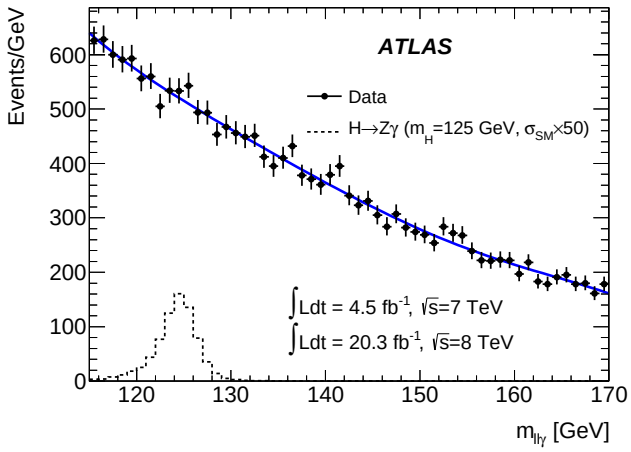

Figure 5.5: Distribution of the reconstructed $\ell\ell\gamma$ invariant mass in data, after combining all the event categories (points with error bars). The solid blue line shows the sum of background-only fits to the data performed in each category. The dashed histogram corresponds to the signal expectation for a Higgs boson mass of 125 GeV decaying to $Z\gamma$ at 50 times the SM-predicted rate.

$p_0 = 0.42$ is expected (0.2σ) and $p_0 = 0.27$ is observed (0.6σ). Shown in figure 5.6, 95% CL expected and observed signal strength μ upper limits are found to be respectively between 5 and 15, and 3.5 and 18 in the range of masses between 120 and 150 GeV. At $m_H = 125.5$ GeV the expected limit is 9 while the observed limit is 11, and assuming SM Higgs boson signal $\mu = 1$ the expected upper limit becomes 10. The FSR correction introduced a 2% improvement in the result.

The dominant contribution to the uncertainties in the results is statistical. If all systematic uncertainties are neglected, observed and expected 95% limits decrease by $\sim 5\%$.

Cross-section times branching ratio ($\sigma \times BR$) upper limits on the $pp \to H \to Z\gamma$ process are calculated as well at 95% CL. At $\sqrt{s} = 8$ TeV, the limit lies within 0.13 and 0.5 pb (0.33 – 0.45 pb at $m_H = 125.5$ GeV), and at $\sqrt{s} = 7$ TeV it is within 0.20 and 0.8 pb (0.7 – 0.55 pb at $m_H = 125.5$ GeV).

At $m_H = 125.5$ GeV, expected and observed limits are 0.33 and 0.45 pb at $\sqrt{s} = 8$ TeV and 0.7 and 0.5 pb at $\sqrt{s} = 7$ TeV, respectively.

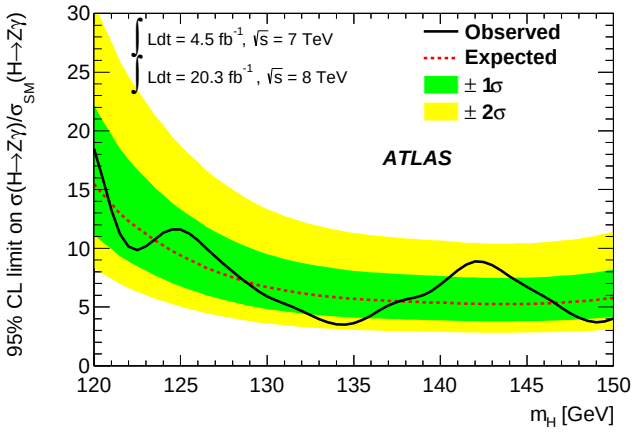

Figure 5.6: Observed 95% CL limits (solid black line) on the production cross section of a SM Higgs boson decaying to $Z\gamma$ divided by the SM expectation. The limits are computed as a function of the Higgs boson mass. The median expected 95% CL exclusion limits (dashed red line), in the case of no expected signal, are also shown. The green and yellow bands correspond to the $\pm 1\sigma$ and $\pm 2\sigma$ intervals.

5.6 Conclusions

The search for the Higgs boson in the $H \to Z\gamma$ in the range $m \in (120, 150)$ GeV with 4.5 fb^{-1} of pp collisions at $\sqrt{s} = 7$ TeV and 20.3 fb^{-1} at $\sqrt{s} = 8$ TeV recorded with the ATLAS detector did not find a significant excess of events with respect to the expected background. Several corrections to improve the invariant mass distribution are applied to the events, including the collinear FSR correction in the $Z \to \mu\mu$ channel that improves the resolution by $\sim 1\%$. The greatest excess is found at $m_H = 141$ GeV, with $p_0 = 0.05$, equivalent to a significance of $\sigma = 1.6$. A significant measurement would have been possible with $\gtrsim 220$ times the data. The upper limit of the cross section times branching ratio obtained at $\sqrt{s} = 8$ TeV ranges from 0.13 to 0.5 pb (95% CL), and the 7 and 8 TeV combined observed cross section divided by Standard Model expectation at $m_H = 125.5$ GeV is $11 \times$ SM at 95% CL.

Chapter 6

Introduction to radiation detectors

6.1 Radiation interaction with matter

Charged and uncharged particles with a kinetic energy above $\sim$ 20 eV are capable of inducing ionisation of atoms as they travel through matter. This so-called ionising radiation may undergo Coulomb interactions directly with orbital electrons and occasionally with atomic nuclei, or, in the case of uncharged particles, it may do so indirectly via the secondary products of a dramatic initial interaction, where it transfers most of its energy to the medium in an individual encounter.

6.1.1 Interaction of electrons with matter

Energetic electrons travelling through a medium suffer large deviations due to their electromagnetic interaction with orbital electrons. The incident electron may transfer a significant fraction of its energy to orbital electrons due to them having the same mass. Elastic scattering off atomic nuclei may also shift the electron direction dramatically.

Collisional energy loss (ionisation and excitation of atoms in the medium) is described by the following formula, derived by Bethe:

$$-\left(\frac{dE}{dx}\right)_c = \frac{2\pi e^4 NZ}{m_e v^2}\left(\ln\frac{m_e v^2 E}{2I^2(1-\beta^2)} - (\ln 2)\left(2\sqrt{1-\beta^2} - 1 + \beta^2\right) + (1-\beta^2) + \frac{1}{8}\left(1-\sqrt{1-\beta^2}\right)^2\right), \tag{6.1}$$

where e is the electron charge, N and Z are the number density and the atomic number of the atoms in the medium, respectively, v is the electron speed, E its energy, m_e its mass and $\beta = v/c$. The parameter I quantifies the ionisation and excitation potential of the atoms, and it is determined from experiment for each material. As the electron is

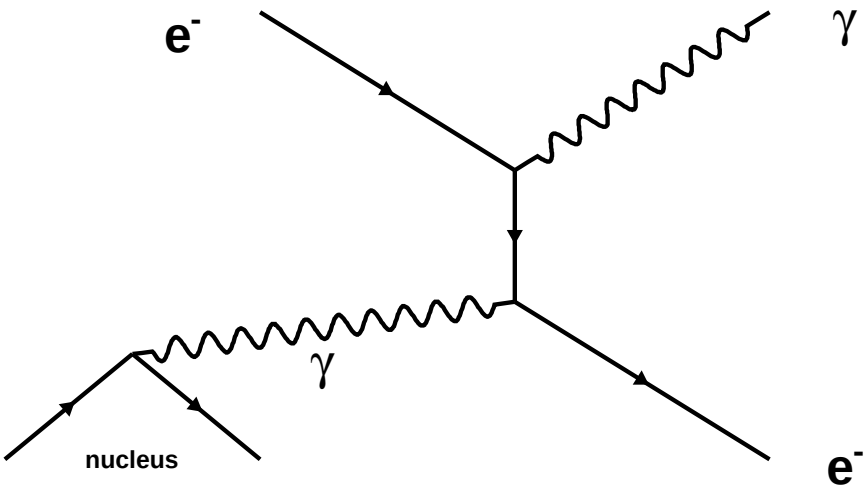

Figure 6.1: Diagram for bremsstrahlung. An electron interacts electromagnetically with the medium and emits radiation.

deflected in the absorber medium, it suffers certain acceleration. When charges are accelerated, they emit energy in the form of electromagnetic radiation, or bremsstrahlung. In figure 6.1 the diagram of one of the possible processes is shown. The other process is obtained by interchanging the vertices where the electron absorbs and emits radiation. The specific energy loss of an electron in a medium due to bremsstrahlung is given by:

$$-\left(\frac{dE}{dx}\right)_r = \frac{NEZ(Z+1)e^4}{137m_e^2c^4}\left(4\ln\frac{2E}{m_ec^2} - \frac{4}{3}\right). \tag{6.2}$$

As can be seen, the emission of radiation is more significant for high electron energies and in media with high atomic number. Heavy energetic nuclei do not suffer significantly from bremsstrahlung due to the mass parameter in the denominator.

The total specific energy loss of electrons in media is the sum of the collisional and radiative terms:

$$-\frac{dE}{dx} = -\left(\frac{dE}{dx}\right)_c - \left(\frac{dE}{dx}\right)_r \tag{6.3}$$

whose ratio is given by:

$$\frac{(dE/dx)_r}{(dE/dx)_c} \simeq \frac{EZ}{700\ \text{MeV}}. \tag{6.4}$$

For electrons with energy $E \sim$ MeV, the radiative contribution to the energy loss is only a small percentage, but it grows in importance for heavy materials and higher energies.

6.1.2 Interaction of γ-rays with matter

Photons are neutral particles that do not directly ionise or excite the medium around them. Instead, photons transfer the whole or part of their energy to electrons in the medium, which then gradually deposit their energy as they travel through the material.

The main three mechanisms of importance in spectroscopy through which a gamma-ray interacts in matter are:

Photoelectric absorption

A photon with energy $E = h\nu$ higher that the binding energy E_b of an electron in an atom may be absorbed by the electron and disappear. The extracted photoelectron acquires a kinetic energy $E_{e^-} = h\nu - E_b$, neglecting the small atom recoil energy. The vacancy left behind by the photoelectron is immediately occupied by an electron from a more loosely bound shell, releasing in turn an X-ray or an Auger electron carrying the difference in energy between the two states. The released X-ray may interact again and extract a more loosely bound electron. The process may continue and several low energy electrons can be extracted.

The process of photoelectric absorption then has the characteristic of a high energy electron, carrying most of the energy of the initial gamma-ray, plus low energy electrons from subsequent X-ray emissions, carrying the binding energy of the first photoelectron.

The kinetic energy carried by these electrons equals the incident gamma-ray energy $h\nu$. They excite and ionise the detector medium and thus the photon energy can be measured.

Compton scattering

This process consists on the partial transfer of energy and momentum from a photon to an electron, assumed unbound and at rest. The photon is deflected when the energy is transferred, and the electron suffers a recoil to conserve momentum.

If a photon of four-momentum[1] $\mathbb{P}_\gamma = (E, E, 0, 0)$, where $E = h\nu$ and momentum $p = E$ in the x-direction interacts with a static electron $\mathbb{P}_{e^-} = (m_e, 0, 0, 0)$, transferring a certain amount of energy, the resulting four-momenta will be $\mathbb{Q}_\gamma = (E', E'\cos\theta, E'\sin\theta, 0)$, where $E' = h\nu'$ and $\mathbb{Q}_{e^-} = (E_e, E_e\cos\phi, -E_e\sin\phi, 0)$.

Applying the conservation of total four-momentum the photon and recoil electron kinetic energies can be calculated as a function of the photon recoil angle:

$$h\nu' = \frac{h\nu}{1 + \frac{h\nu}{m_e}(1 - \cos\theta)} \tag{6.5}$$

$$K_e = h\nu - h\nu' = \frac{\frac{h\nu}{m_e}(1 - \cos\theta)}{1 + \frac{h\nu}{m_e}(1 - \cos\theta)}. \tag{6.6}$$

The maximum energy transfer takes place in head-on collisions ($\theta = \pi$)

$$K_e(\pi) = \left(\frac{2h\nu/m_e}{1 + \frac{2h\nu}{m_e}}\right) h\nu \tag{6.7}$$

So the energy distribution of the recoil electrons drops to zero abruptly at $K_e(\pi) < h\nu$, defining the so-called Compton edge. The separation between the initial gamma-ray energy and the Compton edge is given by $E_C = h\nu - K_e(\pi) = \frac{h\nu}{1+2h\nu/m_e}$, which tends to $E_C \to m_e/2$ in case $h\nu \gg m_e/2$.

Pair production

For gamma-rays with energies greater than $2m_e$, an additional interaction becomes energetically possible: e^-e^+ pair production. In the vicinity of the protons in the material of a detector, gamma-rays may convert into an e^-e^+ pair. The energy above the $2m_e$ threshold is converted into kinetic energy, shared by the produced pair, with a negligible amount transferred to a neighbouring nucleus to conserve overall momentum

[1] Speed of light in vacuum $c = 1$ is assumed here.

($\sim m_e^2/m_N$).

The electron and positron of the pair will subsequently excite and ionise the medium, and lose their energy. When this happens, the positron will annihilate with an electron from the medium and two back-to-back 0.511 MeV photons will be generated, possibly leading to energy depositions away from the original interaction point.

6.2 Noble liquid scintillation calorimeters

A calorimeter is a detector used to measure a particle's energy. In order to do this, calorimeters must be able to stop the particle, absorb their energy and collect it. Energetic particles deposit their energy via interactions with the medium, as described in section 6.1, so a high density target is required to maximise the stopping power of the detector. The products of the particle interaction are free electrons, ionised atoms and photons: charge and light that can be measured to estimate the particle energy. Calorimetry allows to measure the energy of neutral high-energy particles, such as γ-rays, neutrons, neutrinos...

Heavy noble liquids are amongst the most used media in calorimetry due to their density and scintillation yield. Noble gas scintillation is due to the decay of excited diatomic molecules, a feature also observed in the liquid phase [68]. Excited molecules are formed through the interaction of individual atoms (A) with energetic particles (R):

$$\begin{aligned} R + A &\rightarrow R' + e^- + A^+ \\ R + A &\rightarrow R' + A^* \\ e^- + A^+ &\rightarrow A^* \end{aligned} \tag{6.8}$$

Excited atoms may decay, releasing VUV photons[1]

$$A^* \rightarrow A + h\nu_a \tag{6.9}$$

or relax via heat emission to the surrounding medium. The photon from atomic decay is quickly reabsorbed by the medium, exciting a new atom.

[1] Vacuum Ultraviolet ($\lambda < 200$ nm) light, strongly absorbed in air.

	$\langle E_i \rangle$/eV	$\langle E_e \rangle$/eV	N_e/N_i	$\langle H \rangle/N_i$/eV
Ar	15.4	12.7	0.21	5.15
Kr	13.0	10.5	0.08	5.50
Xe	10.5	8.4	0.06	4.45

Table 6.1: Average energy required to ionise (E_i) and excite (E_e) an atom, average fraction (N_e/N_i) of excited to ionised atoms after a high-energy particle interaction and average kinetic energy lost via heat per ionisation electron, for liquid Argon, Krypton and Xenon. From [69].

In noble liquids, as well as in dense noble gases, triple atomic collisions take place

$$A^* + 2A \rightarrow A_2^* + A \tag{6.10}$$

to form diatomic excited molecules (excimers). These excimers decay radiatively, giving rise to the molecular continuum:

$$A_2^* \rightarrow 2A + h\nu_m \tag{6.11}$$

Noble liquids are virtually transparent to their own scintillation light from the molecular continuum, making it feasible to detect these photons even with large detector volumes.

In the absence of an applied electric field, all electron-ion pairs formed in the liquid recombine, releasing scintillation light that can be collected with a photosensitive detector coupled to the liquid. For an increasing electric field intensity, the recombination process reduces and charge can be collected instead. The total signal ($N_i + N_e$) is independent of the value of the electric field if both charge and light are collected [69].

6.3 Gaseous radiation detectors

Energetic particles of sufficiently high energy may excite and ionise noble gas atoms, creating electron-ion pairs or inducing the emission of de-excitation photons. Photons emitted due to the initial particle interaction are said to be primary scintillation. If an intense electric field is present, charge is accelerated and additional electron-ion pairs

and excited atoms are created due to the transfer of kinetic energy from electron collisions with the medium. Secondary scintillation light, also called electroluminescence, is emitted after this process. Detectors may rely on the detection of scintillation light or in the collection of charge produced during the multiplication process in the gas. Since the amount of collected charge will be proportional to the energy deposited in the medium by the initial particle, this latter type of detector is called a *proportional counter* [69].

Gas multiplication takes place in cascade, since electrons liberated after collisions with accelerated charge will also be accelerated. This process is described with the Townsend equation:

$$\frac{dn}{n} = \alpha dx \tag{6.12}$$

where n represents the number of drifting electrons and dn is the increase in n after a drift distance of dx. The first Townsend parameter α depends on the medium and it is a function of the applied electric field: it vanishes below the threshold for atomic excitation and ionisation and generally increases monotonically above that value. For the simple parallel plate geometry, the electric field and α become constants and the solution is

$$n(x) = n_0 e^{\alpha x} \tag{6.13}$$

an exponentially growing number of electrons. The total charge collected for an initial number of electrons n_0 after a distance of d would be $Q = n(d)q_e = q_e n_0 e^{\alpha d}$, and the gain or multiplication constant neglecting contributions from the ion current is defined as

$$G = Q/(n_0 q_e) \tag{6.14}$$

with a value of $G = e^{\alpha d}$ in this case. In case of very high gains ($G \sim 10^8$), or fast counting rates, charge may accumulate in the gas, distorting the electrostatic field and the linearity of response. The simple exponential result from equation 6.13 predicts $\alpha d \lesssim 20$ before space-charge effects start causing discharges (Raether limit [70, 71]).

Current in the electrodes signals particle interactions within the detector volume. However, it is not the collection of charge carriers in the electrodes that induces the current but the modification of the electric field lines around the electrodes as the charge moves. The Shockley-Ramo theorem [72, 73] greatly simplifies the calculation of the

induced charge and intensity in the electrodes, given the velocity of the charge carriers:

$$i = q\vec{E}_0 \cdot \vec{v} \tag{6.15}$$

where q is the carrier charge, $\vec{v}$ is the charge velocity and $\vec{E}_0$ is the *weighting* field, calculated under special conditions:

- All charge within the detector volume is ignored.
- The potential at the electrode where the induced charge is of interest is set to one.
- All other electrodes are grounded.

This field does not correspond to the actual electric field, which must still be calculated to obtain the field lines that will be followed by the charge carriers [69, 74].

Multiplication requires that free electrons move within the gas. Therefore, gases with low electronegativity must be chosen, and must generally be purified before sealing the detector or, in case of detectors operated in flow mode, directly within the gas circuit. Gases used in these devices may not only be ionised but also excited if insufficient energy is transferred during a collision with electrons during the multiplication process. In this case a visible or UV photon will be emitted as the atom relaxes to its ground state, causing further ionisation or excitation of other gas atoms, or resulting in the extraction of electrons from the detector walls. This effect causes spurious events and loss of energy linearity, it broadens the electron avalanche cloud and it therefore deteriorates position resolution as well. A small addition of polyatomic gases, such as methane (CH_4), has been proven to suppress the effects due to these photons thanks to their oscillatory modes of excitation, releasing the absorbed energy via heat instead of further ionising radiation. In this context, these gases are often called quenchers. Noble gases are generally used as proportional multiplication media, but gains greater than 100 can only be achieved if a small amount of quench gas is added [74].

6.3.1 Solid photocathodes

Gaseous detectors can be used to directly detect X-rays or other particles that deposit their energy in the gas, or they can be coupled to a scintillator and function as a pho-

tomultiplier, provided that a photocathode is placed within the gas medium. Typically, thin layers of materials with low work function are deposited on the detector window (semi-transparent) or on an electrode (reflective), to exploit the photoelectric effect and extract photoelectrons into the gas. The ejection of the photoelectron occurs from the surface opposite to the photon interaction in semi-transparent photocathodes, and from the same surface in case of reflective photocathodes. Reflective photocathodes can therefore be thicker and more efficient. The Quantum Efficiency (QE) of photocathodes, defined as

$$QE = \frac{\text{number of photoelectrons emitted}}{\text{number of incident photons}}, \tag{6.16}$$

depends not only on their geometry, but also on the material used, the substrate and the method of deposition. Different materials react differently to different photon wavelengths, and photoelectron ejection into the gas medium is affected by gas pressure as well. The proportion of photoelectrons that would be successfully ejected from the photocathode into the vacuum is termed extraction efficiency. When a gas medium is present, the proportion is lower by a factor termed collection efficiency.

6.3.2 Micro-patterned structrures

Current gaseous detector technology involves micro-patterned structures for electron avalanche multiplication, allowing for high counting rates with good energy resolution and the possibility of position measurement.

6.3.2.1 Gas Electron Multiplier

Gas Electron Multipliers (GEMs) consist on a thin insulating film, typically $\sim 50\ \mu$m thick Kapton, with copper layers printed on both sides. The metal is etched to create a hexagonal pattern of holes with a typical diameter of $\sim 70\ \mu$m and separated by $\sim 100\ \mu$m. When a high potential difference is applied between the two electrodes, free electrons are accelerated, following the electric field lines and colliding with gas atoms as they move, adding new electron-ion pairs to the process. Electrons are focused into the GEM holes, where most of the multiplication takes place. High gains can be achieved with a stack of GEMs, inducing a cascaded electron multiplication

process [75].

6.3.2.2 Micro-Hole and Strip-Plate

The Micro-Hole and Strip-Plate (MHSP) is an electron multiplier consisting on two charge amplification stages. Similarly to a GEM, a thin kapton substrate with metallised faces is used. GEM-like holes are etched through and a microstrip pattern is etched on the bottom surface of the structure: cathode strips and anode strips. A potential difference is applied between the top surface and the cathode strips, generating the electric field that focuses the electrons into the holes for the first multiplication stage. A bias voltage is also applied between the cathode and the anode strips to induce a second multiplication stage and produce signal in the anode strips [76]. One dimensional position of interaction can be inexpensively reconstructed by resistive charge division [77] or by independently measuring the signal out of each anode. A single MHSP can provide a $> 10^3$ multiplication factor. When perpendicular strips are etched on the top surface, 2D position reconstruction is possible and the microstructure is called 2D-MHSP [78].

6.3.2.3 THGEM

The evolution of the GEM was the Thick GEM, a similar structure with an order of magnitude bigger dimensions. Sub-millimetre thick standard Printed Circuit Board (PCB) is used as a substrate, where electrodes are cladded and 0.3-1.0 mm diameter holes are mechanically drilled with a pitch of $\sim$ 1 mm, providing more robustness against physical deformation and damage due to electrical discharges compared to a GEM. Larger-area detectors can be built and higher gains can be achieved. Typically a 0.1 mm rim is etched around the holes, reducing even further the probability of discharges. The operation principle is equivalent to that of the GEM, but electron collection efficiency is higher due to the greater hole diameter. Similarly to GEMs, THGEMs can also be used in a cascade to provide greater amplification with lower bias voltage [79, 80].

6.3.2.4 THCOBRA

Like the GEM, the evolution of the MHSP is the THCOBRA, a structure combining the robustness and cheapness of the THGEM and the two stages of multiplication and position reconstruction capabilities of the MHSP. PCB is used as a substrate, with its faces metallised and holes mechanically drilled with the same parameters as the THGEM. On the bottom surface of the THCOBRA a strip pattern similar to that of the MHSP is etched, with cathode strips surrounding the THGEM-like holes and the anode strips between the cathodes. The name *THCOBRA* was given due to the snake-like shape of the anode strips. Like the 2D-MHSP, the THCOBRA can reconstruct 2D-position of interaction if strips are etched on the top surface, perpendicular to the anode strips, in which case the structure is termed 2D-THCOBRA (see figure 6.2).

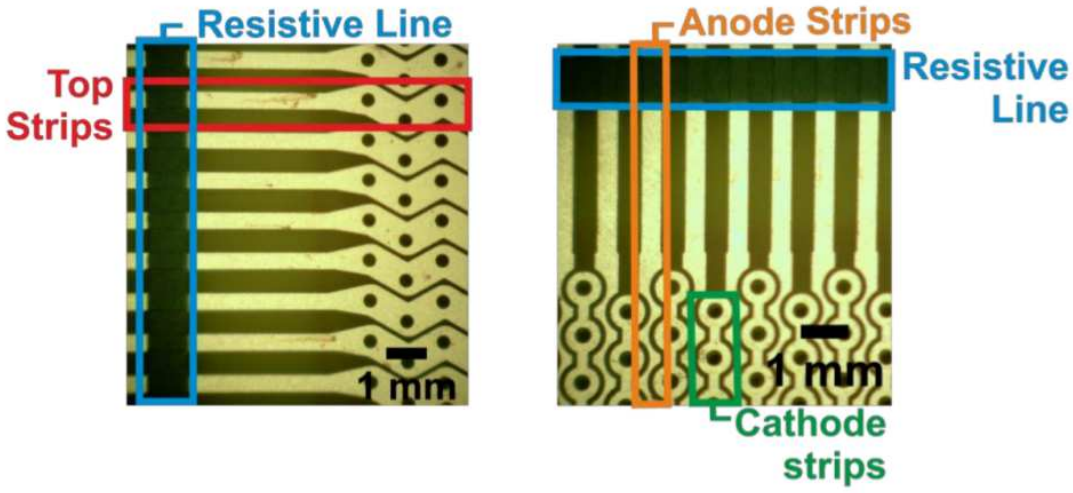

Figure 6.2: Detailed view of a 2D-THCOBRA top (left) and bottom (right) sides, showing, respectively, the top strips and the cathode and anode strips with their resistive lines. From [81].

6. INTRODUCTION TO RADIATION DETECTORS

Chapter 7

Cryogenic Gaseous Photomultiplier for Position Reconstruction of Liquid Argon Scintillation Light

7.1 Introduction

Noble liquids (xenon, krypton and argon) are growing in importance in particle physics experiments [82, 83, 84, 85, 86] and they have been proposed as an alternative to crystals in medical particle detectors such as Positron Emission Tomography (PET) scanners [87]. In PET scanners, the position resolution is limited by the granularity of the 360° crystal and photomultiplier tube (PMT) arrays, and the energy resolution by the crystal scintillation light yield (NaI(Tl): 38 ph/keV, BGO: 15% relative to NaI(Tl), GSO: 30%, LSO: 75% [88]) and the photodetector resolution. Compared to conventional scintillation crystals, noble liquids have similar or superior scintillation light yield (liquid argon: $\lesssim$ 51 ph/keV [68], liquid xenon: $\sim$ 40 ph/keV [89]), allowing for a similar or improved energy resolution with relatively small volumes [90] despite their lower density. Furthermore, they are transparent to their own scintillation light and, unlike solid state detectors, degradation of the medium can be counteracted by continuously circulating the liquid through a purifier. Liquid xenon is commonly used due to its high density and scintillation light wavelength at 178 nm, offering a better stopping power than the other liquids and the possibility of detecting the light with

cryogenic photomultipliers [91]. At lower light wavelengths, such as the peak of argon scintillation ($\sim$ 127 nm), wavelength shifters must be used to continue working with PMTs [92]. However, liquid argon is an attractive medium due to its very low cost compensating for its lower detection efficiency, although alternative light read-out methods are required to avoid the granularity limitations imposed by PMTs and the efficiency loss introduced by wavelength shifters.

Position sensitive Gaseous Photomultipliers (GPMs) can be manufactured with large active areas and with photocathodes sensitive to UV noble liquid scintillation light, offering a cheap alternative to vacuum and solid state photon detectors and with a position resolution on the order of 100 μm. Hole-type micropatterned structures like Thick Gaseous Electron Multipliers (THGEMs) are indispensable components in such GPMs. When arranged in a cascade, with the first structure coated with a thin film of photosensitive material and operated at high voltages immersed in a noble gas, they focus the photoelectrons into the holes and provide additional electrons and positive ions via collisions with the gas atoms. The cascaded structure allows for lower individual operating voltages and discharge probability while increasing the detector gain. Caesium Iodide (CsI) can be used to form a reflective photocathode [77], with sensitivity to UV light below the 220 nm threshold with a quantum efficiency from $\sim$ 15% for liquid xenon scintillation (178 nm) to $>$ 60% for liquid argon scintillation light (127 nm) (see Figures 7 and 8 in [93]) and a time resolution $<$ 10 ns [94, 79, 95].

The stability of position sensitive GPMs at cryogenic temperatures down to 88 K has been tested with positive results [96], confirming the expected reduction in photoelectron extraction efficiency with increased gas density at low temperatures. Liquid xenon scintillation light detection has also been performed with a GPM detector [97]. In this article the construction, operation and testing of a prototype GPM intended for liquid argon scintillation light is presented. Voltage settings are optimised at room temperature to maximise the gain, and the position resolution is studied. Further tests towards the operation of the detector submerged in liquid argon are also carried out: structural tests in liquid Nitrogen, room temperature multiple-photon position reconstruction and gain stability.

7.2 GPM Detector Design and Operation Principle

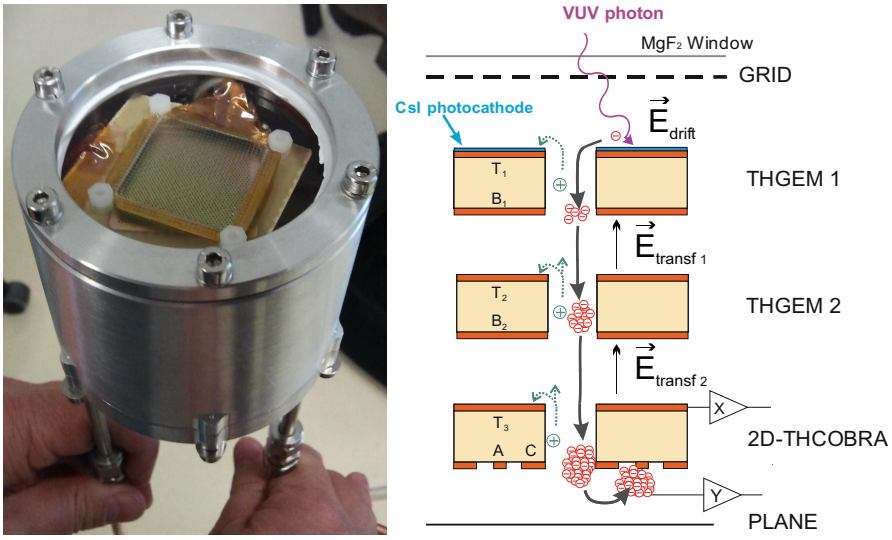

(a) (b)

Figure 7.1: (a) Detector prototype. The MgF_2 window, vacuum-sealed with Teflon gaskets to the aluminium cylinder, the grid and the first THGEM are visible. (b) Schematic representation of the detector and its operation principle.

The detector used in this work is shown in Figure 7.1a. The design comprises three micropatterned structures housed in an aluminium cylinder of 10 cm diameter and 10 cm height, with a 3 mm thick circular window on one end and two diametrically opposed gas inlet/outlet perforations on the other. A stainless steel CF flange with nickel pins is used for signal and power feedthrough, with all structural components vacuum-sealed with Teflon gaskets.

The window material is Magnesium Fluoride (MgF_2) due to the high typical transmittance in the VUV range ($T > 50\%$ at 121 nm [98]). The three micro-structures comprise two THGEMs and a 2D-THCOBRA, placed in parallel with separations of 3 mm, copper-cladded 400 μm thick G10 sheets with 400 μm holes mechanically drilled, without rim and with 800 μm pitch in the case of the THGEMs and with an 80 μm rim and a 1 mm pitch in the case of the 2D-THCOBRA. Strips 100 μm wide were etched on the top and bottom surfaces of the 2D-THCOBRA following a photolithography process, and these are joined by resistive lines deposited by serigraphy

(see Figure 6.2). A grid is placed on top of the first THGEM, at 2 mm, and a copper plane is placed after the 2D-THCOBRA at 2 mm as well. The detector is operated in flow mode with a gas mixture of 95% Neon and 5% CH_4 that fills the inside of the cylinder and serves as multiplication medium. As shown in Figure 7.1b, a VUV photon that enters through the MgF_2 window and interacts in the CsI photocathode deposited on top of the first THGEM may produce emission of a photoelectron with a certain probability. The photoelectron drifts due to the electric field between the THGEM top and bottom surfaces (T_1, B_1) into the THGEM holes. As it accelerates in the gas medium, collisions with Neon atoms start an electron multiplication process. The electron cloud extracted from the first THGEM holes drifts towards the second THGEM due to the transfer field $\vec{E}_{\text{transf 1}}$. A second multiplication occurs in the second THGEM and the electron cloud then drifts towards the 2D-THCOBRA in $\vec{E}_{\text{transf 2}}$. A bias voltage V_{CT} is applied between the top strips (T_3) and the cathode (C) on the bottom of the structure, generating a field in which the electron cloud accelerates and multiplies. Further multiplication occurs due to the voltage V_{AC} between the cathode and the anode strips (A), where the signal is collected and divided. An opposite sign signal is induced in the top strips [77], allowing for 2D reconstruction of the position of incidence of the VUV photon.

7.3 Experimental Setup and Methods

Detector gain measurements and image acquisition are performed simultaneously at room temperature. The experimental setup is shown in figure 7.2. For all measurements, a collimated Hg(Ar) lamp is used to provide the VUV photons producing the signals. The signals from the top and anode resistive lines in the 2D-THCOBRA are preamplified and digitised with a calibrated Cremat CR-111 and CAEN N1728B NIM ADC module (4 channels, 14 bits, 100 MHz sampling rate), respectively, and the image is reconstructed by weighting the integrated signals from each end of the resistive lines following the principle of resistive charge division [99]. Figure 7.3 shows the calibration of the electronics and data acquisition system.

The single photoelectron collected charge distribution is well modelled by a Polya

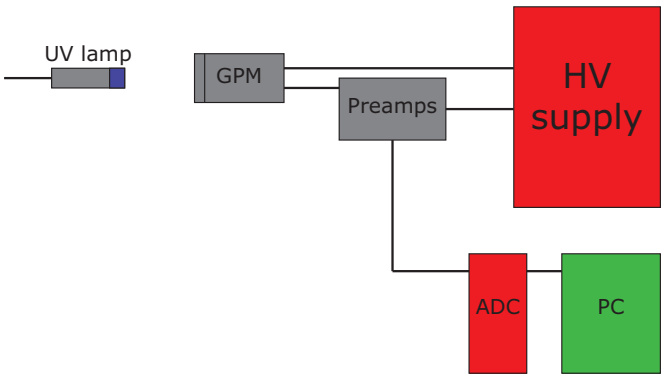

Figure 7.2: Experimental setup. A Hg(Ar) lamp provides the UV photons producing the signals, preamplified with Cremat CR-111 preamplifiers and digitised with a CAEN N1728B NIM ADC module.

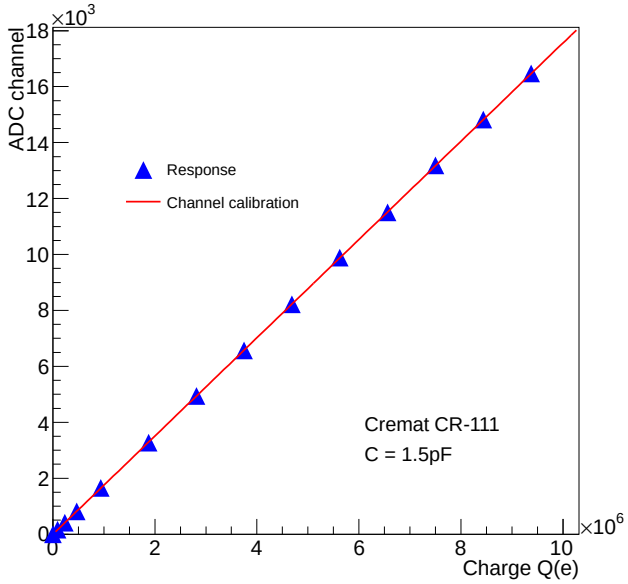

Figure 7.3: ADC channel calibration. Known pulses were sent to the ADC module through the preamplifiers to obtain a factor of 0.001757 ADC/e for the anodes combined.

distribution (see e.g. [100]) of the form

$$P_m(g) = \frac{m^m}{\Gamma(m)} \frac{1}{G} \left(\frac{g}{G}\right)^{m-1} e^{-m\frac{g}{G}} \tag{7.1}$$

where g is the charge, m a dimensionless real parameter and G the detector Gain. In log scale the function has a linear component of the form

$$\log(P_m(g)) \sim -m\frac{g}{G} + \cdots \tag{7.2}$$

Relative gain comparisons can be performed using the inverse slope of the linear part of the distribution [101, 102, 103].

To measure the photoelectron collection efficiency of the detector, one end of the anode-strip resistive line is disconnected, so that all the charge flows to the other end. After preamplification, the signal is amplified with a Canberra 2022 (shaping time 2 μs, $G = 100$ and $G_f = 1$) and then digitized using an Amptek MCA8000A.

7.4 Results: detector characterisation

To achieve optimal performance, the detector must hold its structural integrity at liquid argon temperatures and retain a stable and predictable gain. Due to the nature of the liquid argon scintillation light, the detector has to detect simultaneous multiple photon interactions. In this section, measurements to determine the detector performance are presented. First, measurements to characterise the GPM behaviour are performed at room temperature: gain, photoelectron collection efficiency and position resolution, and finally, preliminary tests to evaluate the detector behaviour under simulated liquid argon conditions are carried out: multiphoton position reconstruction, gain stability and evolution and detector structural integrity tests at cryogenic temperatures.

The detector gain was measured at room temperature as a function of the two 2D-THCOBRA potentials, V_{AC} and V_{CT}, with the potentials on THGEM1 and THGEM2 fixed at 595 V and 550 V respectively, empirically chosen as a compromise between efficiency and discharge probability, and the transfer fields set to $E_{\text{transf 1}} = E_{\text{transf 2}} =$ 300 V/cm. Equation 7.1 was used to extract the absolute gain for each of the voltage settings. The gain as a function of the Anode strips−Cathode potential V_{AC} is shown

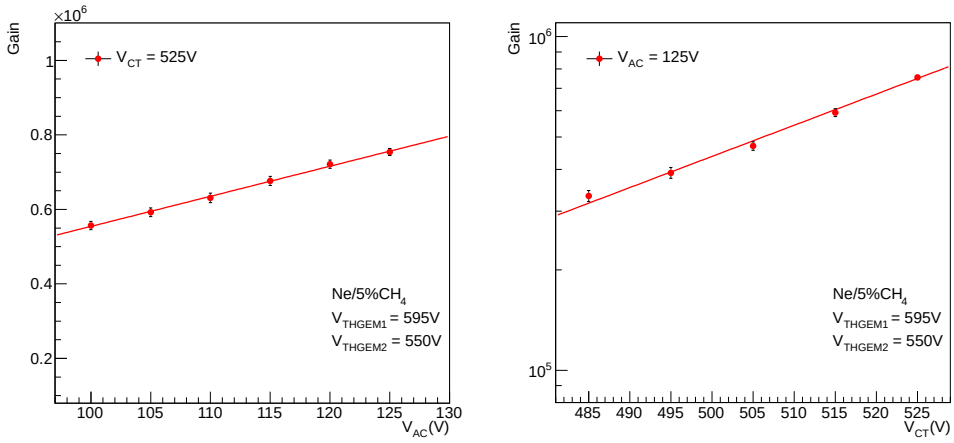

(a) (b)

Figure 7.4: Detector gain as a function of the Anode strips−Cathodes potential (a), and as a function of Top strips−Cathodes potential (b), in number of collected electrons per photoelectron.

in Figure 7.4a for V_{AC} from 100 V to 125 V in steps of 5 V and for Cathodes−Top strips potential fixed at $V_{\mathrm{CT}} = 525$ V. The expected behaviour was exponential [77], but the relatively low potential chosen to minimise discharge probability gives a linear observed behaviour, indicating that no additional electron multiplication occurs in the gas at this stage. In Figure 7.4b, gain measurements as a function of V_{CT} are presented. V_{CT} is varied from 485 V to 525 V in steps of 10 V for a constant $V_{\mathrm{AC}} = 125$ V. In this range, the observed variation has an exponential behaviour, as there is electron multiplication taking place in the 2D-THCOBRA holes, between the top strips and the cathodes. Based on this study, optimal operation voltages were chosen ($V_{\mathrm{AC}} = 125$ V and $V_{\mathrm{CT}} = 525$ V), corresponding to a gain of $G = 8 \cdot 10^5$ (see Figure 7.5). For these values, detector operation is stable and there is a low discharge rate.

The drift field between the first THGEM and the grid has a strong effect on the extraction of photoelectrons from the CsI surface. In Figure 7.6, the detector gain is plotted as a function of the drift potential with respect to the top of THGEM1, where it is shown that the gain falls rapidly when applying a non-zero potential. A negative potential stops the photoelectrons from being extracted from the CsI layer and worsens the charge multiplication that takes place immediately before the first THGEM holes.

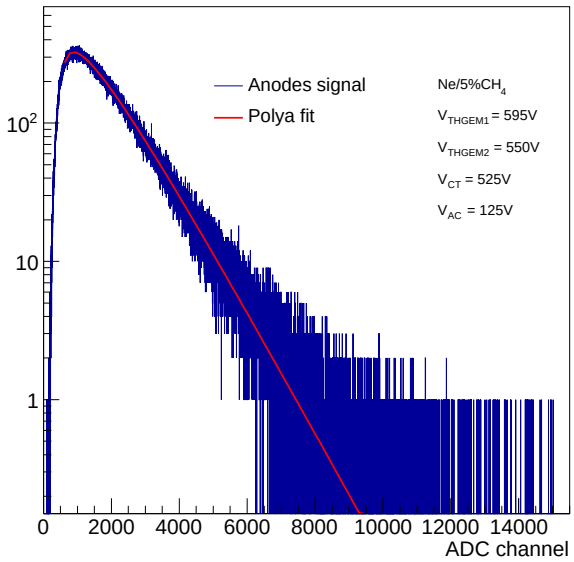

Figure 7.5: Distribution of the collected charge for single photoelectrons under optimal operation voltages (blue) and polya fit (red) yielding a gain of $G = 8 \cdot 10^5$ after ADC calibration.

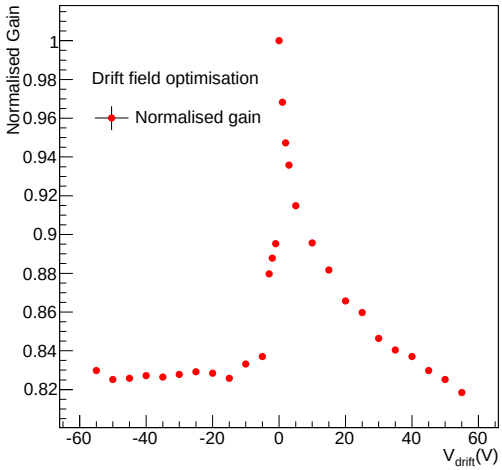

Figure 7.6: Detector gain as a function of drift potential

The gain flattens out at ~ 83% of the maximum for $V_{\text{drift}} \simeq -10$ V. However, with increasingly positive potential the extraction of photoelectrons is aided by the additional electric field, and the effect on the field lines is less important, producing a slower gain drop. The optimal value in terms of gain was $V_{\text{drift}} = (0 \pm 0.5)$ V, so the grid potential was set to zero with respect to the first THGEM for the rest of the tests.

Maximising the detector collection efficiency is especially important when working in single-photoelectron mode. This ratio approaches 1 as V_{THGEM1} is increased, and to measure it the gain is kept approximately constant for different voltage settings by comparing a reasonably linear region of the collected charge spectra and applying equation 7.2. The comparison is performed by integrating this region to estimate the amount of collected charge for different THGEM1 potentials [104, 105]. The result is shown in Fig 7.7, where $\epsilon_{\text{coll}} \sim 1$ at $V_{\text{THGEM1}} = 595$ V. At this bias voltage, the surface field between holes is high enough for the detector to reach an extraction efficiency higher than 70% [104].

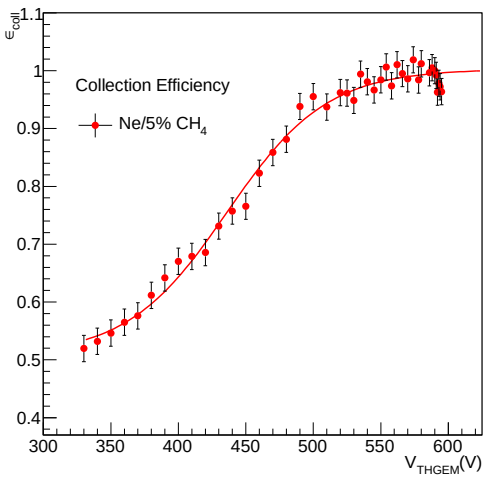

Figure 7.7: Photoelectron collection efficiency as a function of THGEM1 potential. Data is normalised so that the fit tends asymptotically to 1.

To determine the GPM position resolution the edge spread function method was applied to one of the edges of the pattern created by a hole of the first THGEM in the image (see Figure 7.8), following the method described in [106]. Projections of the

edge in the x and y-directions are fitted to a Boltzmann function[1] and the spread is calculated from a gaussian fit to its derivative, as shown in the figure. The result of the fit yields $< 90 \pm 30$ μm in the direction of the anode strips and 90 ± 30 μm in the direction of the top strips.

An experiment was set up to test the detector ability to reconstruct UV light from naturally occurring sources. Flame light below the CsI 220 nm threshold should be detectable by the GPM [107], so a lit candle was placed in front of the detector, collimated and attenuated with plastic film, as shown in Figure 7.9 (left). In the absence of attenuation, flame UV light overwhelmed the detector, causing discharges due to space-charge accumulation, confirming the hypothesis. With enough attenuation, it was possible to ensure that only single photons hit the detector. An image built after a 3 s exposure to candle light is shown in Figure 7.9 (right). A series of frames were recorded and a movie showing the movement of the UV light sources within the flame can be found in [108]. In combination with an IR detector, a 360° collimated GPM can be used for outdoor fire detection.

Liquid argon produces $<$ 51000 scintillation photons per MeV of incident particle [68]. These photons can extract photoelectrons from the GPM CsI photocathode ($QE > 10\%$ [93]). Assuming that the detector is observing 0.511 MeV gamma-ray interactions in a cylinder of liquid argon of 10 cm height with a MgF_2 window (70 mm diameter), the number of photoelectrons generated is on the order of $\mathcal{O}(10^1) \sim \mathcal{O}(10^2)$. Therefore, the system must be able to reconstruct events with multiple photons that simultaneously produce photoelectrons in the photocathode.

To simulate argon emission, a spinning disk with a slit allows pulses of UV light from the Hg(Ar) lamp to be detected, being integrated for 10 μs. The detector, operated at room temperature at 20 cm from the light source was moved from right to left in steps of $\sim$ 2 cm to determine if the average position of the photon pulses would vary accordingly. In Figure 7.10 three collected charge distributions and their corresponding position distributions are shown. The results show that the detector can simultaneously reconstruct the energy deposition of multiple photons and their average position of arrival at the photocathode. The first measurement (violet charge distribution, position (a)) suffered from more noise from one of the channels, hiding most of the multiple photon signal due to pileup conditions. The trigger threshold was increased for the rest

[1] Boltzmann function: $y = \frac{A_1 - A_2}{1+\exp([x-x_o]/d)} + A_2$

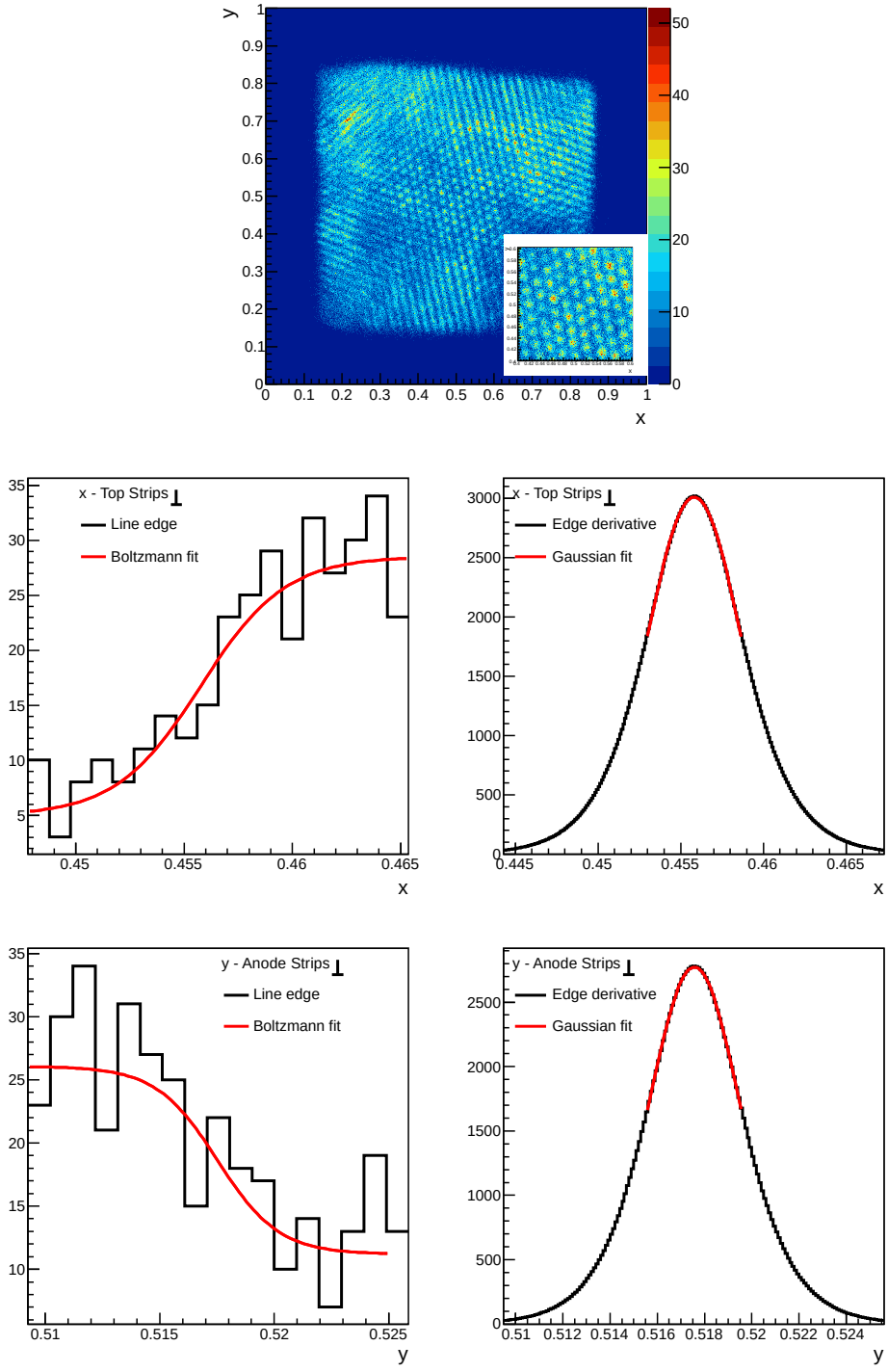

Figure 7.8: Position resolution measurement with the Line Spread Function method. The spread of one of the hole edges in the THGEM1 imaged pattern is fitted to a Boltzmann function. The derivative of the fit is taken and fitted to a gaussian to obtain the resolution. The results obtained are $\sigma = 90 \pm 30$ μm in the x-direction (top strips) and $\sigma \lesssim 90 \pm 30$ μm in the y-direction (anode strips). Scale: 3.12 cm = 1.

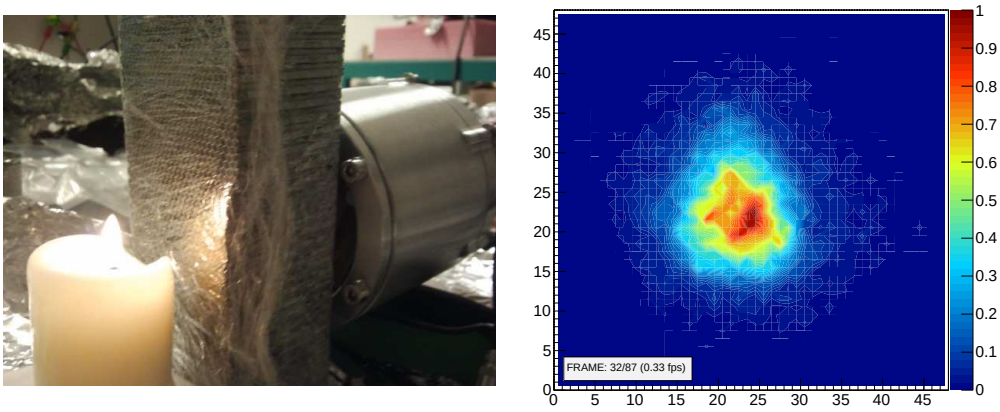

Figure 7.9: Experimental setup for candle tests. A lit candle in front of the GPM, UV radiation collimated and attenuated with plastic film (left). Example image obtained from a 3 s exposure time, showing the burning candle flame shape (right). A full animated sequence can be watched in [108]. Scale: 3.12 cm = 48px.

of the measurements. It is worth noting that when operated in multiphoton mode, the detector loses its single photon position capability (reconstructed always around the centre) due to the long integration time.

In order to test the stability of the gain during prolonged time periods, the GPM was set up to detect single photons from the UV Hg(Ar) lamp. The experiment ran for approximately 44 h, collecting data in intervals of 3 min. The following variables were measured: anode and top-strips gain, pressure of the gas entering and leaving the detector, room temperature and instantaneous discharge times. The purely exponential part of the measured charge distributions for every 3 min interval was fitted to extract the gain. Every signal indicating a high current in the voltage supply (discharge) was recorded.

A standard Principal Component Analysis (PCA) reveals linear dependence between gains, room temperature and pressure of the gas leaving the detector. In Figure 7.11, the normalised pressure (green histogram) and temperature (blue histogram) are shown together with the gain from the anode strips channels (purple histogram), as a function of time[1]. Discharges are shown as red points on the gain distribution.

[1]Gain is normalised to an arbitrary central value (1200 ADC/e^-). Time is normalised to the length

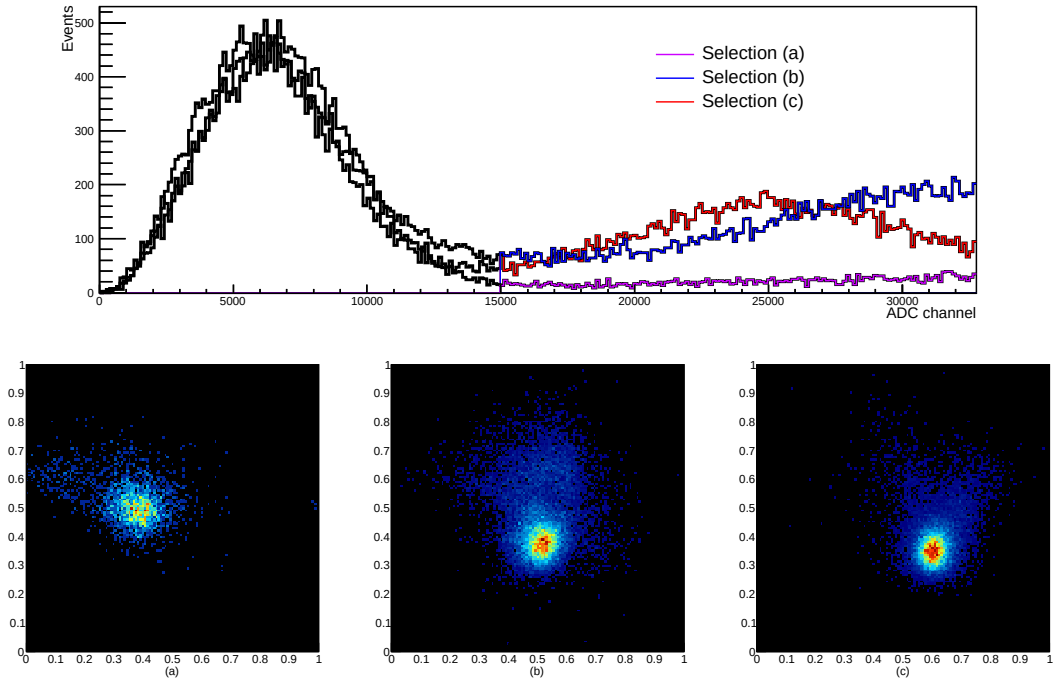

Figure 7.10: Displacement of average position and collected charge distribution of multiple photon interactions. The single-photon polya charge distribution is modified by multiple photon interactions appearing in the high end of the spectrum as a resonant peak, revealing the average energy deposited in the detector per multiphoton event. A different average number of simultaneous photons interact in the photocathode in cases (b) and (c), and hence their collected charge distributions do not peak at the same point. The maximum number of available ADC channels was reached and the distributions cannot be fully shown. An excessive number of low-energy events during data-taking hides the multiphoton peak in (a) due to pileup. Scale: 3.12 cm = 1.

The ratio between top and anode strips gain is shown in Figure 7.12, stable at a value of ~ 67%.

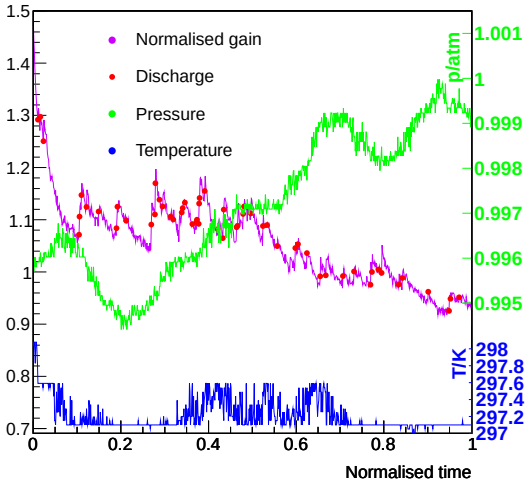

Figure 7.11: Normalised pressure (green histogram), temperature (blue histogram) and gain from the anode strips channels (purple histogram), as a function of time. Discharges are shown as red points on the gain distribution.

The variation in gain observed in Figure 7.11 is mainly due to the variation in room temperature and pressure and to occasional discharges, and can be described by:

$$\frac{dG}{dt} = \frac{\partial G}{\partial p}\frac{dp}{dt} + \frac{\partial G}{\partial T}\frac{dT}{dt} + \frac{\partial G}{\partial t}\bigg|_{\text{discharge}} \tag{7.3}$$

Where the partial derivatives are calculated for all the other variables constant. Integrating this expression yields:

$$\begin{aligned} G(p(t), T(t), \text{disch}(t)) &= G_0 + \frac{\partial G}{\partial p}p(t) + \frac{\partial G}{\partial T}T(t) + G(\text{disch}(t)) \\ &= G_1(p(t)) + G_2(T(t)) + G_3(\text{disch}(t)) \end{aligned} \tag{7.4}$$

The behaviour of the gain with respect to pressure variations $G_1(p)$ was studied in regions of constant room temperature ($T = 297.1$ K). On average, a discharge occurred

of the experiment (145711 s or 40.48 h)

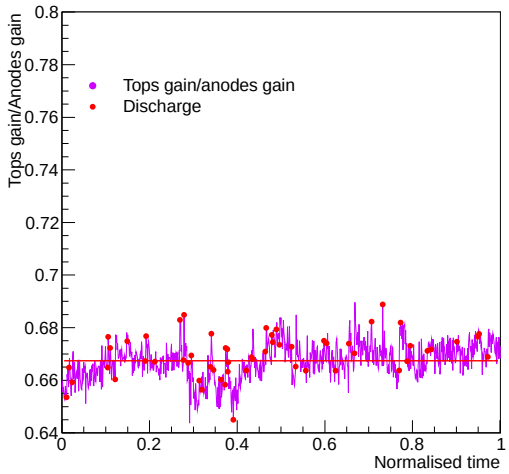

Figure 7.12: Ratio of the gain measured from the top strips signal to the gain measured from the anode strips signal. A stable value of ∼ 67% is observed during operation.

every 46 minutes, so it was required that no discharge occurred in the last 30 mins. A linear correlation between pressure and gain was established, with negative slope. Analogously, $G_2(T)$ was fitted and a positive slope was found. The discharge-dependent term is obtained by calculating $G_3(\text{disch}(t)) = G(p, T, disch) - G_1(p) - G_2(T)$. As shown in Figure 7.13, discharges are responsible for a ±10% variation around the mean at (0 ± 2)%.

Given the stable operation and multiple photon detection capabilities, preliminary structural tests at cryogenic temperatures were carried out. Initially, the MgF_2 window was substituted for a more robust aluminium window. The detector was then evacuated to a pressure of $\sim 10^{-6}$ mbar and then cooled down to 77 K with liquid Nitrogen. After reaching stability, the detector was removed from the liquid and was left to heat up to room temperature. During this stage, the pressure increased to 200 mbar, an encouraging result considering that the gas pressure will be kept at ∼ 1 atm during normal operation. To further ensure structural integrity and good performance of the Teflon gaskets, an additional test was performed with a dummy glass window. argon was allowed to flow through the detector until all air had been removed. When the pressure reached 1.2 atm, all valves were shut and the detector was cooled down using liquid Nitrogen. The pressure was maintained at ∼ 1.2 atm by adding more argon,

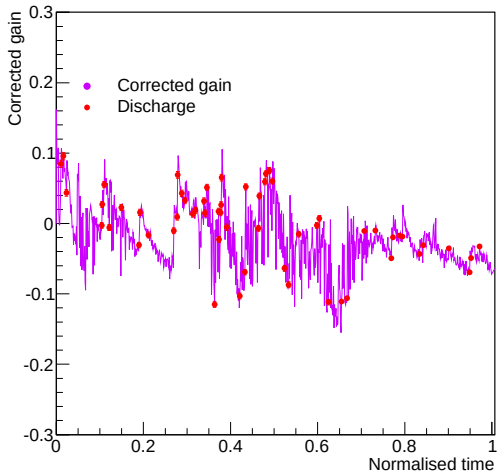

Figure 7.13: Gain evolution after correcting for the variation due to temperature and pressure. Discharges induce oscillations of ±10% around the mean.

since the gas freezes below 84 K. When equilibrium was reached, the liquid Nitrogen was removed and a block of solid argon was visible through the glass window of the detector. As the system warmed up to room temperature, the flow of escaping argon was regulated to keep the pressure constant. When the pressure dropped to 1 atm all valves were shut. No water, in liquid or solid state, was visible inside the detector volume or on the inner surface of the glass window after all the argon evaporated and the system reached room temperature. The detector was pumped down to 10^{-6} mbar to test the glass window strength, without problems. After turning off the pump the pressure did not go above 10 mbar, hence the system is vacuum tight with Teflon gaskets and a glass window, even after the process of cooling and heating. While in the actual prototype a MgF_2 window is used, there is no reason to expect a significant change with respect to the measurements performed with glass.

7.5 Conclusions

A new large area Gaseous Photomultiplier utilizing a cascade of Thick GEM layers intended for gamma-ray position reconstruction in liquid argon is proposed. A prototype designed to operate at cryogenic temperatures inside the liquid phase and to reconstruct

liquid argon scintillation light was built. A number of performance measurements were carried out at room temperature and stable operation high-voltage settings: photoelectron collection efficiency, position resolution and stability. A photoelectron collection efficiency on the order of 1, a gain of $8 \cdot 10^5$ per photoelectron and a position resolution better than 100 μm were measured. Discharges were observed every 46 min of operation on average (0.1 discharges/($h \cdot cm^2$)). Detector gains were stable for the whole data taking period within ±10%, showing a slow charging-up effect after every discharge. Gain variations due to pressure and temperature disappear when the two variables are under control in the laboratory. However, to reduce the discharge rate it is necessary to operate with lower bias settings, limiting the stability of the gain to the above-mentioned ±10%.

The proposed detector has potential applications ranging from medical physics and engineering, to particle physics. Initial tests of robustness against cryogenic temperatures were performed successfully. The next essential step would be to demonstrate the operation of the Gaseous Photomultiplier inside the liquid argon phase.

7. CRYOGENIC PSGPM FOR LIQUID ARGON SCINTILLATION RECONSTRUCTION

Chapter 8

Summary

The QED Final State Radiation photons and a method for their recovery in ATLAS were introduced in chapter 3. The algorithm for FSR recovery was improved with respect to the original to include not only collinear FSR photons from $Z \to \mu\mu$ events (efficiency: 70%, purity: 85%) but also non-collinear FSR photons from $Z \to ee$ and $\mu\mu$ events (efficiency: 60%, purity: > 95%). Excellent data-Monte Carlo agreement and pileup independence was found. The algorithm was used to improve the Higgs mass measurement in the $H \to ZZ^* \to 4\ell$ channel and to correct the dimuon mass distribution in the Higgs search in the $H \to Z\gamma$ channel. Additionally, the FSR photons from Z decays to $\ell\ell\gamma$ were used to cross-check the photon calibration, extrapolated from the $Z \to ee$ electron calibration and used in the Higgs mass measurement in the $H \to \gamma\gamma$ channel, with a precision better than 0.5%.

Chapter 5 introduced the search for the Higgs boson in the $H \to Z\gamma$ channel, yielding an upper limit at the 95% CL for the cross section times branching ratio of 0.13 to 0.5 pb measured from the $\sqrt{s}$ = 8 TeV data sample, and a cross section divided by Standard Model expectation at m_H = 125.5 GeV of $11 \times SM$ at 95% CL measured in the combined $\sqrt{s}$ = 7 TeV and 8 TeV data sample. The improvement introduced in the limits by the FSR correction is 2%.

During LHC Run II Final State Radiation photons will again play an important role in the photon calibration and the mass reconstruction of particles decaying to electrons or muons. Due to the increase in luminosity and centre-of-mass energy of operation ($\sqrt{s}$ = 13 TeV), conditions affecting FSR photon reconstruction, including pileup, will change, so the algorithm will have to be tested and re-optimised if necessary. Up to

300 fb $^{-1}$ will be made available to the ATLAS detector for new studies and improved searches.

A position sensitive Gaseous Photomultiplier was built in order to reconstruct liquid Argon scintillation light, and it was presented in chapter 7. The detector comprises two THGEMs with CsI reflective photocathode on the first structure and a 2D-THCOBRA, arranged in cascade, encased in an aluminium cylinder with a MgF_2 window transparent to VUV light from liquid Argon scintillation. It is operated in flow-mode with Ne/5%CH_4. Initial calibration and tests were performed at room temperature: $8 \cdot 10^5$ gain per photoelectron, $\sim$ 100 μm position resolution, $\sim$ 1 collection efficiency and a rate of 0.1 discharges/$(h \cdot cm^2)$ were measured under optimised bias settings. The effects of room temperature and pressure variations on the stability of the gain were disentangled and the variation induced by the occasional discharges ($\pm$10%) could be determined. It was proven that the GPM can reconstruct the average position of interaction of simultaneous photons, essential for liquid Argon scintillation light position measurement. Preliminary structural tests at cryogenic temperatures were carried out in liquid Nitrogen, proving that the detector is able to withstand such conditions maintaining its vacuum-tightness.

Future experiments will involve the operation of the detector in liquid Argon and the reconstruction of ultraviolet photons provided by LEDs and scintillation light from particle interactions in the liquid. Successful position reconstruction of scintillation light will be an important milestone towards the application of cryogenic GPMs in nuclear medicine devices such as PET scanners.

9

Glossary

ADC: Analog to Digital Converter.
Alpgen: a generator of hard multi-parton processes in hadronic collisions.
Auger effect: the emission of an electron from an atom when a vacancy in its inner-shell is filled by another electron from a more loosely bound shell.
Bremsstrahlung: the loss of energy by radiation from a charged particle accelerated in an electromagnetic field.
Crystal Ball: a function consisting of a gaussian core and a power-law low-end tail, used to model processes in which part of the energy may be lost.
Electronegativity: a chemical property describing the tendency of atoms to attract electrons towards themselves. A higher electronegativity represents a higher attraction.
EM: Electromagnetic.
FSR: Final State Radiation.
Gaussian-Sum Filter (GSF): a technique used in ATLAS to incorporate electron bremsstrahlung losses in the track reconstruction.
Geant4: a toolkit for the simulation of the passage of particles through matter.
GPM: Gaseous Photomultiplier.
HERWIG: a Monte Carlo simulation package for Hadron Emission Reactions With Interfering Gluons.
LAr: Liquid Argon.

Levi-Civita symbol: totally antisymmetric tensor density of weight -1, represented in cartesian coordinates by $\epsilon_{a_1,a_2,...,a_n} = 1$ if $(a_1, a_2, ..., a_n)$ is an even permutation of $(1, 2, ..., n)$; -1 in case of an odd number of permutations and 0 otherwise.

Monte Carlo (MC): a Monte Carlo simulation uses random numbers drawn from a probability distribution to evaluate mathematical expressions that are not easily tractable with analytical methods.

Minimum Ionising Particle (MIP): a particle with a mean rate of energy loss through matter near the minimum given by the Bethe-Bloch equation.

MC@NLO: a parton shower Monte Carlo that computes hard partonic processes with full Next-to Leading Order QCD corrections.

NLO, **NNLO**, **LO...:** the amplitudes of particle interactions are perturbatively calculated from a power series of the coupling constant. The Leading Order (LO) or tree-level term is represented by a Feynman diagram with no loops. Higher-order terms are represented by diagrams with an increasing number of loops: Next-to Leading Order, Next-to-Next-to Leading Order, etc...

Parton Distribution Function (PDF): measured for each different parton contained in the nucleon of interest, the PDF $f(x)$ is the distribution of the probability of finding a parton of flavour f with a fraction x of the nucleon momentum.

PET: Positron Emission Tomography.

Principal Component Analysis (PCA): a procedure that produces a set of linearly uncorrelated variables from a set of correlated variables via an orthogonal transformation.

Topological cluster: a cluster of calorimeter cells with a variable size that depends on the significance of the cells. The significance is calculated as a ratio of the cell noise and the energy deposited in the cell. The topo-seeded clustering algorithm centres a fixed-sized window on the cluster centre found by the topological algorithm.

Photolithography: a microfabrication process involving the transfer of a geometric pattern from a photomask onto a light-sensitive chemical deposited on a substrate, using light. Further chemical treatment engraves the pattern on the substrate or allows for the deposition of the desired material onto it.

PHOTOS: a software package for the simulation of QED radiative corrections in resonance decays.

POWHEG: POsitive Weight Hardest Emission Generator.

PSGPM: Position Sensitive Gaseous Photomultiplier.
PYTHIA: a software package for the generation of high energy collisions that models the physics of hard processes and the evolution to multihadronic final states.
Serigraphy: a printing technique that uses a mesh to transfer a material onto a substrate. Blocking certain areas of the mesh allows to obtain the desired pattern.
Sherpa: a high-energy particle collision event generator providing complete hadronic final states.
VUV: Vacuum Ultra Violet, light with a wavelength in the range $\lambda \in (100, 200)$ nm, strongly absorbed by atmospheric oxygen.

9. GLOSSARY

References

[1] D. Griffiths. *Introduction to Elementary Particles*. Second edition. New York, USA: John Wiley & Sons.

[2] C. L. Cowan Jr. et al. Detection of the Free Neutrino: A Confirmation. *Science* 124 (July 1956), pp. 103–104.

[3] J. Beringer et al. Review of Particle Physics. *Phys. Rev. D* 86 (2012), p. 010001.

[4] A. Djouadi. The anatomy of electroweak symmetry breaking: Tome I: The Higgs boson in the Standard Model. *Physics Reports* 457.14 (2008), pp. 1 –216.

[5] P. W. Higgs. Broken Symmetries and the Masses of Gauge Bosons. *Phys. Rev. Lett.* 13 (1964), pp. 508–509.

[6] F. Englert and R. Brout. Broken Symmetry and the Mass of Gauge Vector Mesons. *Phys. Rev. Lett.* 13 (1964), pp. 321–323.

[7] G. S. Guralnik, C. R. Hagen, and T. W. B. Kibble. Global Conservation Laws and Massless Particles. *Phys. Rev. Lett.* 13 (1964), pp. 585–587.

[8] L. Evans and P. Bryant. LHC Machine. *JINST* 3.08 (2008), S08001.

[9] *Big Science - The LHC in pictures*. https://bigscience.web.cern.ch/bigscience/en/lhc/lhc2.html. Visited on 04-2015.

[10] The first LHC protons run ends with new milestone. *CERN Press Office* (Dec. 2012).

REFERENCES

[11] ATLAS Collaboration. Observation of a new particle in the search for the Standard Model Higgs boson with the ATLAS detector at the LHC. *Phys. Lett. B* 716.1 (2012), pp. 1 –29.

[12] S. Chatrchyan et al. Observation of a new boson at a mass of 125 GeV with the CMS experiment at the LHC. *Phys. Lett. B* 716.1 (2012), pp. 30 –61.

[13] ATLAS Collaboration. Measurements of Higgs boson production and couplings in diboson final states with the ATLAS detector at the LHC. *Phys. Lett.* B 726 (2013), pp. 88–119.

[14] CMS Collaboration. Observation of a new boson with mass near 125 GeV in pp collisions at $\sqrt{s}$ = 7 and 8 TeV. *JHEP* 1306 (2013), p. 081.

[15] ATLAS Collaboration. Evidence for the spin-0 nature of the Higgs boson using ATLAS data. *Phys. Lett.* B 726 (2013), pp. 120–144.

[16] CMS Collaboration. Study of the mass and spin-parity of the Higgs boson candidate via its decays to Z boson pairs. *Phys. Rev. Lett.* 110 (2013), p. 081803.

[17] R. Aaij et al. Observation of the Resonant Character of the $Z(4430)^-$ State. *Phys. Rev. Lett.* 112 (22 2014), p. 222002.

[18] A. Collaboration. The ATLAS Experiment at the CERN Large Hadron Collider. *Journal of Instrumentation* 3.08 (2008), S08003.

[19] ATLAS Collaboration. Measurement of the inclusive isolated prompt photon cross section in pp collisions at $\sqrt{s}$ = 7 TeV with the ATLAS detector. *Phys. Rev. D* 83 (2011), p. 052005.

[20] *Photon Shower Shapes Data/MC Comparisons from $Z + \gamma$ events*. Tech. rep. ATL-COM-PHYS-2013-600. Geneva: CERN, May 2013.

[21] *Measurements of the photon identification efficiency with the ATLAS detector using 4.9 fb^{-1} of pp collision data collected in 2011*. Tech. rep. ATLAS-CONF-2012-123. Geneva: CERN, 2012.

[22] *Reconstruction of collinear final-state-radiation photons in Z decays to muons in $\sqrt{s}$=7 TeV proton-proton collisions.* Tech. rep. ATLAS-CONF-2012-143. Geneva: CERN, Nov. 2012.

[23] M. L. Mangano et al. ALPGEN, a generator for hard multiparton processes in hadronic collisions. *JHEP* 0307 (2003), p. 001.

[24] T. Sjöstrand, S. Mrenna, P. Skands. A brief introduction to PYTHIA 8.1. *Comput. Phys. Commun.* 178 (2008), pp. 852–867.

[25] E. Barberio, B. van Eijk, and Z. Was. Photos: a universal Monte Carlo for QED radiative corrections in decays. *Comput. Phys. Commun.* 66.1 (1991), pp. 115 –128.

[26] S. Agostinelli et al. GEANT4: A Simulation toolkit. *Nucl. Instrum. Meth.* A506 (2003), pp. 250–303.

[27] J. Beringer et al. Review of Particle Physics. *Phys. Rev. D* 86 (2012), p. 010001.

[28] ATLAS Collaboration. Search for Higgs boson decays to a photon and a Z boson in pp collisions at $\sqrt{s}$ = 7 and 8 TeV with the ATLAS detector. *Phys. Lett. B* 732 (May 2014), pp. 8–27.

[29] ATLAS Collaboration. Measurement of the Higgs boson mass from the $H \to \gamma\gamma$ and $H \to ZZ^* \to 4\ell$ channels with the ATLAS detector using 25 fb^{-1} of pp collision data. *Phys. Rev. D* 90 (2014), p. 052004.

[30] ATLAS Collaboration. Electron and photon energy calibration with the ATLAS detector using LHC Run 1 data. *Eur. Phys. J. C* 74.10, 3071 (2014).

REFERENCES

[31] S. H Abidi, C Anastopoulos, and M Antonelli. *Event Selection and background estimation for the measurement of the properties of the Higgs particle in the four lepton decay channel with the ATLAS detector*. Tech. rep. ATLAS INTERNAL NOTE. Geneva: CERN.

[32] ATLAS Collaboration. Measurement of the Higgs boson mass from the $H \to \gamma\gamma$ and $H \to ZZ^* \to 4\ell$ channels with the ATLAS detector using 25 fb^{-1} of pp collision data. *Phys. Rev. D* 90 (2014), p. 052004.

[33] J.-B. Blanchard, J.-B. de Vivie, and P Mastrandrea. *In situ scales and smearings from Z and J/Ψ events*. Tech. rep. ATL-COM-PHYS-2013-1653. Geneva: CERN, 2013.

[34] C Rangel-Smith, B Lopez Paredes, and Y Yamaguchi. *In-situ photon scales from radiative Z decays*. Tech. rep. ATL-COM-PHYS-2013-1634. Geneva: CERN, 2013.

[35] ATLAS Collaboration. Observation of a new particle in the search for the Standard Model Higgs boson with the ATLAS detector at the LHC. *Phys. Lett. B* 716 (2012), p. 1.

[36] CMS Collaboration. Observation of a new boson at a mass of 125 GeV with the CMS experiment at the LHC. *Phys. Lett. B* 716 (2012), p. 30.

[37] M. Carena, I. Low, and C. Wagner. Implications of a modified Higgs to diphoton decay width. *JHEP* 2012.8, 60 (2012).

[38] S Heinemeyer et al. *Handbook of LHC Higgs Cross Sections: 3. Higgs Properties: Report of the LHC Higgs Cross Section Working Group*. Tech. rep. arXiv:1307.1347. CERN-2013-004. Comments: 404 pages, 139 figures, to be submitted to CERN Report. Working Group web page: https://twiki.cern.ch/twiki/bin/view/LHCPhysics/CrossSections. Geneva, 2013.

[39] I. Low, J. Lykken, and G. Shaughnessy. Singlet scalars as Higgs imposters at the Large Hadron Collider. *Phys. Rev.* D 84 (2011), p. 035027.

[40] I. Low, J. Lykken, and G. Shaughnessy. Have we observed the Higgs (imposter)? *Phys. Rev.* D 86 (2012), p. 093012.

[41] A. Azatov et al. New Prospects for Higgs Compositeness in $h \to Z\gamma$. *Phys. Rev.* D 88 (2013), p. 075019.

[42] The CMS Collaboration. Evidence for the direct decay of the 125 GeV Higgs boson to fermions. *Nat. Phys.* 10 (Aug. 2014), pp. 557–560.

[43] S. Alioli, P. Nason, C. Oleari and E. Re. NLO Higgs boson production via gluon fusion matched with shower in POWHEG. *JHEP* 0904 (2009), p. 002.

[44] P. Nason and C. Oleari. NLO Higgs boson production via vector-boson fusion matched with shower in POWHEG. *JHEP* 1002 (2010), p. 037.

[45] E. Bagnaschi et al. Higgs production via gluon fusion in the POWHEG approach in the SM and in the MSSM. *JHEP* 1202 (2012), p. 088.

[46] T. Gleisberg et al. Event generation with SHERPA 1.1. *JHEP* 0902 (2009), p. 007.

[47] S. Hoeche, S. Schumann, and F. Siegert. Hard photon production and matrix-element parton-shower merging. *Phys. Rev. D* 81 (2010), p. 034026.

[48] G. Corcella et al. HERWIG 6: an event generator for hadron emission reactions with interfering gluons (including super-symmetric processes). *JHEP* 0101 (2001), p. 010.

[49] S. Frixione and B. R. Webber. Matching NLO QCD computations and parton shower simulations. *JHEP* 0206 (2002), p. 029.

[50] S. Frixione, P. Nason, and B. R. Webber. Matching NLO QCD and parton showers in heavy flavour production. *JHEP* 0308 (2003), p. 007.

[51] H.-L. Lai et al. New parton distributions for collider physics. *Phys. Rev. D* 82 (7 2010), p. 074024.

REFERENCES

[52] M. Grazzini and H. Sargsyan. Heavy-quark mass effects in Higgs boson production at the LHC. English. *JHEP* 2013.9, 129 (2013).

[53] J. Pumplin et al. New Generation of Parton Distributions with Uncertainties from Global QCD Analysis. *JHEP* 2002.07 (2002), p. 012.

[54] A. Djouadi, J. Kalinowski, and M. Spira. HDECAY: a program for Higgs boson decays in the Standard Model and its supersymmetric extension. *Comput. Phys. Commun.* 108.1 (1998), pp. 56 –74.

[55] A. Bredenstein et al. Precise predictions for the Higgs-boson decay $H \to WW/ZZ \to 4$ leptons. *Phys. Rev. D* 74 (1 2006), p. 013004.

[56] S. Actis et al. {NNLO} computational techniques: The cases and $H \to \gamma\gamma$ and $H \to gg$. *Nucl. Phys. B* 811.12 (2009), pp. 182 –273.

[57] J. Butterworth, J. Forshaw, and M. Seymour. Multiparton interactions in photoproduction at HERA. English. *Z. Phys. C Part. Fields* 72.4 (1996), pp. 637–646.

[58] *Improved electron reconstruction in ATLAS using the Gaussian Sum Filter-based model for bremsstrahlung*. Tech. rep. ATLAS-CONF-2012-047. Geneva: CERN, 2012.

[59] ATLAS Collaboration. Electron performance measurements with the ATLAS detector using the 2010 LHC proton-proton collision data. *Eur. Phys. J. C* 72.3, 1909 (2012).

[60] T Barklow et al. *Search for the Standard Model Higgs boson in the* $H \to Z\gamma$ *decay mode with 20.3* fb^{-1} *of* pp *collisions at* $\sqrt{s} = 8$ *TeV and 4.6* fb^{-1} *of* pp *collisions at* $\sqrt{s} = 7$ *TeV*. Tech. rep. ATL-COM-PHYS-2013-1397. Geneva: CERN, 2013.

[61] ATLAS Collaboration. Measurements of $W\gamma$ and $Z\gamma$ production in pp collisions at $\sqrt{s} = 7$ TeV with the ATLAS detector at the LHC. *Phys. Rev.* D 87 (2013), p. 112003.

[62] ATLAS Collaboration. Improved luminosity determination in pp collisions at $\sqrt{s} = 7$ TeV using the ATLAS detector at the LHC. *Eur. Phys. J. C* 73.8, 2518 (2013).

[63] *Muon reconstruction efficiency in reprocessed 2010 LHC proton-proton collision data recorded with the ATLAS detector*. Tech. rep. ATLAS-CONF-2011-063. Geneva: CERN, 2011.

[64] ATLAS Collaboration. Electron performance measurements with the ATLAS detector using the 2010 LHC proton-proton collision data. *Eur. Phys. J. C* 72.3, 1909 (2012).

[65] ATLAS and CMS Collaborations. *Procedure for the LHC Higgs boson search combination in summer 2011*. Tech. rep. ATL-PHYS-PUB-2011-011. Geneva: CERN, 2011.

[66] A. L. Read. Presentation of search results: The CL(s) technique. *J. Phys. G: Nucl. Part. Phys.* 28 (2002), p. 2693.

[67] G. Cowan et al. Asymptotic formulae for likelihood-based tests of new physics. *Eur. Phys. J. C* 71 (2011), p. 1554.

[68] D. Gastler et al. Measurement of scintillation efficiency for nuclear recoils in liquid argon. *Phys. Rev. C* 85.6 (June 2012), p. 065811.

[69] E. Aprile et al. *Noble Gas Detectors*. Wiley, 2006.

[70] H. Raether. *Electron avalanches and breakdown in gases*. Butterworths, 1964.

[71] M. S. Naidu and V. Kamarju. *High Voltage Engineering*. Second Edition. McGraw-Hill, 2009.

[72] W. Shockley. Currents to Conductors Induced by a Moving Point Charge. *J. Appl. Phys.* 9.10 (1938).

[73] S. Ramo. Currents Induced by Electron Motion. *Proceedings of the IRE* 27.9 (1939), pp. 584–585.

[74] G. F. Knoll. *Radiation detection and measurement*. Fourth Edition. New York: Wiley, 2010.

REFERENCES

[75] R. Bouclier et al. The Gas electron multiplier (GEM). *IEEE Trans. Nucl. Sci.* 44 (1997), pp. 646–650.

[76] J. Maia et al. Avalanche-ion back-flow reduction in gaseous electron multipliers based on GEM/MHSP. *Nucl. Instrum. Meth. A* 523.3 (2004), pp. 334 –344.

[77] T. Lopes et al. Position sensitive VUV gaseous photomultiplier based on Thick-multipliers with resistive line readout. *JINST* 8.09 (2013), P09002.

[78] H. Natal da Luz et al. MHSP with position detection capability. *Nucl. Instrum. Meth. A* 573 (Apr. 2007), pp. 191–194.

[79] A. Breskin et al. A concise review on THGEM detectors. *Nucl. Instrum. Meth. A* 598 (2009), pp. 107–111.

[80] M. Alexeev et al. The quest for a third generation of gaseous photon detectors for Cherenkov imaging counters. *Nucl. Instrum. Meth. A* 610.1 (2009). Proceedings of the Fifth International Conference on New Developments in Photodetection, pp. 174 –177.

[81] A. L. M. Silva et al. X-ray imaging detector based on a position sensitive THCOBRA with resistive line. *JINST* 8.05 (2013), p. 05016.

[82] M. Boulay. DEAP-3600 Dark Matter Search at SNOLAB. *J. Phys. Conf. Ser.* 375 (2012), p. 012027.

[83] M. Bossa. DarkSide-50, a background free experiment for dark matter searches. *JINST* 9 (2014), p. C01034.

[84] W. Lampl et al. Status of the ATLAS Liquid Argon Calorimeter and its Performance after Three Years of LHC Operation. *Astroparticle, Particle, Space Physics and Detectors for Physics Applications*. Chap. 94, pp. 593–597.

[85] G. Gratta and D. Sinclair. Present Status and Future Perspectives for the EXO-200 Experiment. *Adv. High Energy Phys.* (2013), p. 545431.

[86] J. Shirai. KamLAND-Zen: Status and Future. *Nucl. Phys. Proc. Suppl.* 237-238 (2013), pp. 28–30.

[87] M.-L. Gallin-Martel et al. Experimental results and first 22Na source image reconstruction by two prototype modules in coincidence of a liquid xenon positron emission tomograph for small animal imaging. *Nucl. Instrum. Meth. A* 682.0 (2012), pp. 66 –74.

[88] J. Bushberg. *The Essential Physics of Medical Imaging*. Lippincott Williams & Wilkins, 2002.

[89] G. Plante et al. New measurement of the scintillation efficiency of low-energy nuclear recoils in liquid xenon. *Phys. Rev. C* 84.4 (2011), p. 045805.

[90] T. Alexander et al. Light yield in DarkSide-10: A prototype two-phase argon TPC for dark matter searches. *Astropart. Phys.* 49.0 (2013), pp. 44 –51.

[91] D. S. Akerib et al. An ultra-low background PMT for liquid xenon detectors. *Nucl. Instrum. Meth. A* 703 (Mar. 2013), pp. 1–6.

[92] R. Acciarri et al. Demonstration and comparison of photomultiplier tubes at liquid Argon temperature. *JINST* 7 (Jan. 2012), p. 1016.

[93] Y. Xie et al. Quantum efficiency measurement of CsI photocathodes using synchrotron radiation at BSRF. *Nucl. Instrum. Meth. A* 664.1 (2012), pp. 310 –316.

[94] S. D. Torre. Status and perspectives of gaseous photon detectors. *Nucl. Instrum. Meth. A* 639.1 (2011), pp. 111–116.

[95] R. Chechik, A. Breskin, and et al. R Chechik. Advances in gaseous photomultipliers. *Nucl. Instrum. Meth. A* 595.1 (2008), pp. 116–127.

[96] L. Periale et al. A study of the operation of especially designed photosensitive gaseous detectors at cryogenic temperatures. *Nucl. Instrum. Meth. A* 567.1 (2006). Proceedings of the 4th International Conference on New Developments in Photodetection, pp. 381 –385.

[97] S. Duval et al. On the operation of a micropattern gaseous UV-photomultiplier in liquid-Xenon. *JINST* 6.04 (2011), P04007.

[98] Crystran Ltd. *Magnesium Fluoride (MgF2) Optical Material*. 2012. URL: http://www.crystran.co.uk/optical-materials/magnesium-fluoride-mgf2 (visited on 01–2015).

[99] H. Natal da Luz et al. MHSP with position detection capability. *Nucl. Instrum. Meth. A* 573 (Apr. 2007), pp. 191–194.

[100] R. Bellazzini et al. Imaging with the invisible light. *Nucl. Instrum. Meth. A* 581.1 (Feb. 2007). VCI 2007 Proceedings of the 11th International Vienna Conference on Instrumentation, pp. 246 –253.

[101] C. Shalem et al. Advances in Thick GEM-like gaseous electron multipliers Part I: atmospheric pressure operation. *Nucl. Instrum. Meth. A* 558 (2006), pp. 475–489.

[102] D. Mörmann. Study of novel gaseous photomultipliers for UV and visible light. JINST TH 004. PhD thesis. Weizmann Institute of Science, Israel, 2005.

[103] C. Richter et al. On the efficient electron transfer through GEM. *Nucl. Instrum. Meth. A* 478.3 (2002), pp. 538 –558.

[104] C. D. R. Azevedo et al. Towards THGEM UV-photon detectors for RICH: on single-photon detection efficiency in Ne/CH_4 and Ne/CF_4. *JINST* 5 (Jan. 2010), p. 1002.

[105] J. F. C. a. Veloso et al. THCOBRA: Ion back flow reduction in patterned THGEM cascades. *Nucl. Instrum. Meth. A* 639.1 (May 2011), pp. 134–136.

[106] M Cortesi et al. Investigations of a THGEM-based imaging detector. *JINST* 2.09 (2007), P09002.

[107] P. Martinengo, E. Nappi, and V. Peskov. Position Sensitive Gaseous Photomultipliers. *ArXiv e-prints: 1008.1327* (Aug. 2010).

[108] *Candle light movie*. http://www.hep.shef.ac.uk/people/lopez/candlemovie.html. Visited on 01-2015.